Adaptive dispersion compensation of a fiber for the Timing Electro Optical Sampling Experiment at TTF2

Diplomarbeit
von
Franciskus Van den Berghe

vorgelegt an der
Universität Hamburg

angefertigt am
Deutschen Elektronen-Synchrotron (DESY) Standort Hamburg

Hamburg, Juni 2005

Gutachter der Diplomarbeit:	Prof. Dr. J. Roßbach (Universität Hamburg) Dr. B. Schmidt (DESY)

Contents

Definitions

The following symbols will be used:

$a(t), a(\Omega)$	temporal, spectral amplitude of the electric field
g	grating constant
D	dispersion parameter in [D] = [ps/nm/km]
$\Delta\tau_p$	pulse duration
$\Delta\omega_p$	bandwidth
$\vec{E}$	electric field strength
$e(z,t)$	real scalar electric field strength
$\tilde{e}(z,t)$	complex scalar electric field strength
$\tilde{E}(z,\omega)$	complex scalar spectral field strength
ω, ω_l	angular frequency, central angular frequency
$\Omega = \omega - \omega_l$	relative angular frequency
$\varepsilon(t)$,$\mathfrak{e}(\Omega)$	complex envelope of the temporal, spectral field strength
$\mathfrak{F}\{\cdot\}, \mathfrak{F}^{-1}\{\cdot\}$	complex , inverse Fourier-transformation
$\varphi(t), \varphi\omega$	slowly varying temporal, spectral phase
$\phi(t), \phi(\Omega)$	temporal, spectral phase
$I(t)$	temporal intensity of the electric field
k	wave number
λ	wavelength
m	diffraction order of the grating
$m(k), M(k)$	modulator mask, its spatial Fourier transformation
S	detector signal
t	time
v_g	group velocity
v_{Ph}	phase velocity
$\Xi(\Omega), \xi(t)$	transfer function, response function

Table 1: *Mathematical symbols*

Abbreviations and acronyms used in this work:

FEL	Free Electron Laser
VUV-FEL	Vacuum Ultraviolet Free Electron Laser
TESLA	TeV Energy Superconducting Linear Accelerator
TTF	TESLA Test Facility
SHG	Second Harmonic Generation
TEO	Timing Electro Optical sampling
ITO	Indium Tin Oxide
BBO	Beta Barium Borate
SLM	Spatial Light Modulator
SPM	Self Phase Modulation
ZnTe	Zinc-Telluride
Ti:Sa	Titan:Sapphire
SASE	Self-Amplified-Spontaneous-Emission
FWHM	Full Width at Half Maximum
EOS	Electro Optical Sampling
GVD	Group Velocity Dispersion
MFD	Mode Field Diameter
LC	Liquid Crystal
OA	Optical Axis
OPA	Optical Parametric Amplifier
OTR	Optical Transition Radiation
PLD	Path Length Difference
TOD	Third Order Dispersion
PMT	Photomultiplier
GA	Genetic Algorithm

Table 2: *Abbreviations and acronyms*

Abstract

My work describes a 170 m long dispersion free and polarization maintaining laser beam transport system for a sub-100 fs electron bunch arrival-time monitor for the Vacuum Ultraviolet Free Electron Laser (VUV-FEL) at DESY. The arrival-time monitor is based upon the electro-optic effect in Zinc-Telluride which becomes birefringent in present of the electric field of the electron bunch. This process will be sampled by linear polarized Titan:Sapphire laser pulses with a pulse duration less than 80 fs full width at half maximum. If the laser pulses and the electric field simultaniously pass the crystal, the laser pulses become elliptically polarized. The elliptical polarization is converted to an intensity modulation which is read out by different cameras.
The laser beam transport system consists of a fiber, a grating compressor and a pulse shaping setup. The light propagation through each element has been analyzed and simulated to find the correct specification for a non dispersive and polarization maintaining light transport system.

Zusammenfassung

Im Rahmen meiner Arbeit wird ein 170 m langes dispersionsfreies und polarisationserhaltendes Laserstrahltransportsystem entwickelt. Der zu transportierende Laserstrahl wird für einen sub-100 fs Zeitmonitor verwendet, mit dem die Ankunftszeit der Elektronenpakete des VUV-FEL am DESY bestimmt werden soll. Der Monitor beruht auf dem elektro-optischen Effekt in einem Zink-Telluride Kristall. Dieser Kristall wird in Anwesenheit des elektrischen Feldes der Elektronenpakete doppelbrechend. Diese Doppelbrechung wird mit dem zu transportierendem Laserstrahl abgetastet. Der Laserstrahl stammt von einem Titan:Saphir Laser, der 80 fs Pulse erzeugt. Die Laserpulse werden elliptisch polarisiert, wenn die Pulse den Kristall gleichzeitig mit dem elektrischen Feld des Elektronenpaket passieren. Die elliptische Polarisation wird in eine Intensitätsmodulation konvertiert, die von verschiedenen Kameras ausgelesen wird.
Das Laserstrahltransportsystem besteht aus einer 170 m langen Glasfaser, einem Gitterkompressor und einem Impulsformer. In dieser Arbeit wird die Lichtausbreitung in diesen optischen Elementen untersucht und simuliert um die genauen Spezifikationen zu erhalten, die einen dispersionfreien und polarisationserhaltenden Transport ermöglichen.

1 Introduction

The research of chemical and internal atomic processes and structures is important in physics.
But with the common method of investigation, it is just possible to produce freeze-frame images of microscopic processes, because of the high exposure time of the given diagnostic tools. If one uses pulsed light for imaging, the long exposure time is a consequence of a too long pulse duration of the detecting light.
Another limitation is that the wavelength of the light used to investigate the processes and structures, has to be in the order of the structure.
Thus, it is necessary to find a light source which negotiates these limitations.
Atomic structures are in the size-range of several Angström (=0.1 nm), so the light has to have a wavelength below 0.1 nm. While X-rays have a wavelength in that range. Common sources don't have the high brilliance required to image structures on short time scales.
In the course of circular accelerators, a new X-ray source was found. The light of this new source is called synchrotron radiation, which was originally an unwanted by-product. This discovery was the launch pad for the next generation of X-ray sources. However, the radiation is not pulsed so the problem of the high exposure time remains.
In 1971 John M.J. Madey developed the concept of Free Electron Lasers (FEL) [1]. Six years later the first laser radiation using a particle accelerator was generated. The low gain FEL initially used mirrors to achieve high laser power. The wavelength was limited to UV light by the material properties of the mirrors. To overcome this limitation Self Amplified Spontaneous Emission (SASE) FELs can be used. Here the light is amplified in a single passage through the so called undulator.
The X-ray Free Electron Laser solves both problems mentioned above. It allows combining ultrashort laser pulses with the spatial resolution of X-rays. Thereby, ultrashort laser pulse means pulses with a duration in the range of several femtoseconds (10^{-15} s). The brilliance of the X-ray Free Electron Laser should be much higher than conventional X-ray sources, sufficient to image structures in a single shot.
The Vacuum Ultraviolet Free Electron Laser (VUV-FEL) at the Deutsche Elektronen Synchrotron (DESY) is a source for ultrashort VUV and soft X-rays pulses and serves as a facility for the X-FEL which will be in operation in 2012.
The VUV-FEL will be used to investigate fast processes like photochemical reaction on a crystal surface, as phase pump-probe investigations, multi-photon and strong field processes and magnetization dynamics.
A common way to analyze fast processes is to split ultrashort laser pulses into two beams. One beam triggers ("pumps") a fast process in a sample and the other beam "probes" the status of the sample after a certain delay time. These experiments are called "pump-probe experiments" [2].

To setup pump-probe experiments with the VUV-FEL an external optical laser system has been installed during this thesis. The fast processes will be triggered either by the optical laser or by the FEL and the remaining laser source probes. This method offers the most advanced user facility for combined soft X-ray and laser light. For pump-probe experiments, the delay time between pump and probe has to be certain, so it is absolutely necessary to have a very good synchronization between the FEL and the optical laser. Therefore, it is existential to know the arrival time of the electron bunch which generates the FEL pulse. Conventional diagnostic tools for the bunch time arrival measurements like a streak camera have a resolution of around 200 fs [37]. For pump-probe experiments it is necessary to monitor the electron bunch arrival-time better than 100 fs. Controllable systems which are able to operate in this region of sub-100 fs are ultrashort lasers. Today, commercially available lasers operate with a pulse duration of less than 15 fs [18].
The goal is to measure with the ultrashort laser pulses the electron bunch arrival. This can be done by the technique of Electro Optic Sampling (EOS) [3]. This technique uses a crystal which becomes birefringent when an external electric field is present. This crystal is installed close to the electron trajectory. The electron bunch is relativistic and its co-propagating electric field induce transient birefringence in the crystal. This effect is sampled by a polarized femtosecond laser passing simultaneously the crystal.
The arrival-time can be measured by detecting the polarization change of the laser. This experiment is therefore called, Timing Electro Optic (TEO). The Timing Electro Optical experiment will deliver information about the relative timing jitter between the timing sources of the VUV-FEL. One source of the timing jitter is a lack of synchronization between the femtosecond laser and the radio frequency (RF) of the linear accelerator. Other sources for the jitter are:

- magnetic field changes in the bunch compressors
- variation of the exiting time of the electron bunch from the RF photo-injector
- phase noise of the masteroscillator
- thermal drifts in cables and electronics of the VUV-FEL.

Thus, the Timing Electro-Optical experiment delivers information about the accuracy of the synchronization.
The experiment is separated into two parts (see figure 1). The crystal and tools to diagnose the laser are installed close to the electron-bunch in the FEL tunnel (see figure 18). The sampling requires an optical laser with ultra-short pulses, which is located in the FEL experimental hall (see figure 17). The fs laser pulses are produced by a Ti:Sa laser with a central wavelength of $\lambda_l = 800\,\text{nm}$.

The Electro-Optical (EO) technique requires a well defined polarization at the crystal.
Hence, the laser beam has to be transported from the experimental hall to the tunnel while preserving the polarization and with vanishing dispersion.
My Diploma thesis focuses on the laser transport. It includes fiber-optic and pulse shaping techniques to fulfil the requirements for the delivery of the Ti:Sa femtosecond pulses over a distance of 170 m.

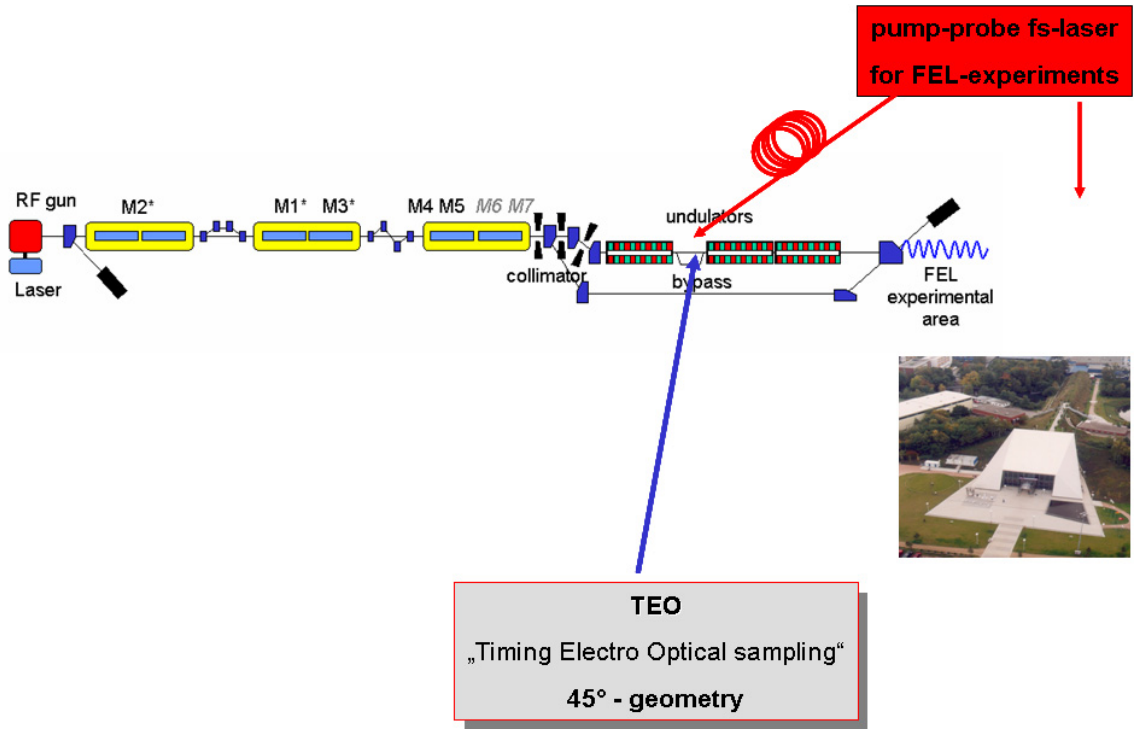

Figure 1: FEL setup with Timing Electro-Optical (TEO) sampling. The TEO experiment has two parts. One is located in the tunnel before the undulator, and the other is housed in the FEL hall. The acceleration module is marked with M1-M5.

1.1 Principle of the Free Electron Laser at DESY

The VUV-FEL at DESY is a Self Amplified Spontaneous Emission (SASE) Laser driven by a superconducting linear accelerator [14]. An overview of the accelerator is shown in figure 1.
The high brightness beam which is produced in an RF photo-injector. The FEL operation requires a high peak current of 2.5 kA which is achieved by two stages of longitudinal bunch compression, combining off-crest acceleration to produce an energy-chirp in the bunches with an energy-dependent path length in a magnetic chicane. In the first acceleration module the beam energy is increased to 140 MeV and the bunch is compressed from 20 ps to 2 ps Full Width at Half Maximum (FWHM). The second comopression takes place at an energy of 450 MeV from 2 ps to 0.4 ps (FWHM). Two more acceleration modules rise the energy to 850 MeV. A 30 m long undulator produces the FEL beam which will be transported over a distance of 50 m into the experimental-hall.
The acceleration modules which consist of superconducting cavities and mostly the bunch compressor generate a jitter in the arrival-time of the electron bunches at the undulator that why the TEO experiment is so important for the synchronization of the FEL and the pump-probe laser.

1.2 The Timing Electro Optical Sampling Experiment

The purpose of the Timing Electro Optical Sampling experiment is to provide a sub-100 fs arrival-time monitor for the VUV-FEL at DESY. The basis of the TEO experiment is the electro-optic effect, the induced birefringence in a crystal, when an external electro-magnetic field is present. In our case the electro-magnetic field is produced by a relativistic electron bunch. The induced birefringence is sampled by ultrashort laser pulses passing the crystal. If a laser pulse passes the crystal at the same time as the electron bunch, a change in the laser pulse polarization is generated.
For the TEO experiment we use a ZnTe crystal which is a member of an electro-optical anisotropic crystal class which becomes birefringence in presence of an electric field.
If the laser pulse passes the crystal not at the same time as the electron beam the polarization of the laser pulse will not be altered. If the laser pulse and the electron bunch crosses the crystal simultaneously the polarization of the linearly polarized laser pulse becomes elliptic. The temporal bunch profile is transformed into different phase retardations as a function of the polarization of the laser behind the crystal. A quarter wave-plate turns the now elliptically polarized laser pulse into a slightly perturbed circular polarization. This polarization is detected by using a polarizer which separates the two orthogonal components. The strength of the electric field can then be detected by an array of photo-diodes

or cameras as an amplitude modulation. Figure 1.2 shows how the electron beam passing the crystal influences the laser beam which is detected after the crystal.

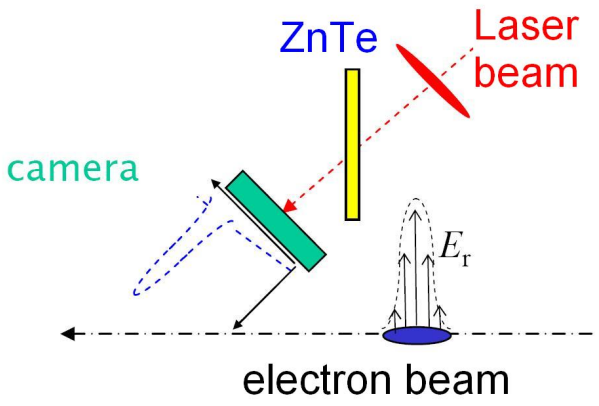

Figure 2: The electron beam influences the laser beam passing the ZnTe crystal. The electron bunch and the laser pulse propagate from the right to the left. The detector is either a photodiode or a CCD camera.

The aim of the electro-optic sampling is to get a temporal information by transforming temporal information into spatial information (see figure 1.2). But the transfer can only be achieved, if the laser pulse passes the crystal approximately at the same time as the electron bunch. The time frame for a possible measurement is about 5 ps given by the laser repetition rate and the laser pulse duration. Hency, the Ti:Sa laser pulses have to be synchronized with the electron beam within this accuracy.
To transfer the temporal information into spatial information the incident laser beam is tilted by 45° with respect to the crystal surface (figure 3). The polarization rotation as function of lateral position of the detected signal gives directly information about the timing. If the signal is in the center of the detector the timing can be considered as good. If the signal is shifted to one side the laer is either later or earlier with respect to the electron bunch. (see figure 3).

Additionally, simulations of the electro-optic transfer function of the ZnTe crystal show that it is useful to have a wedge-shaped crystal, which allows to variate the temporal resolution and improves the signal quality by shifting the laser spot horizontally on the crystal surface (see figure 5) [14]. A path through the thick part of the crystal means a strong signal amplitude but a poor temporal resolution whereas a path through a thin part of the crystal results in a high temporal resolution but a small signal amplitude (see figure 4), because a thick ZnTe crystal produces a strong electro-optical effect but enlarges the laser beam,

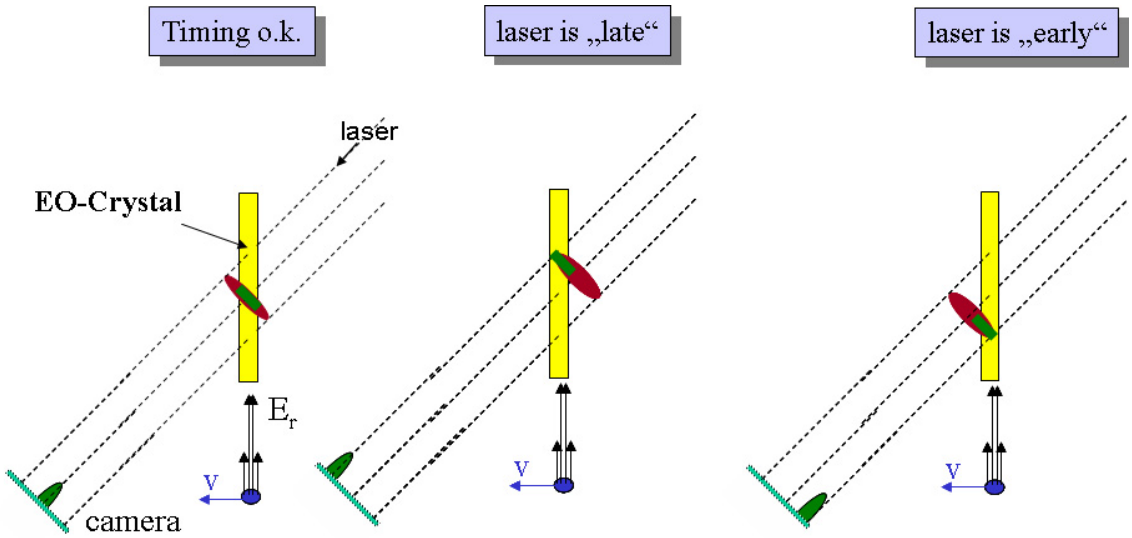

Figure 3: Principle of single-shot cross-correlation: The image of the laser signal on the camera gives direct information about the timing of the electron beam.

while a thin ZnTe crystal produces a small electro-optical effect but does not enlarges the laser beam as much as in the case of a thick crystal. The chosen crystal for the TEO experiment has the dimension and orientation depicted in figure 5. The crystal is mounted in such a way that it can be moved far away and near to the electron beam of the linac (see photography 6).

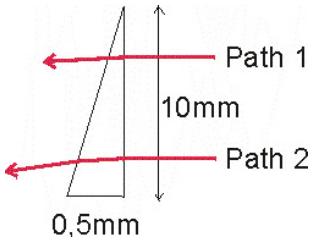

Figure 4: The picture shows two possible paths through the crystal: $Path1$ goes through a thin part of the crystal which gives a high temporal resolution but a small signal, while $Path2$ goes through a thick crystal which gives a strong signal but a poor temporal resolution.

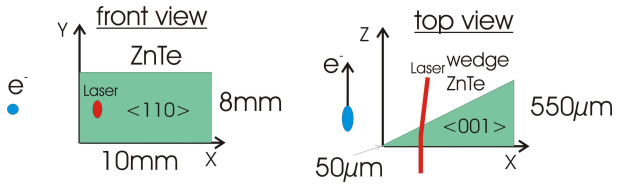

Figure 5: Dimensions and orientation of the ZnTe crystal. The wedge form allows for variation of the laser beam time resolution.

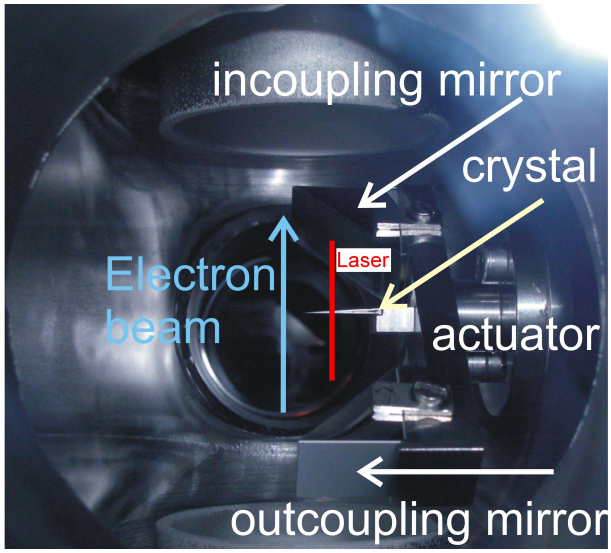

Figure 6: The wedge crystal is mounted on motorized sled. The figure is a top-view photo, the electron bunch passes the crystal from the bottom to the top.

2 Theoretical Background

2.1 Ultrashort Laser pulses

Ultrashort laser pulses allow time resolved measurements in the sub-100 fs range [7]. According to the Fourier theory, the bandwidth $\Delta\omega$ of the laser is inversely proportional to its pulse duration Δt, with $\Delta\omega \cdot \Delta t \geq 1/2$ [18].

For example to generate a pulse duration in the sub-ps range a bandwidth of more than 1 THz is needed.
Therefore, to realize short laser pulses a broad amplification bandwidth of the laser medium is needed. Furthermore, a mechanism is required which couples the phase relation of each frequency-mode generated in the laser oscillator, this is called mode coupling. The Ti:Sa-Laser ($Ti^{3+}Al_2O_3$) is a laser, which fulfils these conditions [24] [25]. The Ti:Sa was invented in 1990 [23] and shows amplification in the interval from 650 nm to 1100 nm, corresponding to a bandwidth of 200 THz. The bandwidth allows for pulse duration of only 5 fs [26]. Other advantages are the high thermal conductivity and a saturation fluence of about $1 J/cm^2$.
The mechanism to achieve mode coupling, which is equivalent to one short pulse propagating through the laser oscillator, can be realized by the Kerr effect in the Ti:Sa crystal [32].

The Kerr-effect is the induced birefringence, where the change of the index of refraction is proportional to the intensity of the laser field,

$$n = n_0 + n_2 I \quad . \tag{1}$$

The change of the index of refraction acts instantanously and does not depend on the accumulated energy density. Assuming a transverse Gaussian beam profile, the variation of the index of refraction can be written as [32]

$$n(r) = n_0 + \frac{1}{2} n_2 I(r) \quad , \tag{2}$$

with

$$I(r) = e^{-\frac{r^2}{2\sigma^2}} \quad . \tag{3}$$

If n_2 is positive, the index of refraction of a medium is larger at the axis of the beam than at larger radius r. The relevant parameter for the propagation of a laser beam is the optical path length $P(r)$ given by the product of the index of refraction n and the propagation distance d, $P(r) = n(r) \cdot d$. The result of the modulation of the index of refraction is a lensing effect which can be seen by replacing the constant thickness d by a variable one. The product with a constant index of refraction leads to the same optical path length (see figure 7):

$$P(r) = n(r)d = d(r)n_0 \tag{4}$$

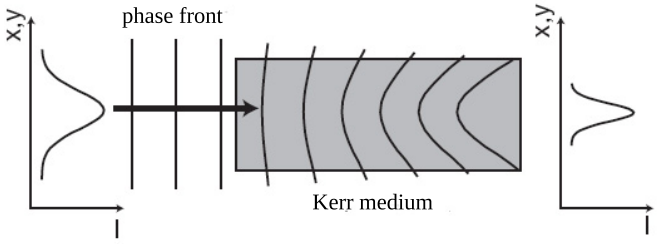

Figure 7: The Kerr effect focuses the laser beam

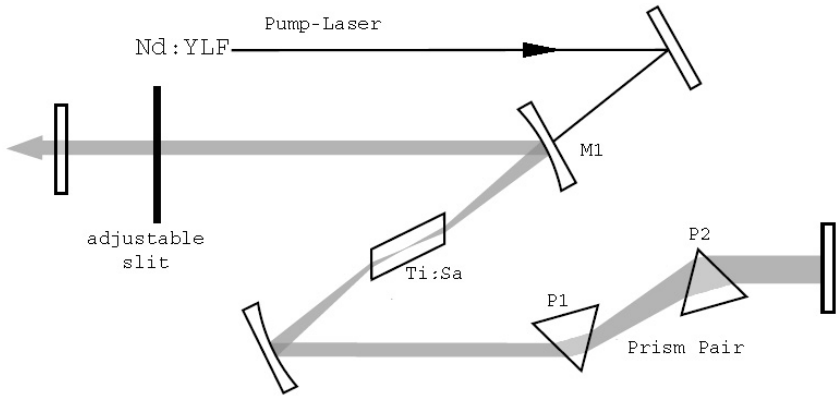

Figure 8: Scheme of a Ti:Sa short pulse laser

$$d(r) = \frac{d \cdot n(r)}{n_0} \tag{5}$$

Thus, one obtains a Gaussian lens, focusing the optical beam. This effect is enhanced while the laser beam propagates through a thick material, because focusing of the beam increases the focal power of the "created" lens. The linear diffraction on the medium will at some stage create an equilibrium state, balancing the Kerr effect. This is called self-focusing and allows the creation of ultrashort laser pulses (see figure 7).

Figure 8 shows the principal setup of a Ti:Sa laser system which is pumped by a Nd:YLF laser with a wavelength of 532 nm. The dichroic mirror M1 in figure 8 is transparent for the pumping wavelength, but reflects the emission wavelength of Ti:Sa. The two prisms P1 and P2 compensate the dispersion (see section 2.2) inside the cavity in a similar way as a grating compressor which will be described in section 2.7.

As shown, the index of refraction inside the Ti:Sa crystal is not constant for

all parts of a Gaussian wave and thus focused them. The self-focusing is large for strong intensity maxima negligible for the weak field of the continuous (cw) operation [32]. As the transverse structures of strong intensity maxima have been reduced in size by an adjustable slit, they are less subject to losses while propagating through the cavity.
The mode-locking is not established automatically, as long as no strong intensity fluctuations arise to create the relevant Kerr effect.The intensity fluctuation can be initiated by e.g. jolting quickly one of the mirrors which triggers the mode-locking process.
The reason why the pulses become short and are stabilized can be seen by taking the influence of the self-focusing on the time structure of the pulse into account. The change of the index of refraction is according to equation 2 is also responsible for a rapid change of phase of the wave as function of time, since the intensity $I(t)$ also varies rapidly with time. This self-modulation of the phase broadens the spectrum of the pulse and thus shortens its duration. Again an equilibrium is reached, when the dispersion compensates the self-modulation of the phase. In the end one pulse will travel back and forth in the cavity while keeping its structure. One mirror is semi-transparent ($\sim 90\%$ reflectivity), so that parts of the back and forth traveling pulse is out-coupled.

Formal Description of Ultra-Short Laser pulses

For theoretical treatment of laser beams one will first consider monochromatical light which are mainly described by their frequency ν. While propagating in z-direction in homogenous, isotropic, dielectric media there shell be a dispersion relation which will be the topic of section 2.2.
Monochromatical light is fully described by Maxwells-equations. In case of no absorption the time variation of the electric field strength $\vec{E}$ and the magnetic field strength $\vec{H}$ follows

$$\Delta\vec{E} - \frac{1}{v_{Ph}^2}\frac{\partial^2}{\partial t^2}\vec{E} = 0 \quad , \tag{6}$$

$$\Delta\vec{H} - \frac{1}{v_{Ph}^2}\frac{\partial^2}{\partial t^2}\vec{H} = 0 \quad , \tag{7}$$

with

$$v_{Ph} = \frac{1}{\sqrt{\epsilon\mu\epsilon_0\mu_0}} = \frac{c}{n} \quad . \tag{8}$$

where ϵ_0 is the dielectric constant of the vacuum, ϵ the relative dielectric constant, μ_0 the permeability of the vacuum, μ relative permeability, c the speed of light,

A the amplitude, ϕ_0 the initial phase of the wave and v_{Ph} the phase velocity. A solution of the wave equation for the electric field is:

$$e(z,t) = A\cos(2\pi\nu t - kz + \phi_0) = Re\{\tilde{e}(z,t) = Ae^{i(2\pi\nu t - kz + \phi_0)}\} \tag{9}$$

This function represents a linearly polarized plane wave with the frequency ν propagating in positive z-direction. To simplify further calculation, the complex description of the electric field will be used. Since the Maxwell equations are linear also a superposition of monochromatic waves solves the wave equation:

$$\tilde{e}(z,t) = \int_0^\infty A(\nu)e^{i[2\pi\nu t - kz + \phi_0(\nu)]}d\nu = \frac{1}{2\pi}\int_0^\infty A(\omega)e^{i[\omega t - kz + \phi_0(\omega)]}e^{i\omega t}d\omega \quad . \tag{10}$$

A light pulse can be represented by the superposition of monochromatic waves. The electric field can be represented either in frequency domain or in time domain:

$$\tilde{E}(\omega) = A(\omega)e^{i\phi(\omega)} = \mathfrak{F}\{\tilde{e}(t)\} = \int_{-\infty}^{\infty}\tilde{e}(t)e^{-i\omega t}dt \tag{11}$$

and

$$\tilde{e}(t) = a(t)e^{i\phi(t)} = \mathfrak{F}^{-1}\{\tilde{E}(\omega)\} = \frac{1}{2\pi}\int_{-\infty}^{\infty}\tilde{E}(\omega)e^{i\omega t}d\omega \tag{12}$$

Integrating equation 12 results in an un-physical region of the frequency domain, but the integration is symmetric to zero, therefore the electrical field is set to zero for all frequencies below zero and the integration is multiplied by two to complete the integration. A slowly changing envelope $\varepsilon(t)$ is introduced using the Slowly Varying Envelope Approximation (SVEA) [10] one introduces . The electric field is split into a fast oscillation and its envelope

$$\tilde{e}(t) = \varepsilon(t)e^{i\omega_l t} \tag{13}$$

The carrier frequency ω_l is calculated by:

$$\omega_l = \frac{\int \omega\tilde{E}(\omega)\tilde{E}^*(\omega)d\omega}{\int \tilde{E}(\omega)\tilde{E}^*(\omega)d\omega} \tag{14}$$

Pulse duration and bandwidth

The pulse duration Δt_p is defined by FWHM of the intensity profile I(t).
A more general definition which includes the entire pulse profile is:

$$\Delta t_p^2 = \frac{\int (t-t_s)^2\varepsilon(t)\varepsilon^*(t)dt}{\int \varepsilon(t)\varepsilon^*(t)dt} \quad , \tag{15}$$

where t_s is the temporal center of mass. The bandwidth of the pulse is given by:

$$\Delta\omega_p^2 = \frac{\int \Omega^2\mathfrak{e}(\Omega)\mathfrak{e}^*(\Omega)d\Omega}{\int \mathfrak{e}(\Omega)\mathfrak{e}^*(\Omega)dt} \quad , \tag{16}$$

where $\mathfrak{e}(\Omega)$ is the complex envelope of the spectral electric field strength and $\Omega = \omega - \omega_l$ is the relative angular frequency. The bandwidth and pulse duration is limited in its product:

$$\Delta t_p \cdot \Delta\omega_p \geq \frac{1}{2} \quad . \tag{17}$$

The relation can be derived by multiplying equations 15 and 16 and applying the Schwarz inequation [10],[32]. Therefore, a short pulse requires a broad spectral bandwidth.

Laser pulse models

The temporal profile of a ultrashort laser pulse exiting the Ti:Sa laser oscillator is well descripted by a Gaussian pulse:

$$\tilde{\varepsilon}(t) = \tilde{\varepsilon}_0 e^{-(t/\tau_G)^2} \quad . \tag{18}$$

$\tilde{\varepsilon}_0$ is the amplitude and the parameter τ_G is defined by the FWHM τ_H with

$$\tau_G = \frac{\tau_H}{\sqrt{2ln2}} \quad . \tag{19}$$

The Gaussian pulse appropriate time-bandwidth product is:

$$\Delta t_p \Delta\omega_p = 1/2 \quad . \tag{20}$$

It is called bandwidth limited or Fourier limited, if there is no phase modulation. If a Gaussian pulse is phase modulated, the time-bandwidth product will be exceeded. As a consequence the time-bandwidth product shows, if the pulse is phase modulated or not. If the pulse is modulated it is common to describe the spectral field by an amplitude- and a phase-function.

$$\tilde{\mathfrak{e}}(\Omega) = \mid \tilde{\mathfrak{e}}(\Omega) \mid e^{-i\phi(\Omega)} \tag{21}$$

2.2 Dispersion

The dependence of the index of refraction on the wavelength $n = n(\omega)$ is called dispersion. Dispersion can be described by the Fourier-transformation of the wave equation 9:

$$\frac{\partial^2}{\partial z^2}\tilde{E}(z,\omega) + \frac{\omega^2}{v_{Ph}^2}\tilde{E}(z,\omega) = 0 \quad . \tag{22}$$

The equation, which follows from applying the spectral solution $\tilde{E}(z,\omega) = A(\omega)e^{i[-kz+\phi_0(\omega)]}$ onto the wave equation, is the so called dispersion-relation:

$$k^2(\omega) = \frac{\omega^2}{v_{Ph}^2} = \frac{\omega^2}{c^2}n^2(\omega) \quad . \tag{23}$$

The spectral phase change in a homogeneous medium distance z is:

$$\phi(\omega) = k(\omega)z = \frac{\omega}{c}n(\omega)z \quad . \tag{24}$$

In the case of a linear propagation in a dispersive medium the change of the electric field is sum of the spectral phases:

$$\mathfrak{e}(z_0 + z, \Omega) = \mathfrak{e}(z_0, \Omega)e^{-ik(\omega_l+\Omega)z} \quad . \tag{25}$$

The temporal behaviour can be calculated by a Taylor expansion around the central frequency ω_l

$$k(\omega) = k(\omega_l + \Omega) = k(\omega_l) + \frac{\partial k}{\partial \omega}|_{\omega_l} \cdot \Omega + \frac{1}{2}\frac{\partial k^2}{\partial \omega^2}|_{\omega_l} \cdot \Omega^2 + ... \tag{26}$$

$$= k_l + k_l'\Omega + \frac{1}{2}k_l''\Omega^2 + ... \quad . \tag{27}$$

The derivatives of k are given by the frequency dependent index of refraction:

$$k_l = \frac{\omega_l}{c}n(\omega_l) = \frac{2\pi}{\lambda_l}n(\lambda_l) \tag{28}$$

$$k_l' = \frac{n(\omega_l)}{c} + \frac{\omega_l}{c}\frac{\partial n}{\partial \omega}|_{\omega_l} = \frac{n(\lambda_l)}{c} - \frac{\lambda_l}{c}\frac{\partial n}{\partial \lambda}|_{\lambda_l} \tag{29}$$

$$k_l'' = \frac{2}{c}\frac{\partial n}{\partial \omega}|_{\omega_l} + \frac{\omega_l}{c}\frac{\partial^2 n}{\partial \omega^2}|_{\omega_l} = \frac{\lambda_l^3}{2\pi c^2}\frac{\partial^2 n}{\partial \lambda^2}|_{\lambda_l} \quad . \tag{30}$$

The Taylor series are inserted into the Fourier-transformation of equation 22:

$$\varepsilon(z,t) = \frac{1}{2\pi}\int \mathfrak{e}(0,\Omega)e^{-i(k_l+k_l'\Omega+\frac{1}{2}k_l''\Omega^2+...)z}e^{i\Omega t}d\Omega \tag{31}$$

$$= e^{-k_l z}\frac{1}{2\pi}\int \mathfrak{e}(0,\Omega)e^{-i(\frac{1}{2}k_l''\Omega^2+...)z}e^{i\Omega(t-k_l' z)}d\Omega \quad . \tag{32}$$

In absense of high order dispersion ($k_l'' = 0$) the envelope of the pulse at position z equals to a modulated envelope at the position 0 at an earlier time $k_l' z$. This is descriptedby the group velocity v_g.

$$\frac{1}{v_g} = k_l' = \frac{1}{v_{Ph}} + \frac{\omega_l}{c}\frac{\partial n}{\partial \omega} \mid_{\omega_l} \quad . \tag{33}$$

In presence of high dispersion the envelope is modified by k_l'' and higher orders. The modulation of the envelope is a result of the wavelength dependence of the group velocity. This effect is called Group Velocity Dispersion (GVD)

$$\frac{\partial v_g}{\partial \lambda} = \frac{\omega^2 v_g^2}{2\pi c} k_l'' \quad . \tag{34}$$

"Chirp" generally means a temporal change of the instantaneous carrier frequency caused by GVD. The dominant parameter is k_l'', since the influence of the higher orders decrease rapidly. k_l'' is called the linear chirp parameter. Higher orders of k are analogous higher order chirp parameter. Depending on the sign of the phase-modulation there are two kinds of chirps:

- Up-chirp is given in case of normal dispersion ($\frac{\partial n}{\partial \lambda} < 0$) where ($k_l''$ is positive that means a positive frequency modulation ($\frac{\partial \omega}{\partial t} > 0$).
- Down-chirp is induced by abnormal dispersion ($\frac{\partial n}{\partial \lambda} > 0$) so that k_l'' is negative, this results in a negative frequency modulation ($\frac{\partial \omega}{\partial t} < 0$).

In analogy to equation 27, the change of the spectral phase propagating through a medium can also be written in a Taylor array:

$$\varphi(\Omega) = \sum_{n=0}^{\infty} \frac{k_l^n}{n!} \Omega^n z = \sum_{n=0}^{\infty} \frac{\varphi_n}{n!} \Omega^n \tag{35}$$

with

φ_0 : phase movement under the envelope
φ_1 : time delay, $\mathfrak{e}(\Omega) \cdot e^{-i\varphi_1 \Omega} \rightleftharpoons \varepsilon(t - \varphi_1)$
φ_2 : linear chirp
φ_3 : quadratic chirp, etc.

2.3 Self-Phase Modulation

In case of high intensities of ultrashort laser pulses nonlinear effects arise in addition to dispersion effects. The Self-Phase Modulation (SPM) is one important nonlinear effect (depending on the square power of the electric field). SPM is a result of the Kerr-effect, which means, that the index of refraction of a medium depends on the intensity of the passing light. The main consequence is a broadening of the spectral distribution. The following mathematic description can be used for non-dispersive materials or very short propagation-lengths, where the temporal development of the intensity does not change significantly. The dependence of the index of refraction of a medium on the intensity of the laser is given by

$$n(t) = n_0 + n_2 \cdot I(t) \quad . \tag{36}$$

It follows by equation 23:

$$k = \frac{\omega_l}{c} \cdot n(t) = \frac{\omega_l}{c} \cdot (n_0 + n_2 I(t)) = k_l \cdot \left(1 + \frac{n_2}{n_0} I(t)\right) \quad . \tag{37}$$

The wave-vector also describes the change of the phase in the time domain propagating in z-direction:

$$\varphi(t) = -k_l \cdot \left(1 + \frac{n_2}{n_0} I(t,z)\right) z \quad . \tag{38}$$

The change of the electric field in case of a *nonlinear* propagation is described by the sum of the temporal phase:

$$\varepsilon(z_0 + z, t) = \varepsilon(z_0, t) e^{-ik(t)z} \quad . \tag{39}$$

Thus, nonlinear interaction causes a change of the pulse spectrum [10]. This effect can be analyzed in the case of SPM using the instantaneous frequency $\Omega(t)$. The instantaneous frequency is the temporal derivative of the phase:

$$\Omega(t) = \frac{\partial \varphi(t)}{\partial t} = -k_l \frac{n_2}{n_0} \frac{\partial}{\partial t} I(t,z) z \quad . \tag{40}$$

Concerning the Fourier relation between time and frequency, new frequency components are created in the frequency spectrum when a periodic amplitude or phase modulation is applied to a periodic signal. In the case of a positive n_2 lower frequencies at the leading edge and higher frequencies are created at the trailing edge of the pulse envelope. The new frequencies are still inside the original pulse envelope. The SPM is not a dispersive effect by itself, but the pulse which propagates through a transparent medium will be chirped during propagation and therefore, the new frequencies will broaden the pulse even faster. Figure 9 shows the influence of self-phase modulation on a Gaussian pulse propagating through a short dispersive element.

If one increases the propagation length, the original pulse profile is lost (see figure 9). There are other nonlinear processes which can occur in long dispersive elements. The main effects are the SPM [42], the generation of solitons [18], higher order of dispersion [43], stimulated Raman diffusion, parametric four-wave-mixing [45] and self-steeping [44]. To avoid such effects, the laser intensity

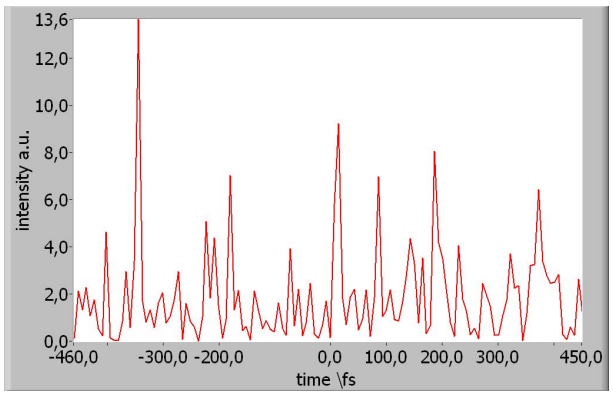

Figure 9: The Lab2 diagram shows the intensity as a function of time of a laser pulse which has propagated through 170 m of SQ1 glass.

has to be small by either increasing the radius of the beam or lengthening the pulse duration.

2.4 Simulation of ultrashort laser pulses with "Lab2 - The virtual femtosecond laboratory"

The mathematical description of short laser pulses is highly complex, as shown in the previous sections. Most of the phenomena acting in the temporal domain (dispersion) and the frequency domain (SPM) can not be solved analytically. Thus, they have to be treated numerically in a simulation.

The program package Lab2 was written in the year 1998 by B. Schmidt, M. Hacker, G. Stobrawa and T. Feurer at the Institute for Optics and Quantum Electronics (IOQ) in Jena [16]. The program allows the simulation of propagation of fs pulses in various media, as well as setups consisting of complicated optical elements like prisms and gratings.
Lab2 runs in the LabView environment which is a programming language by National Instruments. Lab2 allows the simulation of femtosecond labs, in a very convenient manner.
The Lab2 package includes laser sources, for example Gaussian and sech-square pulses, whose properties can easily be changed and adapted to the given boundary conditions. Furthermore, it includes optical elements as well as detectors. The elements are for example linear or nonlinear dispersive elements, grating compressors and pulse shapers. The detectors range from intensity and power detectors to Second Harmonic auto-correlation or Frequency Resolved Optical Gating. Lab2 solves the time dependent Schrödinger equation which describes the propagation of laser pulses in various media and uses the mathematics described in the previous sections. The results of the simulation generated by Lab2 has been used to understand many factores and technical challenges during the design and for understanding of the TEO experiment.
However, Lab2 only works in the frequency-time domain.

2.5 Fiber Optics

General Design of the fiber-optic

A schematic drawing of a fiber is shown in figure 10.

A fiber consists of four main components, the core with the highest index of refraction, the cladding, which is a material that surrounds the core of an optical fiber, its lower index of refraction, compared to that of the core, causes the transmitted light to propagate within the core, the coating and the buffer. The last two components are normally protecting plastic films. This type of fiber is called step-index-fiber, there are also gradient-fibres, which consist of multiple layers with increasing index of refraction.

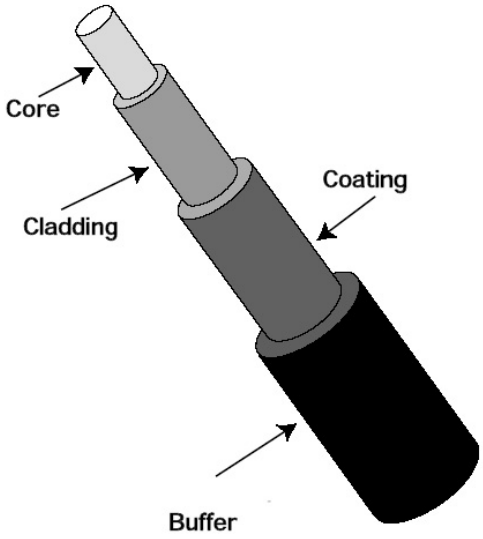

Figure 10: Cross-section of a standard fiber

Principles of reflection in fiber optics

The guiding of light through optical fibers is based on total reflection. One condition for total reflection is a transition from a material with higher to lower index of refraction. The other condition follows from the Snell law of refraction:

$$\sin(\alpha) = \frac{n_2}{n_1} \sin(\beta) \quad . \tag{41}$$

In the special case of a fiber, n_1 is the refraction index of the optically more dens medium 1, the core, and n_2 the refraction index of the optically thinner medium 2, the cladding, ($n_1 > n_2$). α is the angle of incidence and β the exiting angle of the light (see figure 11). The maximum value for $\sin(\beta)$ is 1, thus follows:

$$\sin(\alpha) > n_2/n_1 \tag{42}$$

If this equation is not fulfilled, the wave can not enter medium 2.
We define the critical angle α_g of total reflection by:

$$\sin(\alpha_g) = n_2/n_1 \quad . \tag{43}$$

But in reality there is still an intrusion of the wave in the medium 2. The intensity of the wave in medium 2 decreases as

$$I = I_0 \cdot e^{-z/\lambda} \quad . \tag{44}$$

If the cladding does not absorb and the cladding is much thicker than the wavelength, no energy is transferred into the cladding and losses are low.

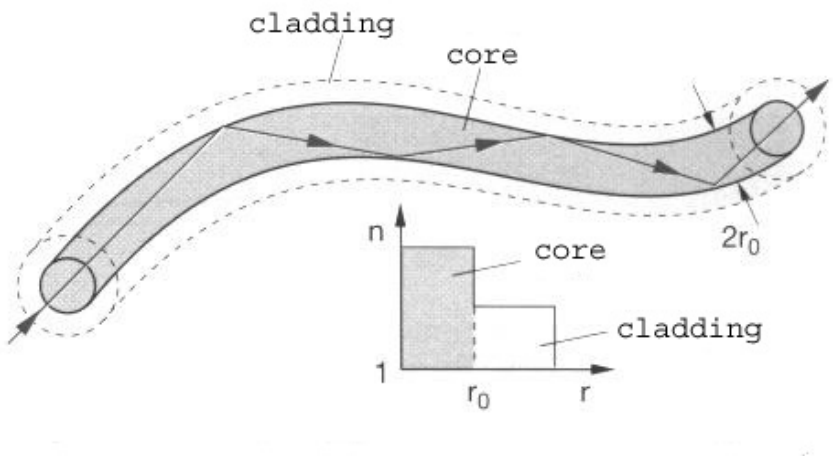

Figure 11: This Diagram shows the propagation of light in a fiber by total internal reflection. [4].

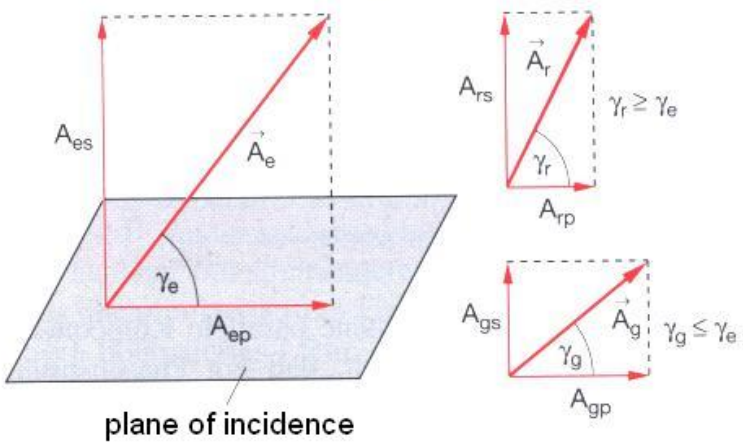

Figure 12: Changes in polarization due to internal reflection. Where $\vec{A}_e$ is the field vector of the incident beam.

In the case of linearly polarized light incidented at an angle α with respect to the surface, the polarization is altered.
This behaviour of polarized light propagating in a fiber can be better understood regarding figure 12 which shows the field vector of the electric field relative to the plane of incidence. The angle between the electric field vector and the plane of incidence is called γ_e. Therefore the angle γ_e can be expressed as:

$$\tan(\gamma_e) = \frac{A_{es}}{A_{ep}} \quad , \tag{45}$$

where the field vectors A_{es} and A_{ep} follow from figure 12.
The Fresnel formulas deliver the angle γ_r between the reflected electric field vector and the plane of incidence:

$$\tan(\gamma_r) = \frac{A_{rs}}{A_{rp}} = -\frac{cos(\alpha - \beta)}{cos(\alpha + \beta)} \cdot tan(\gamma_e) \quad . \tag{46}$$

The result of this is:

$$\gamma_r > \gamma_e, \tag{47}$$

because $\cos(\alpha - \beta) > \cos(\alpha + \beta)$. As a consequence, the polarization is tilted away from the plane of incidence for reflection.

2.6 Fiber Principles

Mode

Two types of fibers are distinguished by their mode behaviour:

- multimode fiber
- single mode fiber

For the TEO experiment a single-mode fiber is used. A single mode fiber is a fiber in which only one mode of the laser beam propagates. Common single mode fibers have a diameter less than 9 µm [18]. To realize single-mode fibers the core radius r has to fulfil the following equation [18]:

$$r < \frac{\lambda}{\pi\sqrt{n_1 - n_2^2}} \quad , \tag{48}$$

where n_1 is the index of refraction of the core medium and n_2 the index of refraction of the cladding medium.

Polarization Maintenance

Another important prerequisite for the fiber, which is used in the TEO experiment, is the polarization maintenance. Polarization maintaining single mode fibers split the polarization of the incident beam into two orthogonal components, propagating along the fast and the slow axis with different velocities of propagation.

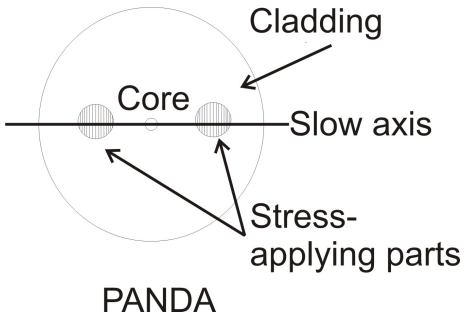

Figure 13: The stress structure of a polarization maintaining fiber

The decoupling of the two axis results from birefringence, which is induced by stress structures inside the fiber-optic cladding (see figure 13). This stress structure looks like a Panda bear, therefore such fibers are called PANDA-fiber. The slow axis is parallel to the stress field. A linear polarized laser beam has to be injected in that way that the polarization of the laser beam is parallel to the slow axis. So that the electric field vector of the incident beam has a preferred direction, which means that just the linear polarization propagates through the fiber. Small changes of the alignment of the slow axis with respect to the field vector of the linear polarized light cause large fluctuations in the polarization of the emitted light after propagating through the fiber.

Fiber Parameters

A single mode polarization maintaining fiber is characterized by the numerical aperture (NA), the fiber attenuation, the mode field diameter (MFD), the cut-off wavelength λ_{ct}, the D parameter and the h parameters. The last two parameter and the fiber attenuation are important for the fiber which is used in the TEO experiment.

Fiber Attenuation

Power loss in a fiber is caused by leakage, absorption and scattering from the core into the cladding.

The relative power loss of a fiber with the length dL is given by:

$$\frac{dP}{P} = -k \cdot dL \quad . \tag{49}$$

After integration:

$$P(L) = P(0) \cdot e^{-kL} \tag{50}$$

depicts an exponential decay of the transmitted power.
The attenuation constant k is given by

$$k = -\frac{1}{L} ln \frac{P(L)}{P(0)} \tag{51}$$

and depends on the wavelength and the fiber material. It is often given by the attenuation coefficient θ, which is given by

$$\theta = -\frac{10}{L} log \frac{P(L)}{P(0)} \tag{52}$$

with $[\theta] = \text{dB/km}$.

D Parameter

The D parameter describes the dispersion of a fiber.

$$D = -\frac{2\pi c}{\lambda_l^2} \cdot k_l'' = \frac{\Delta\tau}{L\Delta\lambda} \tag{53}$$

D is proportional to the GVD parameter k_l''. $\Delta\tau$ is the pulse duration after the dispersive medium of length L and $\Delta\lambda$ is the spectral width of the laser pulse. The D parameter is mostly given in the dimension $[D] = ps/nm/km$.

h Parameter

The h parameter is the polarization preserving parameter, it is given in the dimension 1/m. This parameter gives information about the relative deviation of the polarization along the fiber. The h parameter is important for choosing the fiber, because the h parameter times the fiber length L gives the percentage deviation of ideal polarization maintenance.

Wave propagation in a fiber

Dispersion is the dependence of the index of refraction on the wavelength $n(\lambda)$. There are three different types of dispersion, the mode-dispersion, the chromatic dispersion and the wave guide dispersion.

Mode Dispersion

Mode dispersion is generated according to section 2.2, because the light beam propagates the fiber with different trajectories and therefore with different propagation times. The pulse length increases. The phase velocity is given according to equation 8 by:

$$v_{Ph} = \frac{c}{\sqrt{1 - \frac{m^2\pi^2c^2}{d_f^2\omega^2}}} \tag{54}$$

Where m is the mode number and d_f is the fiber diameter. The mode dispersion is the limiting factor for the maximum distance of data transmission in multi-mode fiber-optics. Single mode fibers are not influenced by this kind of dispersion.

Chromatic Dispersion

Chromatic dispersion takes place in single- and multi-mode fibers, since it is a property of the fiber material itself. The index of refraction decreases in the region of normal dispersion proportional to the wavelength (see section 2.2). As a result the pulse spreads while propagating through the fiber.

Wave Guide dispersion

Wave guide dispersion is based on the wavelength dependence of the mode energy distribution in the core and in the cladding. A part of the central wavelength energy propagates into the cladding. This part increases with increasing wavelength. The energy in the cladding propagates faster than the energy in the core, because of the smaller index of refraction of the cladding.
The group delay of a wave with a shorter wavelength is larger than for waves with a longer wavelength.
This effect works against the chromatic dispersion, therefore the sum of the dispersion decreases for single-mode fibers. For single mode fiber the wave guide dispersion depends on the core-diameter, core-cladding index difference and the incident wavelength. A certain combination of these parameters allows a zero-dispersion fiber in which the wave guide dispersion has compensated the chromatic dispersion [41]. The important parameter is the wave guide parameter D_{wg} which depends on the index of refraction of the core n_1 and the cladding n_2, the material constants a and b and the wavelength λ is given by:

$$D_{wg} = -\left(\frac{n_1 - n_2}{\lambda c}\right) V \frac{d^2(Vb)}{dV^2} \tag{55}$$

with

$$V = \frac{2\pi a n_2}{\lambda}\sqrt{2(n_1 - n_2} \quad . \tag{56}$$

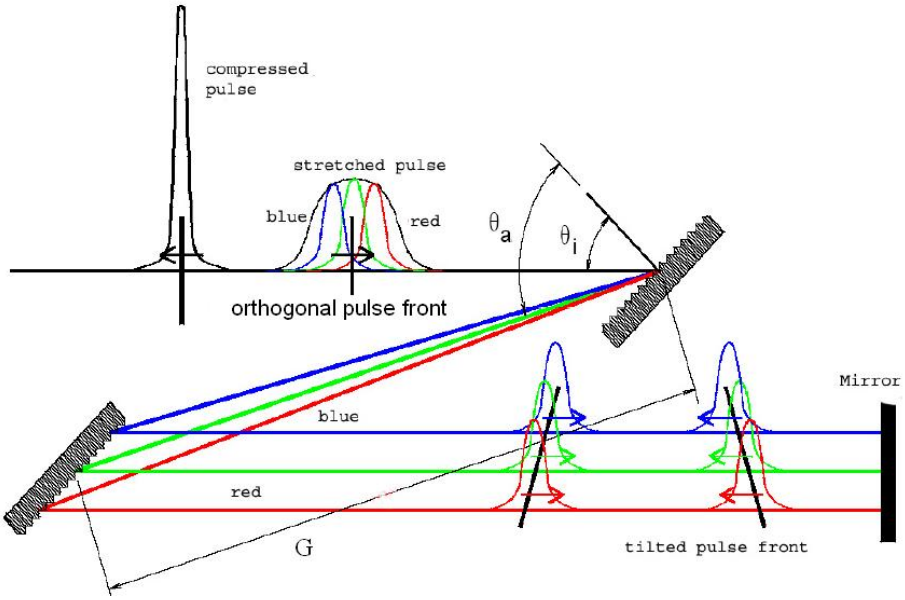

Figure 14: Setup of a grating compressor and the pulse propagation through the compressor. The red light leads the pulse train, so its path length is longer than the path length of the blue light [11].

2.7 Grating Compressor

Dispersion is not only produced by matter but also by gratings and prisms. The advantage in respect to "transparent media" is the fact that the dispersion in such a setup can be changed by adjusting the distance of the dispersive elements. Moreover it is also possible to choose the sign of the dispersion. Abnormal dispersion occurs in transparent media only in certain wavelength ranges or in specially designed media (photonic crystal fibers [10]). The use of dispersive optical elements like prisms and gratings is a special arrangement, which generates dispersion.
A general setup of a grating compressor is shown in figure 14. Up-chirp laser pulses can be temporally compressed with this setup of two parallel gratings.
The pulse front before the reflection at the first grating of the pulse is plane, so that every spectral part propagates in the same direction. The propagation direction of the light becomes wavelength dependent after the first grating reflection. The second grating disperses the different wavelength in a way that the propagation directions are parallel again. But now the spectral components are spatially displaced with respect to each other and the pulse front is tilted with respect to the beam direction. The laser pulses are reflected back through the grating setup by a mirror in order to avoid that different colors propagate colinear into the same direction. The shift of the beam depends on the wavelength and the

pulse duration is therefore reduced; the pulse front is orthogonal with respect to the propagation direction. The dispersion depends on the grating constant g, on the angle of incidence θ_i, on the wavelength λ, the grating distance d and on the order of diffraction m.
The following calculation includes the propagation twice through the setup, where θ_a is the angle of diffraction, with $\sin(\theta_i) + \sin(\theta_a) = \frac{\lambda}{g}$ follows:

$$\varphi_2 = \frac{d^2\varphi}{d\omega^2} = -\frac{m^2\lambda^3 d}{\pi c^2 g^2 \cos^3(\theta_a)} \tag{57}$$

and

$$\varphi_3 = \frac{d^3\varphi}{d\omega^3} = -\frac{3\lambda}{2\pi c}\frac{d^2\varphi}{d\omega^2}\left(1 + \frac{\lambda \sin(\theta_a)}{g\cos^2(\theta_a)}\right) \quad . \tag{58}$$

For a Gaussian pulse the duration τ_{out} can be calculated using the Fourier limited pulse duration $\tau_{in} = (2\pi)/(\Delta\omega)$, where $\Delta\omega$ is the bandwidth, by [9]:

$$\tau_{out} = \tau_{in}\sqrt{1 + 7,69\left(\frac{k''z}{\tau_{in}^2}\right)^2} \tag{59}$$

With $k''z = \varphi_2$ and $(\varphi_2)/(\tau_{in}^2) \gg 1$ follows:

$$\tau_{out} = \frac{2,77\varphi_2}{\tau_{in}} \tag{60}$$

2.8 Modulation of Laser Pulses

To be able to modulate a spectral phase and an amplitude of a ultrashort laser pulse it is necessary to have a filter mask at the Fourier plane. This can be realized for example by a grating stretcher. If a grating stretcher is used to generate a Fourier plane, the incident laser beam $e^+_{in}(t) = a(t) \cdot e^{i\psi(t)}$ ($a(t)$ is the amplitude and $\psi(t)$ is the phase) is transformed in the spectral field at the first grating $\tilde{E}^+_{in}(\omega)$ and is focused by a collecting mirror. This is mathematically speaking a complex Fourier-transformation:

$$\tilde{E}^+_{in}(\omega) = \mathfrak{F}\{E_{in}(t)\} \quad . \tag{61}$$

If the filter mask is placed in the Fourier plane, it influences the laser field $\tilde{E}^+_{in}(\omega) = A(\omega) \cdot e^{-i\Psi(\omega)}$ in its phase $\Psi(\omega)$ and amplitude $A(\omega)$ and the modulated laser-field becomes:

$$\tilde{E}^+_{out}(\omega) = \tilde{E}^+_{in}(\omega) \cdot R(\omega) e^{-i\upsilon(\omega)} \quad . \tag{62}$$

$R(\omega)$ describes the spectral amplitude modulation and $\upsilon(\omega)$ the spectral phase-modulation. When the laser beam has passed the filter mask, the spectral modulated field is transformed into a temporal modulated laser-field $e^+_{out}(t) = \mathfrak{F}^{-1}\{E^+_{out}(\omega)\}$ by an inverse Fourier-transformation . $e^+_{out}(t)$ is the modulated laser-pulse and $R(\omega)e^{-i\upsilon(\omega)}$ is called "spectral filter-mask". It can be a simple phase-mask ($R(\omega) = 1$), a simple amplitude-mask ($\upsilon(\omega) = 0$) or a combination of phase- and amplitude-mask. In this work, the SLM will be used as a phase-modulator to compensate the dispersion.

Modulation of a Laser Pulse by a Linear Phase Function

The pulse shift, which is caused by a linear phase function, can be analyzed regarding equation 62. The modulation-function of a linear phase-ramp is given by $\Xi(\Omega) = e^{-i\tau\Omega}$. A linear phase-modulation generates the field $\tilde{E}_{out}(\Omega) = \tilde{E}_{in}(\Omega) \cdot \Xi(\Omega)$ with $\tilde{e}_{out}(t) = \tilde{e}_{in}(t) \star \delta(t-\tau) = \tilde{e}_{in}(t-\tau)$ being a temporal shift of the pulse by $\Delta t = -\tau$. This results from the laws of the Fourier-transformation [35]. The linear phase modulation can now be combined with equation 111 to calculate the filter-function Ξ_{pix}.

$$\begin{aligned} \Xi_{pix}(\Omega) &= e^{-i\tau\Omega} \cdot \sum_{l=-N/2}^{N/2} \delta(\Omega - l \cdot \Delta x/a) \otimes rect\left(\frac{a\Omega}{(l-r)\Delta x}\right) \\ &+ m_{gap} \cdot \sum_{l=-N/2}^{N/2} \delta\left(\Omega - \left(l + \frac{1}{2}\right) \cdot \Delta x/a\right) \otimes rect\left(\frac{a\Omega}{r\Delta x}\right) \end{aligned} \tag{63}$$

The discrete filter function shows that for

$$\tau = z \cdot \frac{2\pi}{\Delta\Omega} \qquad with \quad z \in \mathbb{Z} \tag{64}$$

the filter-function causes no phase-modulation and the initial pulse has the same form as the exiting pulse.

Sinusoidal Phase Modulation

An initial pulse, which is sinusoidally phase modulated, can be described by the spectral field envelope:

$$\tilde{\mathfrak{e}}_1(\Omega_1) \propto e^{-\left(\frac{\Omega_1}{\Delta\Omega_1}\right)^2} e^{i\phi cos(\Delta\Omega_1+\psi)} \tag{65}$$

where ϕ is a modulation-amplitude and ψ an arbitrary constant phase. The modulation frequency is given by Δt, because in the time-domain a sinusoidal modulation is a pulse train, whose pulses are separated by a temporal distance of Δt. The phase modulation can be expressed by using the Bessel-function [8] [35]. With $cos(\Phi) = sin\left(\frac{\pi}{2} - \Phi\right)$, Bessel functions of first category and m^{th} order, the phase modulation is transformed into:

$$e^{i\phi cos(\Phi)} = \sum_{m=-\infty}^{\infty} J_m(\phi) e^{im\left(\frac{\pi}{2}-\Phi\right)} \tag{66}$$

The temporal field envelope of the pulse train can be calculated by Fourier-transformating of equation 71.

$$\tilde{\varepsilon}_1(t) \propto \sum_{m=-\infty}^{\infty} J_m(\phi) e^{im\left(\frac{\pi}{2}-\psi\right)-\frac{1}{4}(m\Delta t+t)^2\Delta\Omega_1^2}. \tag{67}$$

In the following the second harmonic will be regared.

Frequency Doubling of Phase Modulated Laser Pulses

The Second Harmonic Generation (SHG) generates a frequency doubling which is mathematically the square of the field envelope of the incident pulse in time domain:

$$\tilde{\varepsilon}_2(t) \propto \tilde{\varepsilon}_1^2(t) \quad . \tag{68}$$

This is similar to a convolution in frequency domain:

$$\tilde{\mathfrak{e}}_2(\Omega_2) \propto \int_{-\infty}^{\infty} \tilde{\mathfrak{e}}_1^2(\Omega_1)\tilde{\mathfrak{e}}_1^2(\Omega_2 - \Omega_1)d\Omega_1 \quad . \tag{69}$$

The convolution can be calculated with equation 71 and equation 66. The result is [8]:

$$\tilde{\mathfrak{e}}_2(\Omega_2) \propto e^{-\frac{1}{2}\left(\frac{\Omega_2}{\Delta\Omega_1}\right)^2} \sum_{m=-\infty}^{\infty} \alpha_m \tag{70}$$

with

$$\alpha_m = J_m\left(2\phi cos\left(\frac{\Delta t\Omega_2}{2}+\psi\right)\right)e^{(\frac{1}{2}im\pi-\frac{1}{8}(m\Delta t\Delta\Omega_1)^2)} \tag{71}$$

The term $-\frac{1}{8}(m\Delta t\Delta\Omega_1)^2$ causes an exponential decay of the terms α_m with increasing order m. Therefore, terms with lower order Bessel-function are dominant. Further calculation can be done by involving the specification of the Ti:Sa laser which is used for my work (see section 4.7).

3 Experimental Setup

3.1 Timing Electro Optical Sampling Experiment Setup

The Timing Electro Optical Sampling (TEO) experiment is a sub-100 fs electron-bunch arrival-time monitor for the VUV-FEL. The TEO experiment uses the electro-optical effect of a ZnTe crystal, which becomes birefringent if a electric field is present, in our case the electron-bunch. This effect is sampled by an ultrashort (a pulse duration of less than 100 fs) laser pulse.
The TEO experiment has been set up during my diploma thesis (see figure 16). This setup is divided into two parts; one is located in a Laser hutch in the FEL experimental hall (see figures 17 and 19) the other in the tunnel (see figures 18 and 20), the two setups are connected with a 170 m long fiber-optic cable (see figure 1). The laser is a Ti:Sa pulse train oscillator (KMLab MTS mini Ti:Sa) which is part of a pump-probe laser (see chapter 1). The pump-probe laser consists of an optical parametric amplifier (OPA) pumped by a Nd:YLF laser in burst pulse mode (1 MHz for 800 µs) synchronised with the electron bunch repetition frequency of 1 MHz (see figure 15). The pump-probe laser delivers either the "trigger" or the "sampler" for the pump-probe experiments (see section 1) located in the FEL-hall.

The Ti:Sa has a repetition rate of 108 MHz at a central wavelength of 800 nm. The pulses have a bandwidth of 30 nm, thus the Fourier limit results in a pulse duration of 36 fs.
Before the amplification the pulses are gated with a Pockels cell triggered with 1 MHz to be synchronised with the electron bunch frequency to filter out the non-amplified pulses which could produce background in pump-probe experiments. The non-amplified pulses are used for the electro-optic sampling.

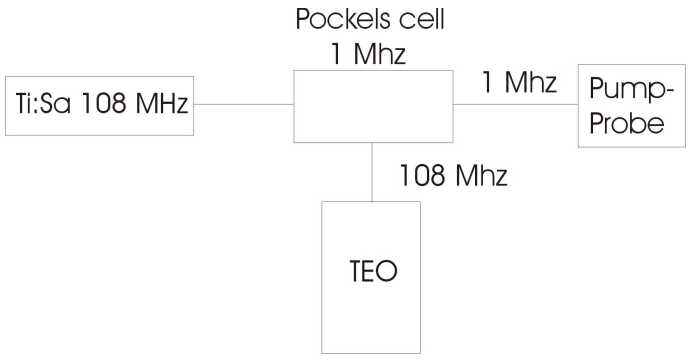

Figure 15: Laser pulse repetition rates for the different components

The EO technique requires ultra-short laser pulse with a well defined polarization and a pulse duration in the order of 50 fs FWHM (see section 1.2). As seen in figure 3 the pulse duration limits the resolution of the timing. Therefore, the optical transport from the laser hutch to the linac tunnel has to be non-dispersive. Dispersion if present would cause pulse broadening which would deliver no precise signal for timing (see section 1.2).
The laser transport has to be adapted to the constructional circumstances of the linac tunnel. The best way to transport light over a long distance is the use of a fiber. A fiber with a defined polarization is the polarization conserving single-mode fiber with a core material consisting of doped fused quartz (SQ1). This fiber has a dispersion which increases the pulse duration to 540 ps. In the dispersed pulse the long wavelength (so called "red light") are at the front and the short wavelengths (so called "blue light") at the tail.
This effect is compensated by a grating compressor (see figure 16) in a way that the compressor stretches the laser pulse up to a factor of 13 (450 ps) before the pulse enters the fiber but with an inverted arrangement of the wavelength. The pulse will be compressed in the fiber, because of the dispersion induced by the fiber core material. The dispersion is based on the wavelength dependent index of refraction, so that the precursory wavelengths of the incident laser pulse are more retarded than the following wavelengths of the laser pulse. Thus, at the end of the 170 m long fiber the laser pulse is compressed. The intensity of the laser pulses in the fiber depends on the pulse duration and the cross section of the fiber core. To avoid nonlinear interactions, like the self-phase modulation (see section 4.1) which arise in case of high intensity, the final compression of the laser pulse takes place in a SF10 glass rod (see figure 18) which allows a significant larger beam-diameter (2 mm compared to 5 µm) and therefore the intensity of the laser pulses decreases by a factor of 10000.

There are still higher order dispersion of the same sign which are produced by the grating compressor and the fiber [18]. This remaining dispersion will be compensated by a so called "pulse shaper". A pulse shaper consists of a Spatial Light Modulator (SLM) which is placed in the focal plane of a "spectrometer setup" [19] (see section 4.5.

The compressed laser pulses with a duration less than 100 fs are used for TEO:
The initial linear polarized laser becomes elliptical while passing the crystal in presents of the electron bunch. A quarter wave plate turns linear polarized light into circular and vice versa. A thin film polarizer separates the two orthogonal polarization components which are then measured by two detectors. The electro-optical effect decreases one polarization while increasing the other. In this way the polarization carries the full information for the timing read-out. The electro-optical effect is detected by an optical imaging system which produces

a 1:2 imaging of the crystal (see section 3.2) onto the detectors for the two polarization components. The crystal is tilted by an angle of 45° with respect to the laser beam. The expected resolution of the imaging system is 5 µm, which is close to the diffraction limit of the optics.

The detection of the change of polarization, which carrys the timing information, is separated into two steps. The first step is an approximated timing between the Ti:Sa and the electron bunch realized by detecting the laser pulses and the optical transition radiation (OTR) of the electron bunches a fast photo diode. Using a scope the relative timing can be adjusted with a precision of about 100 ps. The second step is the detection system which includes an intensified CCD camera or a gated CMOS detector array consisting of 1024 photo diodes arranged in a line which can be gated down to 20 ns. The smallest gate width of the CCD camera is 5 ns. A difficulty is that the fiber is influenced by the ambient temperature which causes a change of the optical path length and consequently a jitter in the pulse duration. To keep the optical path length of the fiber constant a system is installed which uses the technique of cross-correlation. A cross-correlation needs two pulses (see section 3.5). Therefore, a beam splitter in the tunnel setup reflects 50% of the laser beam intensity back into the fiber. These laser pulses are then correlated with laser pulses which are separated by a Faraday Rotator and a polarizer from the original non-modulated laser beam (see figure 17) and compressed temporally by a prism compressor to achieve a higher resolution. The cross-correlator signal is monitored by a photomultiplier. The correlation signal controlls a motor driven optical delay stage which compensates the temperature induced path length difference (see figure 17 and figure 18). A photography of the setup in the laserhutch is shown in figure 19 and a photography of the setup in the tunnel is shown in figure 20.

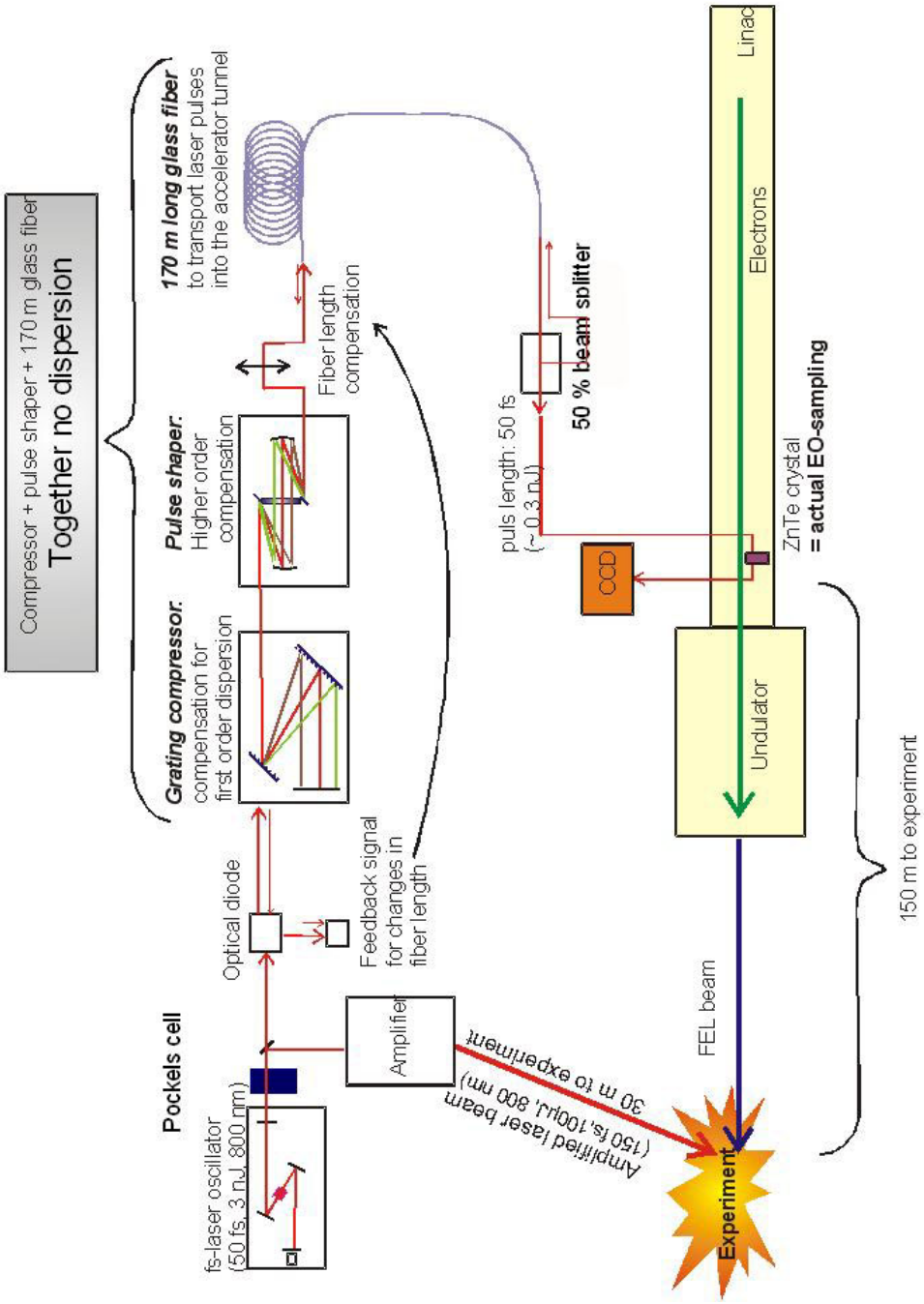

Figure 16: Overview of the setup of the Timing Electro Optic Experiment

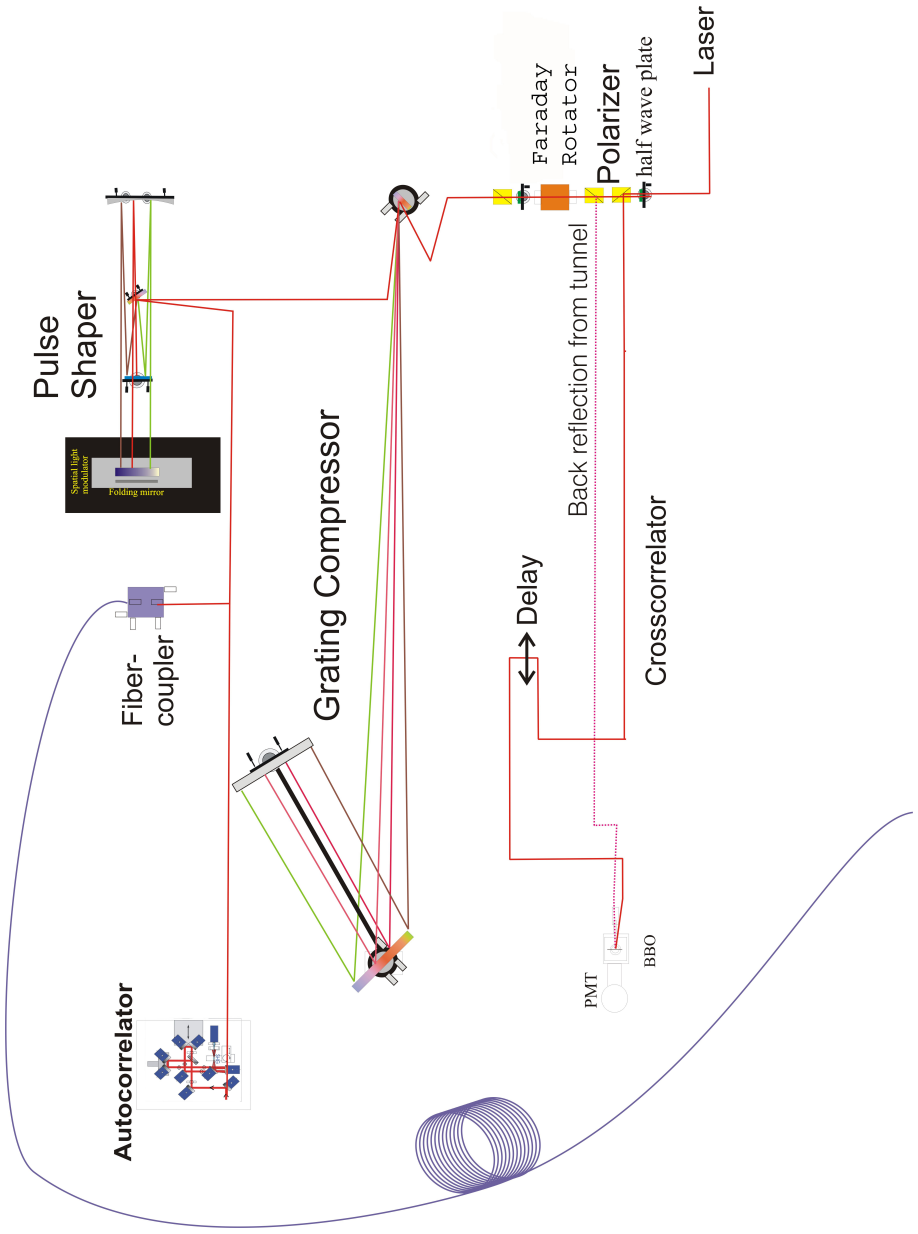

Figure 17: Detailed Overview of the TEO experiment in the laser hutch. The setup includes the grating compressor, the SLM, the setup for the cross-correlation and the motorized delay-stage.

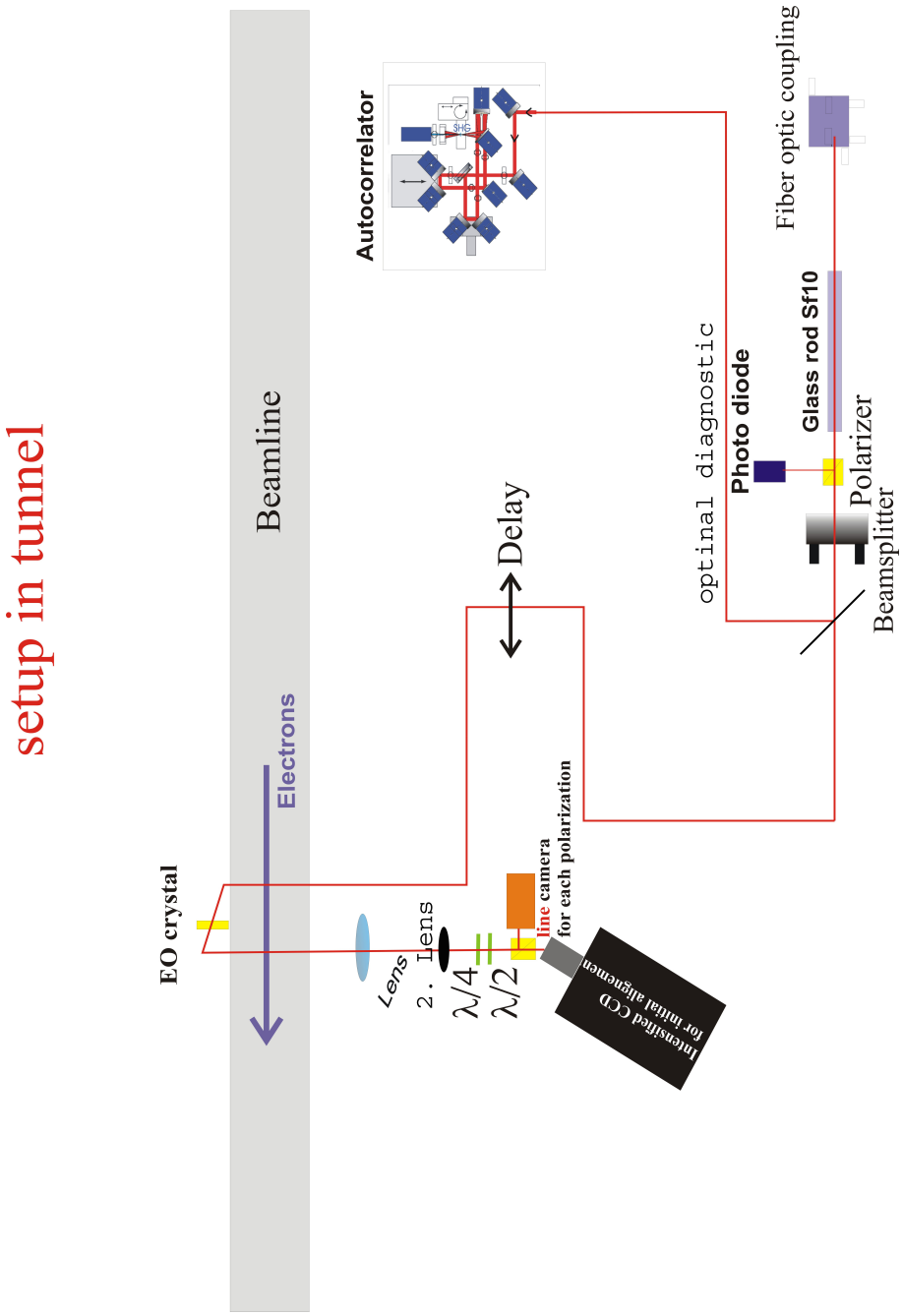

Figure 18: Detailed Overview of the TEO experiment in the tunnel. This setup includes a delay stage for timing of the laser pulses, the crystal and diagnostic tools.

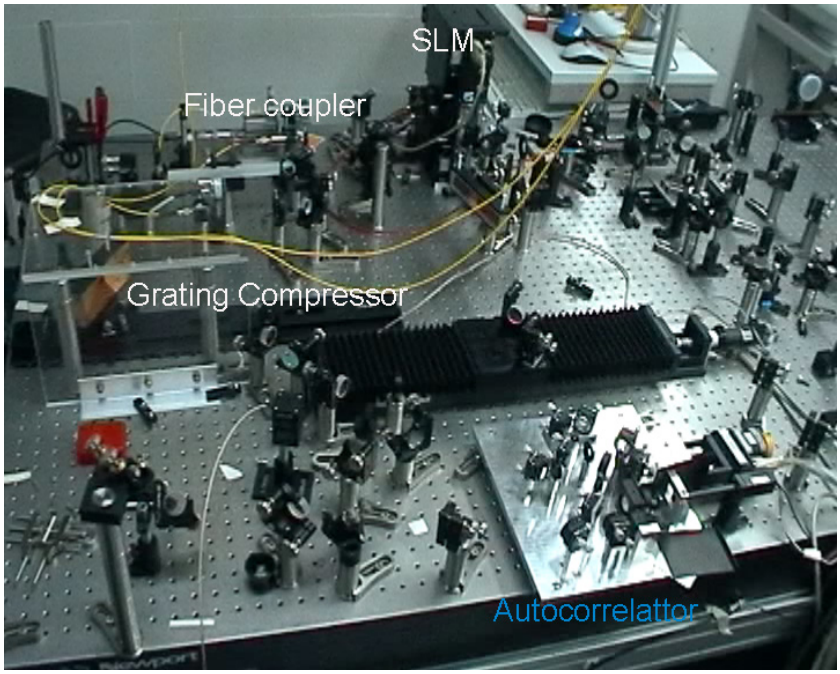

Figure 19: Photography of the TEO setup in the laserhutch, the setup includes the grating compressor, the shaper and the fiber coupler.

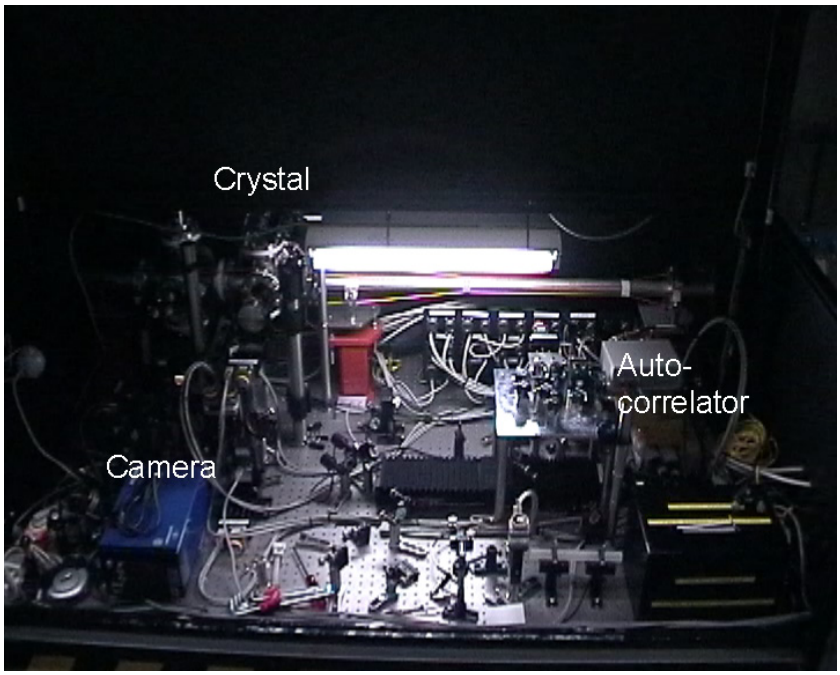

Figure 20: Overview of the experimental setup in the tunnel. This setup includes a motorized delay stage for timing between the laser pulses and the electron bunch, the crystal and diagnostic tools. Several motors to realize the remote control of the laser transport and polarization an intensify camera and an auto-correlator.

3.2 The Timing Electro Optical Sampling Imaging System

The imaging system consists of two achromatic lenses. The first lens has a diameter of 1 inch with a focal length of 150 mm and the second has a diameter of 2 inch with a focal length of 300 mm. The focal lengths of the lenses are chosen such that they realize a 1:2 imaging. The specifications of the lenses are the result of a "Zemax"[1] simulation. The goal for the simulation was to design an imaging system which has a 1:2 magnification and a large solid angle for the light propagating through it. Another point optimized by the simulation is the reduction of imaging errors caused by the lenses. The simulation shows that the use of achromatic lenses is the best way to avoid imaging errors. Achromatic lenses have no color aberation and low other aberations. Also the rotation of plan-convex lenses was simulated by "Zemax", it shows the importance of the correct orientation and that the orientation with respect to the planar or convex site of the lenses is not uniform.
The ZnTe crystal is illuminated by the laser, the resulting image is detected by a camera. The camera has a CCD chip with 640x480 pixels and has been tilted by $50° \pm 5°$ with respect to the direction of the propagation of the laser beam. This ensures a complete transverse imaging of the crystal without the loss of spatial resolution. Cracks on the ZnTe crystal surface are imaged as sharp lines. These sharp lines have been analyzed by plotting the intensity a function of pixel number along the x-axis (see red line in figure 21).
The resolution of the imaging system was also simulated with "Zemax" [30] using the specifications of the lenses (bending radius, material, etc.). From the simulation, a diffraction limitation of 5 µm FWHM for the imaging system has been found. The analysis of figure 22 shows that the slope of the imaged crack is 2.5 ± 0.5 pixels. This determines the resolution of the TEO imaging system to 12.5µm $\pm$ 2µm. Finally, an intensified camera has been installed with a minimum exposure time of 5 ns, which allows the observation of single pulses. A first picture of a single laser pulse is shown in figure 23.

[1] Zemax is a simulation program which allows to simulate nearly every optical setup.

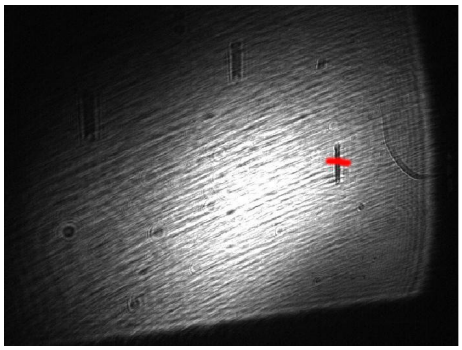

Figure 21: Photograph of the ZnTe crystal, which is placed in the tunnel (see figure 6), has been taken by the TEO imaging system. The camera is a Basler camera with a [480x640] pixel CCD chip. The camera is tilted by $50° \pm 5°$ with respect to the direction of the propagation of the laser beam. One of the sharp lines (crack) in the photograph has been analyzed to determine the intensity as a function of the pixels along the red line. The result is shown in figure 22.

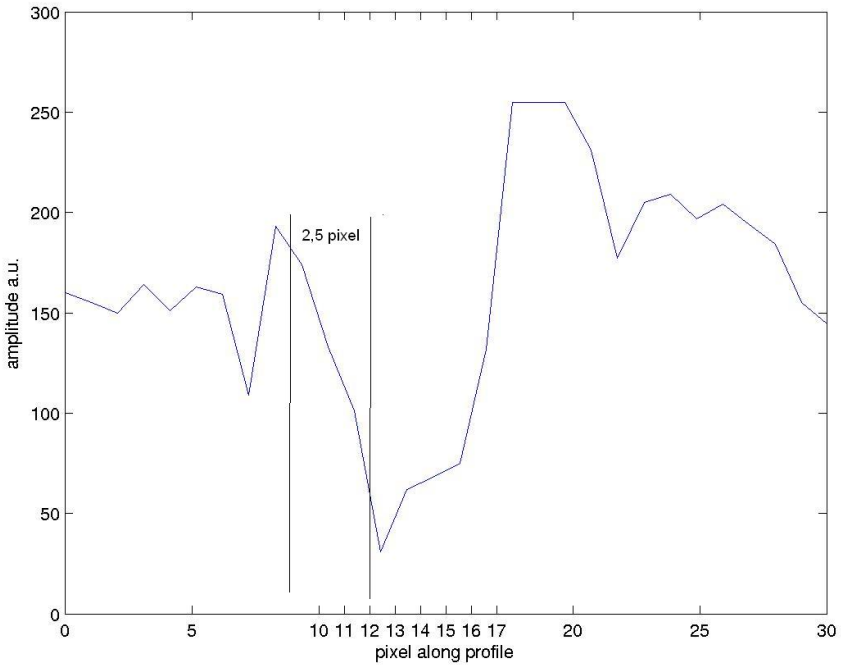

Figure 22: This figure shows the intensity along the red line in figure 21. The crack is visible between pixels 9 and 13. The slope there of 2.5 ± 0.5 pixels is defined by optics, which is in good agreement with the simulations.

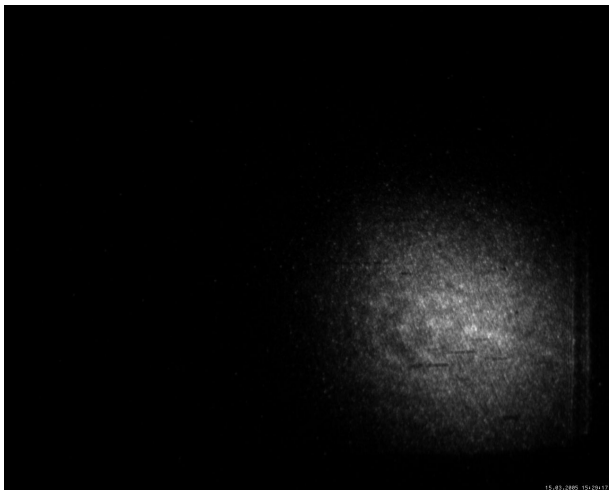

Figure 23: Photograph of the ZnTe crystal, which is placed in the tunnel (see figure 6), taken by the TEO imaging system. The camera is a NanoStar intensified camera. The photography shows a single laser pulse.

3.3 Diagnostic of the laser pulses

3.4 Auto-correlation

The following two sections describe a category of detectors, which allows the detection of the pulse profile by correlation methods using second harmonic generation. These detectors allow the determination of the FWHM for a given Gaussian pulse profile and the pulse structure to a certain extend.

Nonlinear detection

The pulse length is measured with an auto-correlation technique using a nonlinear effect, the multi-photon-absorption in a crystal.
Mathematically, the detected signal S_{NL}^n of a 2-photon-absorbtion is given by:

$$S_{NL}^n \propto \int_{-\infty}^{\infty} I^n(t;x,y)dt, \qquad \forall : n > 1 \tag{72}$$

To get information about the pulse duration, one has to regard the nonlinear integrator in equation 72. The integral increases with the peak intensity in case of a constant energy. And the peak intensity depends on the pulse duration, so that a decreasing pulse duration causes an increasing signal. For $n = 2$ one has second harmonic generation. This is a process which will be described more precisely in the following section.

Second Harmonic Generation

The effect describes a process, in which two photons with the same angular frequency ω are combined to a single photon with twice the original frequency while propagating through a suitable material.
In contrast to linear optics which is based on harmonic oscillation, the nonlinear optic contains strong inharmonic oscillation of the electrons in nonlinear-material. In this inharmonic case, the emitting dipoles can radiate energy at frequencies which are integer multiples of the original frequency.
The inharmonic oscillation is a result of high intensity, which can be achieved by using amplified pulses or tight focusing onto non-linear material the crystal. The electric field of the pulses, which propagate through the medium, is no longer negligibly small compared to typical local fields (inner atomic/molecular fields and crystal fields) in the medium. The result is a pulse dependent change of the properties of the medium. The induced polarization is therefore given by:

$$P = \epsilon_0\chi(E)E = \epsilon_0\chi^{(1)}E + \epsilon_2\chi^{(2)}E^2 + \epsilon_0\chi^{(3)}E^3 + ... + \epsilon_0\chi^{(n)}E^n + ..., \tag{73}$$

where $\chi^{(n)}$ are the nonlinear optical susceptibilities of n^{th} order and $\chi^{(1)}$ is the linear susceptibilities. The linear susceptibilities are much larger than the higher

nonlinear optical susceptibilities. Therefore the electric field has to be accordingly high [27].
For SHG it is enough to focus onto the first two terms of the polarization, because the higher orders can be neglected. Thus, equation 73 can be reduced to the first two terms. The polarization is assumed to be in the x-direction:

$$P_x = \epsilon_0 \chi^{(1)} E_x + \epsilon_2 \chi^{(2)} E_x^2 \quad . \tag{74}$$

For linear polarized light the electric field can be written as follows:

$$E_x = E_{xo} cos(2\pi f t) = E_{xo} cos(\omega t) \quad , \tag{75}$$

where f is the frequency of the incident light and E_{xo} the amplitude of the electric field. Insert equation 75 into equation 74 yields:

$$\begin{aligned} P_x &= \epsilon_0 \chi^{(1)} E_{xo} cos(\omega t) + \epsilon_2 \chi^{(2)} E_{xo}^2 \cos^2(\omega t) & (76) \\ &= \epsilon_0 \chi^{(1)} E_{xo} cos(\omega t) + \epsilon_2 \chi^{(2)} E_{xo}^2 \frac{1}{2}(1 + \cos^2(2\omega t)) \quad . & (77) \end{aligned}$$

The polarization can be rearanged in orders of ω:

$$P_x = P_x'(\omega) + P_x''(2\omega) + const. \tag{78}$$

with the discrete frequencies ω and 2ω. Thus, SHG generates a frequency doubling which will be used in an auto-correlator.

Principles of Auto-correlation

To characterize ultrashort laser pulses it is necessary to have a very fast detector which is not yet available, but the ultrashort laser itself is very fast and so it makes sense to use the laser for characterization. This can be achieved by correlating the laser with itself.
To auto-correlate the laser pulse, the beam is separated by a beam-splitter. One part of the beam passes a variable delay and the other has a fixed path length. The two pulses are overlapped spatially in some instantaneously responding nonlinear optical medium, such as a SHG crystal. The resulting intensity is given by:

$$I_{sig}^{SHG}(t, \tau) \propto I(t) \cdot I(t - \tau) \quad , \tag{79}$$

which is valid for very fast detectors. For common detectors one has to calculate time average:

$$a(\tau) = \int_{-\infty}^{\infty} I(t) \cdot I(t - \tau) dt \quad . \tag{80}$$

In case of a Gaussian pulse the intensity is proportional to the convolution of two Gaussian:

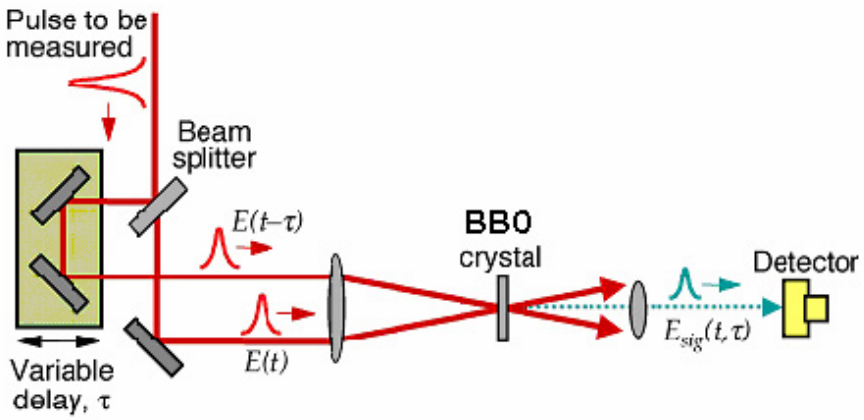

Figure 24: Propagation of a laser pulse through the auto-correlator

$$\begin{aligned} a(\tau) &= I_0^2 \cdot \int_{-\infty}^{\infty} e^{-\frac{t^2}{2\sigma^2}} \cdot e^{-\frac{(t-\tau)^2}{2\sigma^2}} dt \\ &= I_0^2 \cdot e^{-\frac{\tau^2}{4\sigma}} \cdot \int_{-\infty}^{\infty} e^{-\frac{(t-\tau/2)^2}{\sigma^2}} dt = ctc \cdot e^{-\frac{\tau^2}{4\sigma^2}} \end{aligned} \tag{81}$$

As the standard deviation increases two times, the pulse duration increases by $\sqrt{2}$.

The idea the auto-correlation is to transfer the pulse duration of a laser into an intensity signal and it also allows as shown in figure 24 transferring information of the time into space information. Figure 24 shows the development of the pulses propagating through the auto-correlator. The time delay τ is realized by a motorized delay stage table, so a transformation from length information into the necessary time information is the result. To get an information about the pulse duration as a function of the intensity, one uses SHG. For this thesis a Beta Barium Borate (BBO) crystal is used to produce SHG.

3.5 Cross-correlation

The main difference between auto-correlation and cross-correlation is that cross-correlation uses a reference pulse; auto-correlation is therefore a special case in which the reference pulse is the same as the laser pulse to be observed. The principle of cross-correlation is the same; one correlates two ultrashort laser pulses by spatially and temporally overlapping the pulses in a SHG crystal. The intensity is given by:

$$a(\tau) = \int_{-\infty}^{\infty} I(t) \cdot I_{ref}(t-\tau) dt \tag{82}$$

An other difference is the correlation intensity curve which is always symmetric in case of 2^{nd} order auto-correlation and can be asymmetric in the cross-correlation case. The auto-correlation intensity curve is symmetric, because

$$I_{ref}(t) = I(t) \tag{83}$$

so that

$$\int I_{ref}(t-\tau) \cdot I(t) = \int I_{ref}(t) \cdot I(t-\tau) \tag{84}$$

but in the case of the cross-correlation it is:

$$\int I_{ref}(t-\tau) \cdot I(t) \neq \int I_{ref}(t) \cdot I(t-\tau). \tag{85}$$

3.6 Creating a specific Grating Compressor

A grating compressor exists of two gratings and a folding mirror. A grating compressor is used to compress laser pulse e.g. to compensate dispersion. The grating compressor operates at a central wavelength of 800 nm. The angle of incidence is chosen to be in the range of $45° \pm 20°$ which is a value of experience. It allows a compact setup without cut-offs of the laser spectrum caused by a grating. The prerequisites on the grating compressor setup are:

- the grating compressor has to compensate the dispersion caused by the fiber
- the gratings shall be able to transmit a bandwidth of 60 nm FWHM
- the commercial available grating size is 14 cm
- the third order dispersion caused by the grating compressor has to be small

Thus the grating periods are determined by The Littrow angle, which delivers the angle of incidence with the highest reflectivity, is determined by the grating periods and is a kind of grating compressor with a back-reflecting geometry. The back-reflecting geometry is a often used for grating setups in spectrometers. But it is not practical for the alignment. More practical is an angle of incidence which is over 8° larger then the Littrow angle. The Littrow angle α_L is calculated by:

$$\alpha_L = \arcsin\left(\frac{\lambda_c}{2 \cdot g}\right) \tag{86}$$

Where λ_c is the central wavelength and g is the grating constant. The grating periods and its Littrow angle are presented in the table 3.

grating constant [1/mm]	grating period [nm]	Littrow angle	Littrow angle +8°
1200	833	28.7°	37°
1500	667	36.8°	45°
1800	555	46°	54°

Table 3: Littrow angle to determine the angle of incidence

Now the grating compressor shall be able to transmit two times the FWHM of 30 nm at 800 nm central wavelength to avoid a cut-off of the pulse spectrum. This condition delivers the reflection angles $\phi(\lambda)$ for "red" and "blue" borders. It follows with the incidence angle β:

$$\phi(\lambda) = \arcsin\left(\frac{\lambda}{g} - \sin(\beta)\right) \tag{87}$$

grating constant	angle of incidence	$\phi_{red}(830nm)$	$\phi_{blue}(770nm)$	opening angle γ
1200 [1/mm]	37 °	23.2°	18.9°	4.3°
1500 [1/mm]	45 °	32.5°	26.6°	5.9°
1800 [1/mm]	54 °	43.3°	35.3°	8.0°

Table 4: Reflection angles for red and blue borders at 2FWHM

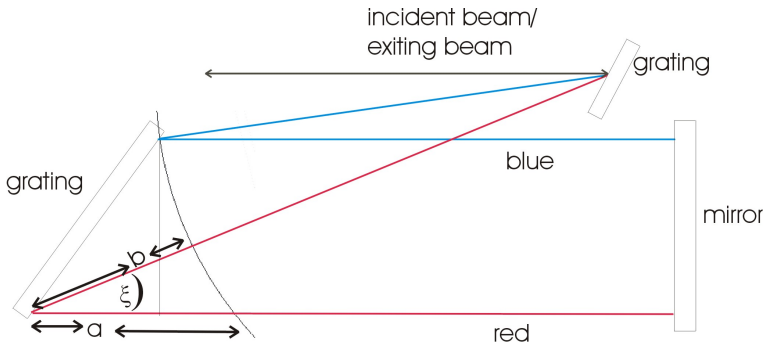

Figure 25: Setup of a grating compressor showing the PLD. The distance a is smaller than the distance b but to have an overview about the expected PLD it is enough to approximate $a \approx b$

The possible grating compressor setups can be drawn with these values to calculate the dependence of path length difference (PLD) as a function of grating size c and grating distance d (see figure 25).

For the small angle ξ between the second grating and the normal of the reflecting mirror the two distances a and b are approximately equal. For a single pass of the laser beam through the grating compressor, one gets:

$$a \approx b \rightarrow PLD = 2 \cdot a. \tag{88}$$

The approximation can be done in our special case by the given range of angles of incident. The dependence of grating size on the PLD can be calculated by:

$$c \approx \frac{PLD}{2 \cdot \cos(90° - \phi_{red})} \tag{89}$$

From the drawing it can be seen that the function between grating distance d and PLD is given by:

$$d \approx \frac{PLD}{2} \cdot \frac{\cos\left(\frac{\phi_{red}+\phi_{blue}}{2}\right)}{\sin(\gamma)\cos(90° - \phi_{red})} \tag{90}$$

Table 5 shows the calculated values in units of PLD which means that the calculated value, for example the value 14 for a grating with 1200 lines/mm in

grating constant [1/mm]	grating distance [PLD]	grating size [PLD]
1200	14	1.3
1500	8	0.9
1800	4	0.7

Table 5: Grating distance and grating size in units [PLD].

case of the grating distance means that the grating distance has to be 14 times of the whished PLD. Using the grating with 1800 1/mm seems to be good, because of its compact setup.
The next step is to calculate the PLD. The grating compressor has to compensate the dispersion of a 170 m long fiber. This delivers a FWHM after the fiber of 540 ps for $\Delta\lambda$ =30 nm. The compressor shall transmit twice the FWHM and the beam goes twice through the setup one gets with the velocity of light c and

$$2 \cdot PLD \approx 2 \cdot FWHM_{\tau} \cdot c \tag{91}$$

follows a PLD of 16 cm. This PLD value allows to calculate the grating distances and the grating sizes of the different gratings with the values shown in table 5. Table 6 shows the grating distance and grating size depending on the grating constant. The grating distance can also be calculated by Lab2. The simulation

grating constant [1/mm]	grating distance [cm]	grating size [cm]
1200	224	21
1500	128	14.4
1800	65	11.2

Table 6: Grating parameters

includes the laser with a Gaussian pulse profile, the fiber and an intelligent grating compressor. The grating size is taken out of table 6. The bandwidth in the simulation is $\Delta\lambda$ = 60 nm, the distance between the grating and the mirror is 600 mm and the angle of incidence is taken out of table 4. The results are presented in table 7.

The differences between the calculated and the simulated values are inside the tolerance, because the differences can be balanced by the alignment. The grating size limits geometrically the spectrum of the passing laser pulse, therefore the spectrum can be cut off at its borders.
To analyze this effect the simulation can be extended by a spectrometer which will show immediately a cut-off of the pulse spectrum (see figure 26).
The maximum commercially available grating size is 14 cm and the distance between mirror and second grating is 600 mm. The other settings are taken from

grating constant [1/mm]	angle of incidence	grating distance [cm]
1200	37°	205
1500	45°	114
1800	54°	63

Table 7: Grating distance calculated by Lab2

grating constant [1/mm]	2^{nd} order dispersion $[10^6 fs^2]$	TOD $[10^7 fs^3]$
1200	-6.23	1.09
1500	-6.1	1.39
1800	-6.23	1.98

Table 8: Table for higher order of dispersion.

the tables before.

Another criteria is the spectra behind the grating. The spectra for different grating constants, simulated with Lab2, are shown in figure 26. The grating with the highest grating constant cuts-off the spectrum for wavelength above 838 nm in contrast to smaller grating constants, 1200 lines per mm grating, where 10% off the spectrum is cut.

A simulation which includes a grating compressor and a 170 m long dispersive element in an arrangement with a gaussian laser beam shows the run of the intensity curve behind the dispersive element and the grating compressor to show effect of the grating compressor on a dispersive laser beam. Therefore the 1500 lines per millimeter grating is used in the simulation.

The curve in figure 28 shows how well the grating compressor works, it could decrease the FWHM down to 344 fs (see figures 27 and 28).

But the curve also show that the intensity curve is no more a Gaussian compared to the initial pulse, because there are hundreds of ancillary-pulses caused by higher order of dispersion of the grating compressor and the fiber.
The major contribution of the laser pulse distortion are of second order dispersion (GVD) and the third order dispersion (TOD) which are calculated by equations 57 and 58.

The fiber itself also produces TOD, this can be calculated by the Sellmeier equations [18].
The table 8 shows that an increasing grating constant means an increasing TOD and the TOD also depends on the angle of incidence.
For fiber glass SQ1 k''' is $270 fs^3/cm$, the TOD is just the product of k''' and the

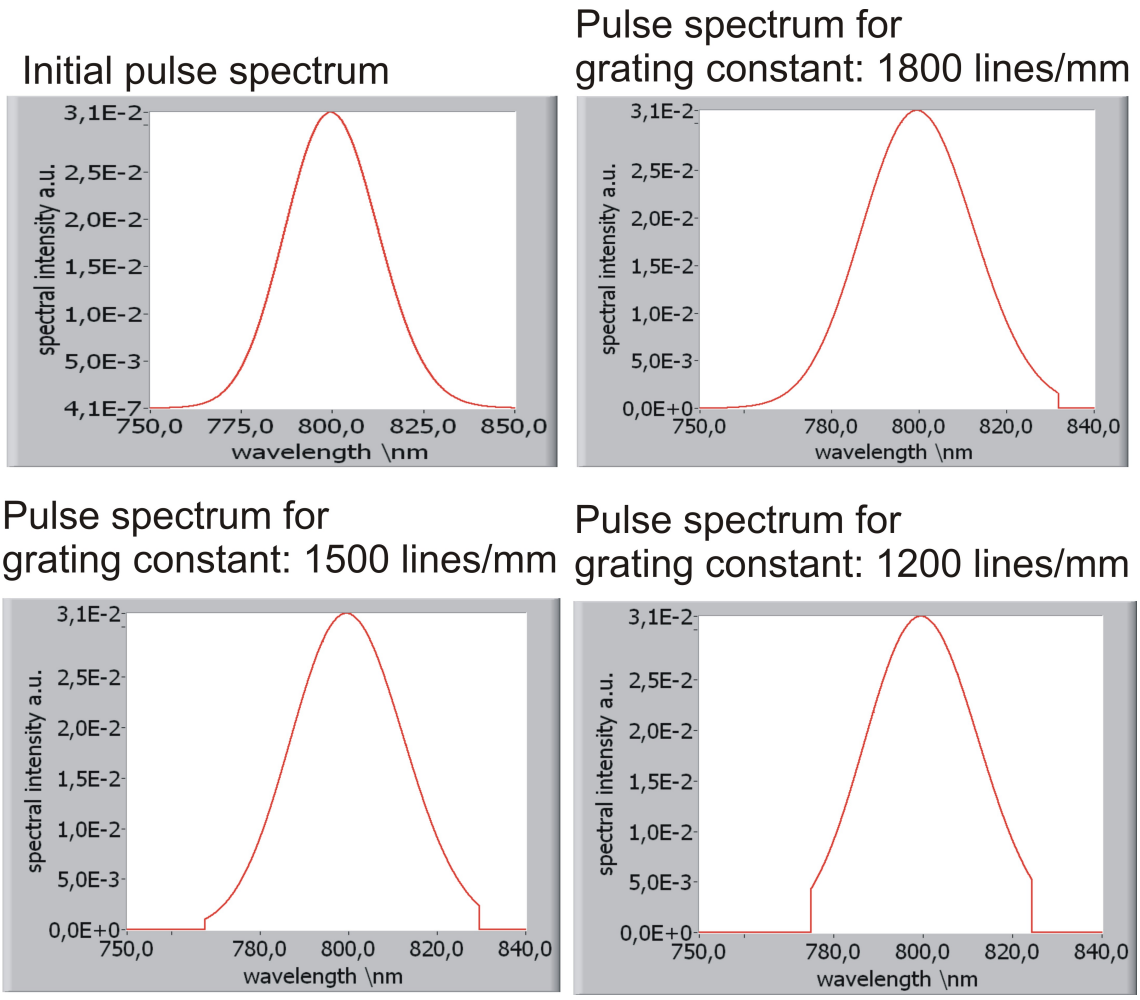

Figure 26: Spectra of the laser pulse before and behind the dispersive element and the grating compressor for different gratings.

fiber length ($l = 170\,\mathrm{m}$), thus the TOD for the fiber is $0.46 \cdot 10^7 fs^3$.
The TOD of the grating compressor is dominating.

In conclusion the most reasonable grating compressor setup is with the 1500 lines per millimeter grating at an angle of incidence of 45°, because the required grating distance and the grating is acceptable small and is available at the common manufactories. A 1800 lines per millimeter grating would be more compact, but the TOD is to high and the grating size has to be larger than 14 cm. In order to compensate the higher orders dispersion; a pulse shaper is required.

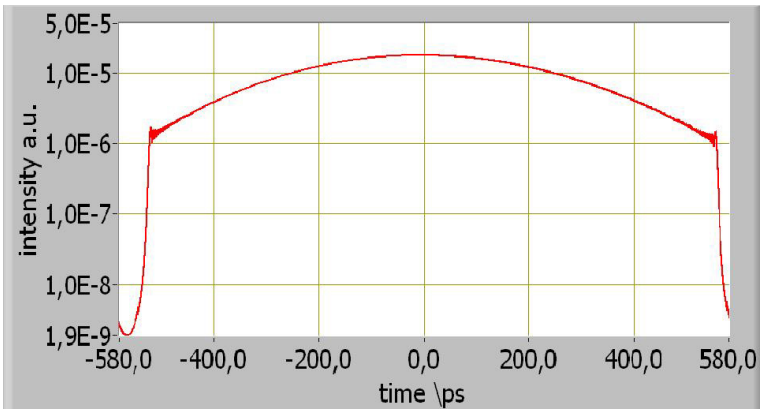

Figure 27: This intensity curve shows the simulated pulse profile of the laser after passing the 170 m long fiber. The FWHM is broaden up to 540 ps and has no Gaussian profile. The intensity has a logarithmic scale.

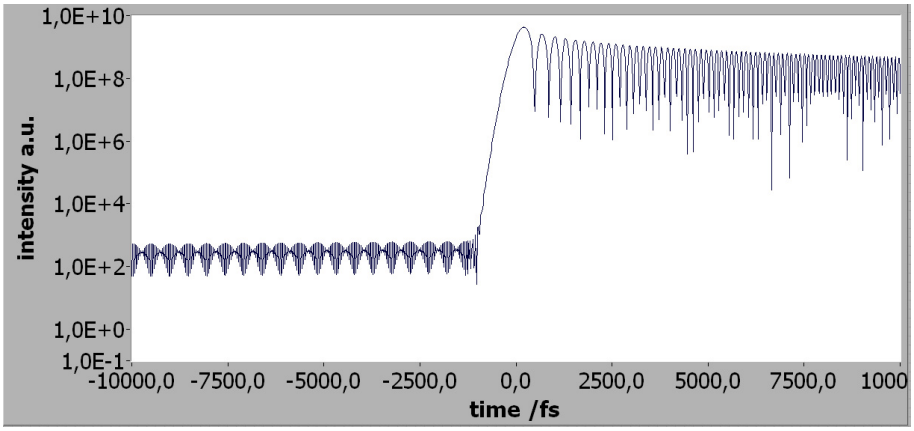

Figure 28: This Lab2 plot shows the simulated pulse profile after the compression by the grating compressor. The higher orders of dispersion are very well presented in this diagram. The compressor is able to compress the pulse back to a FWHM 344 fs, but generates hundreds of ancillary pulses. The intensity has a logarithmic scale.

3.7 Principles of a Spatial Light Modulator

There are two kinds of pulse modulation, the amplitude modulation and the phase modulation.
Today, pulse shaping by a SLM is one of the most common method to create complicated laser pulse patterns [10]. In this work, the SLM is used to recompress the laser pulse by compensating higher orders of dispersion. The SLM is controlled by an optimization algorithm, which uses second harmonic generated reference signal. It is also possible to write several patterns to the SLM to form the laser pulse in the desired shape. This will be used to test the SLM setup and to calibrate the SLM control. The SLM setup will also be simulated with Lab2, to find optimized settings and setup parameters.
Comparing with former SLMs, the big advantages of the pulse shaper SLM-S 640/12 , which is used in the TEO experiment, is the high resolution of 640 pixel and the transmission of up to 90% and the high damage thresholds of $300\,\mathrm{GW}/cm^2$.
With an active area of $6.4\,cm^2$ the SLM is able to perform temporal shaping of amplified laser pulses with up to several joules of pulse energy.

Setup and functionality of the Spatial Light Modulator

To understand the functionality in experiment and theory, it is necessary to know more about the physics of the SLM. The knowledge gained will allow the determination of the limits of the SLM and will show, how well the SLM can be used in the TEO experiment.
The SLM is based on a nematic liquid crystal. Liquid crystals (LC) comprise of longish molecules, which are orientated like unit cells in a crystal. The difference is that the LC molecules do not have a fixed position. Nematic stands for a preferred orientation of the LC molecules, which orientate almost parallel to each other, so that a nematic LC is an optical anisotropic material.
Every LC modulator uses the property that the LC molecules orientation can be controlled by an external electric field.
A cut of a LC-cell is presented in figure 29.

The LC-cell consists of two glass-plates, transparent Indium Tin Oxide (ITO) electrodes and the nematic LC.
The glass-plates with the index of refraction n_{GP} have a thickness of z_{GP}, a distance of z_{LC} and include the liquid crystal. The ITO electrodes have two functionings, the first functioning is to give the liquid crystal a preferred orientation. This is done by a special surface structure of the electrodes. This structure forces the orientation of the molecules along the special structure. The second functioning is to initialize an electric field in the LC cell.
Figure 29 shows the behaviour of the longish molecules with and without an electric field between the electrodes. In case of no electric field, the molecules

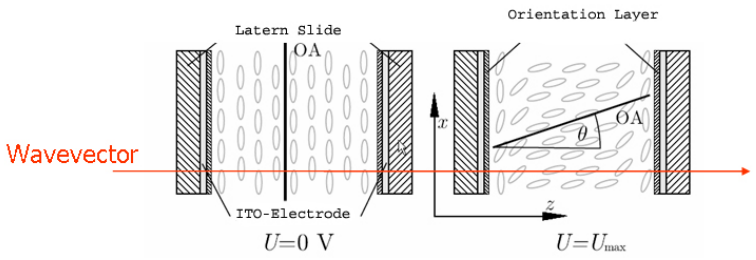

Figure 29: This picture shows a top-view of the LC matrix of the SLM. OA is thereby the optical axis and ITO means Indium Tin Oxide. [10]

are orientated along the x-axis, and with increasing voltage at the electrodes the molecules become more and more tilted. So the optical axis is tilted in z-direction. An incident wave propagates through the cell in z-direction, so that the angle θ between optical axis and propagation direction decreases by increasing voltage. The result is a voltage dependent index of refraction n_{LC} for a wave, which propagates in z-direction with a polarization in the extraordinary direction (x-axis), because the liquid crystal is a dispersive, uniaxial birefringent medium.
With the ordinary index of refraction n^o_{LC} and the extraordinary index of refraction n^e_{LC} of the liquid crystal, the effective index of refraction n_{LC} can be calculated as a function of the voltage U between the electrodes and the frequency ω of the incident light [10]:

$$\frac{1}{n^2_{LC}(\omega,U)} = \frac{\cos^2\theta(U)}{\left(n^o_{LC}\right)^2(\omega)} + \frac{\sin^2\theta(U)}{\left(n^e_{LC}\right)^2(\omega,U)}. \tag{92}$$

If light with frequency ω propagates through a dispersive element, the spectral phase $\phi(\omega)$ will change in condition to the length z of the dispersive element and its index of refraction $n(\omega)$. So with

$$\phi(\omega) = k(\omega)z = \frac{\omega}{c}\cdot n(\omega)z, \tag{93}$$

where c is the velocity of light, follows for the phase-shift:

$$\Delta\phi = \frac{\omega}{c}n_{LC}(\omega,U)\cdot z_{LC} + 2n_{GP}(\omega)\cdot z_{GP} \tag{94}$$

$$= \underbrace{\frac{\omega}{c}\Delta n(\omega,U)\cdot z_{LC}}_{\Delta\phi(\omega,U)} + \underbrace{\frac{\omega}{c}n^o_{LC}(\omega)\cdot z_{LC}2n_{GP}(\omega)\cdot z_{GP}}_{\Delta\phi_{fix}(\omega)} \tag{95}$$

with $\Delta n(\omega,U) = n_{LC}(\omega,U) - n^o_{LC}(\omega)$. Thus, the phase delay is divided into two parts, one is the voltage dependent part $\Delta\phi(\omega,U)$ and a fixed value part $\Delta\phi_{fix}(\omega)$. $\Delta\phi(\omega,U)$ has its maximum for $U = 0\,\mathrm{V}$. The fixed phase delay $\Delta\phi_{fix}(\omega)$ is very small because of the thin glass-plate and will be compensated by the pulse shaper

setup.
The liquid crystal and the electrodes form a LC matrix with 640 pixels; a schematic overview is given in figure 30:

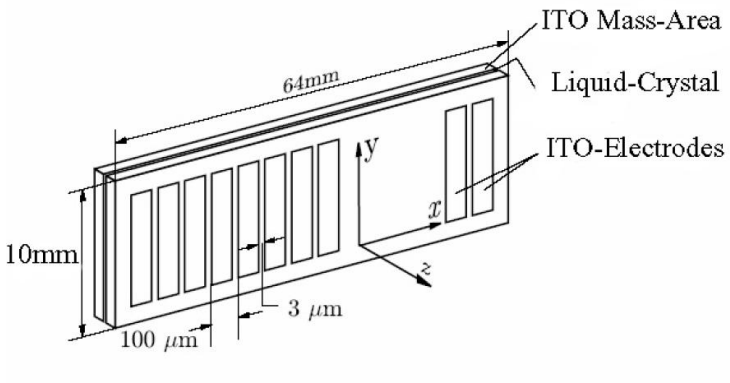

Figure 30: Scheme of the phase-modulator SLM-S 640/12. The Idium-Tin-Oxide(ITO) - control electrodes for the 640 pixel are inside the glass-base. The mass-electrode is placed over the full area of the other glass-base.

The matrix is 10 mm high and 64 mm long. The electrodes of each pixel are 97 µm wide and have a gap of 3 µm between each other. The glass-plate are $z_{GP} =$ 1.5 mm thick and include a liquid crystal film of $z_{LC} = 9$ µm. These values are important for the determining of the limits of the SLM-S 640/14 and to configure a setup, which is optimized for the TEO experiment. A high transmission of each optical element in the TEO setup is very important to realize a laser spot at the crystal with sufficient intensity. The transmission curve of the SLM in condition to the wavelength is shown in figure 31:

This curve shows satisfactory transmission (92%) at 800 nm. This is reached by the glass-plates, which are anti-reflective-coated for this wavelength.

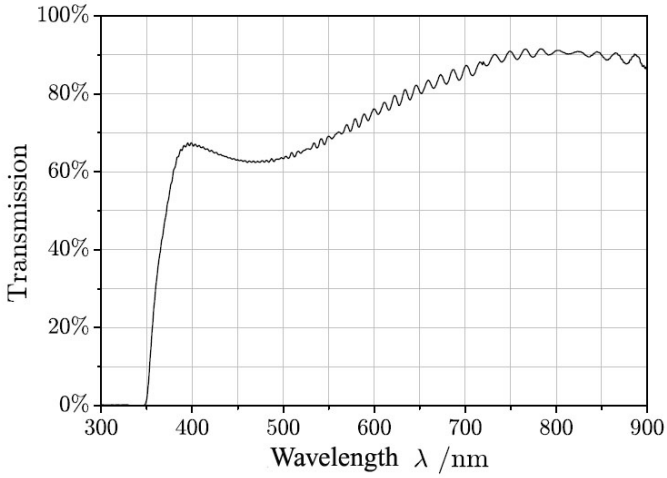

Figure 31: Transmission curve of the SLM-S 640/14 measured at a wavelength regime from 300 nm to 900 nm. The liquid crystal absorbs below 300 nm. The oscillation of the transmission curve at larger wavelength is a result of the Fabry-Perot effect, which is established by the 9 µm thick LC-layer between the two glass-plates.[31]

3.8 The Spatial Light Modulator Setup

To realize amplitude or phase modulation by a SLM, it is necessary to map the laser spectrum to a Fourier plane which can be done by a special setup. This section will lead through different setups to find an optimal SLM setup for the TEO experiment. Another condition is that the setup has to be dispersion free, generally speaking, the setup, apart from the SLM itself, should have no influence on the pulse shape.
The most common setup, which realizes these conditions, is the 4f-stretcher. The setup is shown in figure 32.

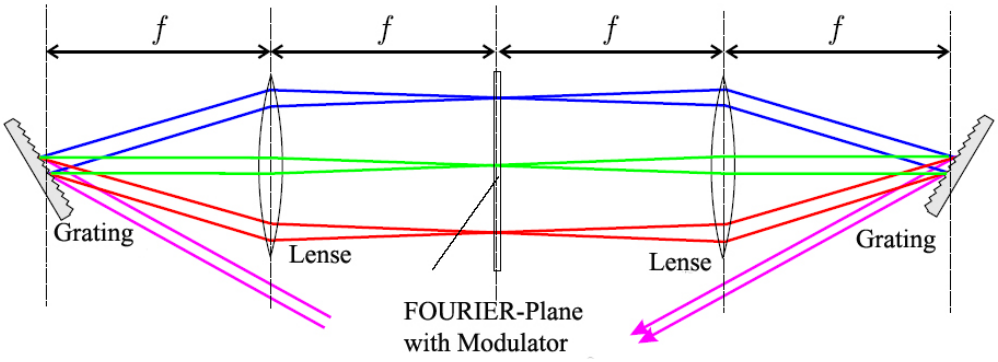

Figure 32: Setup of a 4f-stretcher: The gratings and the lenses are placed back-to-back with a distance of the focal length f of the lenses. A spatial image of the laser spectrum is produced in the Fourier plane between the two lenses. [10]

The figure explains the name $4f$-stretcher, because gratings and SLM stands in the foci of the lenses, so the whole setup is $4f$ long, where f is the focal length. The $4f$-stretcher is dispersion free, so that the pulse exits the setup without chirp. But the lenses cause chromatical and spherical aberration.
To avoid this additional pulse shaping effect, one has to replace the lenses by focussing mirrors, like cylindrical mirrors. Two possible setups for such a reflecting $4f$-stretcher are shown in figure 33.

The cylindrical mirrors for the setup in figure 33 have to be tilted to provide enough place for the SLM, because of this fact and the spherical aberration of the mirror an astigmatism is induced. This off-axis aberration is higher for the short wavelength part of the spectrum in figure 33a, because the reflection angle on both cylindrical mirror is higher than the long wavelength part of the spectrum. An alternative setup is figure 33b, in that case the reflection angles are symmetric. Folding mirrors produce relief. With these folding mirrors the cylindrical mirrors can be used without changing the angle of the optical axis. Therefore, the beam

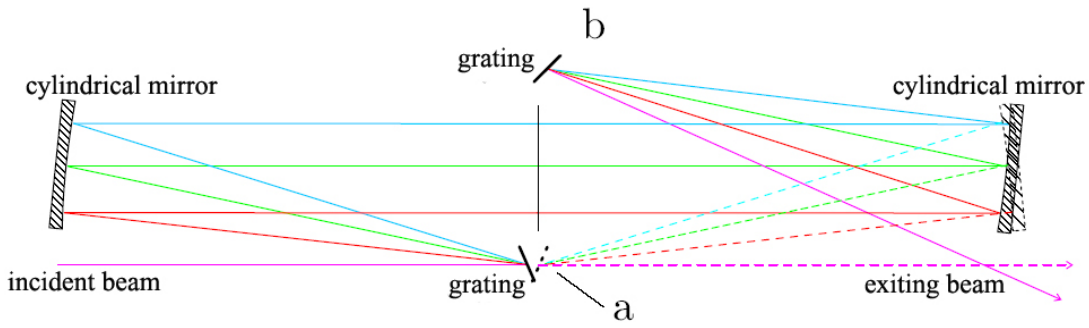

Figure 33: Setup of a 4f-stretcher in off-axis design: a) has in contrast to b) a smaller off-axis-aberration, which is caused by the symmetric angle of refraction of all colors [10].

has to be shifted in height. This is done by vertical tipping of the folding and cylindrical mirrors.

This on-axis setup in figure 34 still has a disadvantage. Parts of the spectrum now have different length of path between the folding and the cylindrical mirror because of the tilted folding mirror. The result is a shift in height in the Fourier plane, so that in case of high beam diameter, the spectral borders can not be formed (see figure 34). The on-axis aberration can not be reduced, but if one can reach an orientation of the folding mirrors along the optical axis, the setup will be complete off-axis aberration free. The following setup in figure 35 fulfils this condition:

The aperture in figure 35 should point up that the incident and exiting beam cross in the Fourier plane outside the spatially spectral image. Such a setup allows the compensation of the angle dispersion of the two gratings.
Another point, which has to be realized by the setup is the compensation of the used material, for example the glass-plates of the SLM produce second and third order dispersion of $\psi_2 = 107fs^2$ and $\psi_3 = 83fs^3$ [**?**] respectively. But the last setup can still be optimized.

Final Setup for the Spatial Light Modulator

The aim in this work is to compensate dispersion by the SLM. The final setup offers the possibility to double the maximum phase-shift, which can be realized by the SLM, by adding a second folding mirror after the SLM (see figure 36). This folding mirror will be called back-reflecting mirror.

The laser goes twice through the LC matrix. Thus, the grating, the cylindrical mirror and the folding mirror are used twice which reduce the cost and required space for the setup.

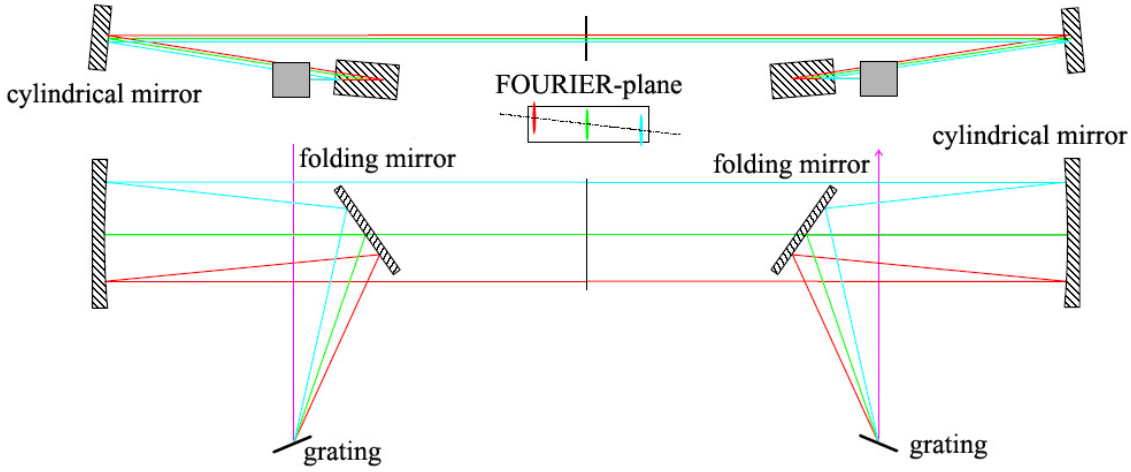

Figure 34: The figure shows a top- and a side-view of a reflective 4f-stretcher in on-axis-design with folding mirror. This setup generates different heights at the Fourier plane, the reason for the different heights at the Fourier plane is the different propagation lengths of the spectral components between the folding mirror and the cylindrical mirror. [10]

A problem for the alignment is the small angle between the incident and the exiting beam. Additionally, space-time coupling causes a spatial chirp. This effect is also minimized by the last configuration. To understand the space-time coupling one has to look closer at the Fourier plane.

Space-Time coupling

The pulse shaper influences the envelope of the initial field $\mathfrak{e}_{in}(\Omega)$ in the frequency domain by the linear filter function $\Xi(\Omega)$, which is a spatial function at the Fourier plane. Thus, the spatial mask-function of the SLM $m(x)$ has to be mapped from the space to the frequency. The position of a frequency components $x(\Omega)$ is not caustic, because the focus of a Gaussian beam is not infinite caustic. That means that every single frequency component has a finite spatial extension on the mask-function $m(x)$. As a consequence, the different spatial zones of a frequency component are influenced by different optical properties. Thus, parts of the beam profile are diffracted in different directions; this causes a temporal modulation, the reduction and the delay entails also spatial modulation of several frequency components. The result is a modulation of the whole exiting pulse. Therefore the spatial and the temporal intensity profile are not independent.
Space-time coupling can be better understood by regarding figure 37.

The figure shows two phase-modulations, a linear and a quadratic one, the

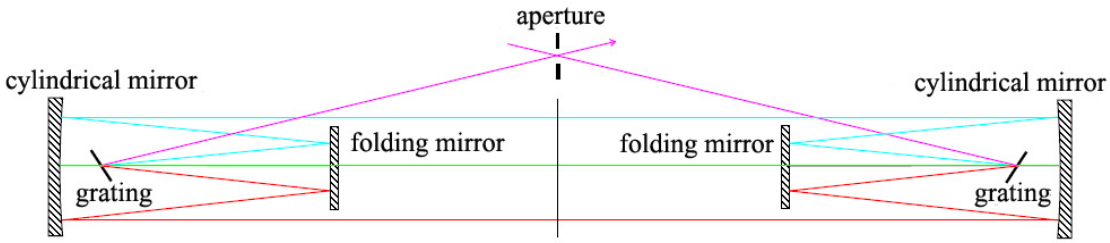

Figure 35: This setup of a 4f-stretcher avoids the angle of the folding mirror against the optical axis. This is a pure on-axis design with 0° of the folding mirrors. [10]

linear phase-modulation is realized by a prism, the quadratic by a lens. The two elements are placed at the Fourier plane of a $4f$-stretcher.
The prism diffracts the beam, which causes a parallel shift of the exiting profile. In the case of the lens, the spatial shift depends also on the position at the Fourier plane. Thus, the spatial shift depends also on the frequency. The result is a spatial chirped pulse, because the output spectral components do not overlap ideally.

Adjustment tolerance of the cylindrical mirror in the final spatial light modulator setup

The dimensions of the cylindrical mirror are determined by the LC dimension. The LC has 640 pixel each is 0.1 mm wide, resulting in a total active width of 64 mm. That means the cylindrical mirror has to be at least 64 mm wide. Finally, a cylindrical mirror of 70 mm x 20 mm, which is curved along the 70 mm is used. The focal distance of the cylindrical mirror is defined by the grating and the desired transmitted bandwidth; the bandwidth should be same as the bandwidth of the grating compressor which was two times the FWHM, thus 60 nm. The grating, which is used in this setup, has a grating constant of 1800 lines per mm so the focal distance should be 500 mm (see section 1.3).
The planarity of the surface of the cylindric mirror is usually given by the deviation in units of fraction of the wavelength λ, of the mirrors is very important in case of coherent laser radiation, because deviation from the planarity causes interferences.
A quality with a deviation of $\lambda(550nm)/4$ per 10 mm from an ideal cylindrical shape means that the focal spot enlargement due to the slope error is

$$q = 2 \cdot \frac{\lambda}{4} \cdot \frac{f}{10mm} = 13.7\mu m \tag{96}$$

All mirrors in the SLM setup have to be precise, especially the folding mirror and the back-reflecting mirror, because imaging defaults of theses two mirrors caused

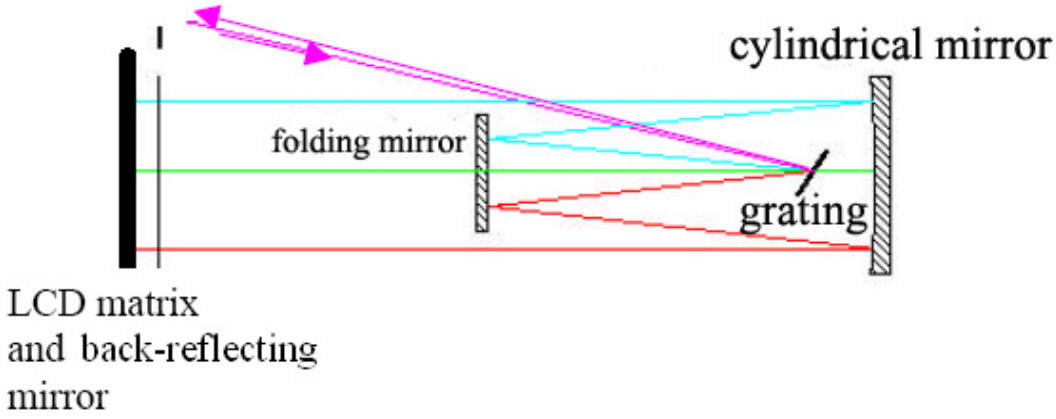

Figure 36: This setup of a 4f-stretcher avoids the angle of the folding mirror against the optical axis. This is a pure on-axis design with 0° of the folding mirror and the back-reflecting mirror. The back-reflecting mirror, which is placed directly behind the SLM saves space, a grating, and a mirror.

by the manufacturing can not be compensated by adjustment, the same applies for the cylindrical mirrors. It is more difficult for the manufacturing to achieve a planarity of the surface of $\lambda/10$ for cylindrical mirror than for flat mirror. Thus, a back-reflecting mirror with $\lambda/10$ and a cylindrical mirror with $\lambda/4$ accuracy are used. A last critical point is the position of the back-reflecting mirror behind the LC matrix. To achieve a propagation through the LC matrix with a flat wave front, the distance between the back-reflecting mirror and the LC matrix should be within the Rayleigh range (see equation 98). The spot-size of the laser beam should be smaller than the width of the pixel (100 µm). The initial laser beam spot of about $w_{in} = 3\,\text{mm}$ FWHM is focused to a small spot size of about $w_0 \approx 40\,\mu\text{m}$ at the SLM by the cylindrical mirror. For that a focal length of $f \approx 500\,\text{mm}$ is used. This can be calculated by

$$\omega_0 \approx \frac{\lambda f}{\pi w_{in}}. \tag{97}$$

Where f the focal length and ω_l/λ the incident beam parameter, c is the velocity of light, w_0 the final beam radius and w_{in} the initial beam radius, and a confocal range of 10 mm. Thus, the folding mirror should be about 3 mm behind the LC matrix. The Rayleigh length ρ_0 can be calculated using the $1/e$ radios of the focal spot w_0

$$\rho_0 = \frac{w_0^2 \omega_l}{2c} \tag{98}$$

At the end an ideal compact $4f$-stretcher is created.

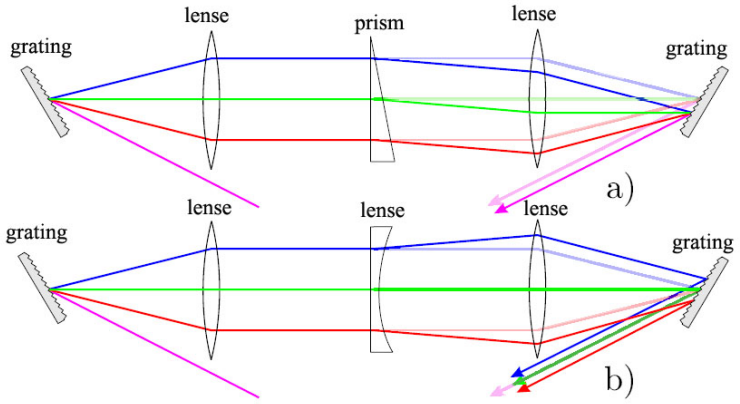

Figure 37: This figure illustrates the space-time coupling by regarding a linear (a) and a quadratic (b) phase-modulation. The linear modulation is realized by a prism and the quadratic by a planar-concave lens. The change of the propagation length is drafted. [10]

3.9 Limits of the Spatial Light Modulator

To compensate higher order dispersion, it is necessary to know the maximum phase-modulation, which can be realized by the SLM. The maximum phase-modulation is limited by the so called "Nyquist-limit". Furthermore the effect on the laser shaping due to the gap region between each pixel of the SLM has to be investigated The last important point concerning the limits of the SLM is the spatial dispersion introduced by the $4f$-stretcher setup.

Spatial dispersion caused by the $4f$-stretcher setup

The spatial dispersion is determined by the $4f$-stretcher geometry and has an influence on the Fourier plane.
It is possible to determine the location $x(\Omega)$ at the Fourier plane (see figure 38) for each frequency Ω, if the direction of refraction of the frequency ω_l is located along the optical axis ($x = 0$) and if the focal length f is given. Figure 38 shows a diagram of the relevant parameters. From this figure, one can calculate the location x as a function of Ω:

$$x(\Omega) = f \cdot arctan(\beta(\omega_l + \Omega) - \beta(\omega_l)) \tag{99}$$

The spatial dispersion is defined by

$$a(\Omega) = \frac{\partial x}{\partial \Omega} \tag{100}$$

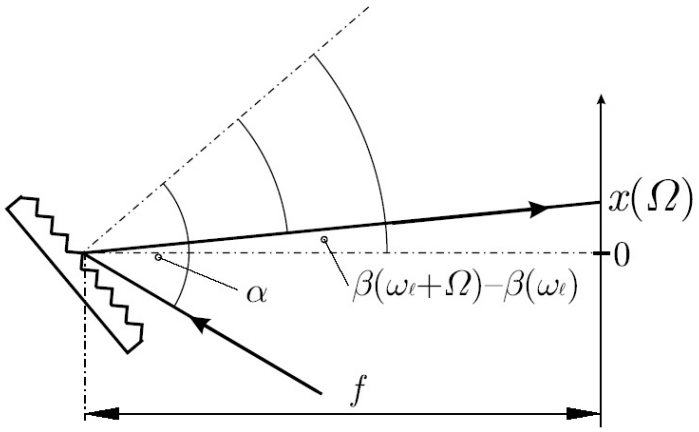

Figure 38: This figure shows an incident and an exiting beam diffracted by a grating. If the central frequency ω_l is diffracted along the optical axis ($x = 0$), it is possible to calculate the position x at the Fourier plane for every frequency ω. [10]

at the Fourier plane (location of the SLM), where it influences the pulse shaping by generating a linear chirp. Equation 100 can be written with equation 99:

$$a(\Omega) = \frac{-2\pi cf}{g \cdot (\omega_l + \Omega)^2\{1 + [\beta(\omega_l + \Omega) - \beta(\omega_l)]^2\} \cos\beta(\omega_l + \Omega)}. \tag{101}$$

with the grating-equation:

$$\beta(\lambda_l) = arcsin\left(\frac{\lambda_l}{g} - sin(\alpha)\right) \tag{102}$$

The equation shows that the spatial dispersion $a(\Omega)$ is a nonlinear function of Ω. For small bandwidth, the spatial image of the frequency can be linearized:

$$x(\Omega) = a(0) \cdot \Omega = \frac{-2\pi cf}{g\omega_l^2 \cos\beta(\omega_l)} \cdot \Omega. \tag{103}$$

The relation between the space and the frequency for the experimental setup is shown in figure 39. The spectral deviation of the linear approximation is already 10% at the borders of the SLM ($\pm 3.2\,\mathrm{cm}$). The consequences of this approximation can be shown. Regarding a linear spectral phase $\varphi(x) = \tau \cdot x/a(0)$, the pulse is then shifted by τ. The higher order derivation of the spectral phase clarifies the behaviour of the linear spectral phase.

$$\varphi(\Omega) \quad = \quad \varphi(x(\Omega)) = \tau \frac{1}{a(0)} x(\Omega) \tag{104}$$

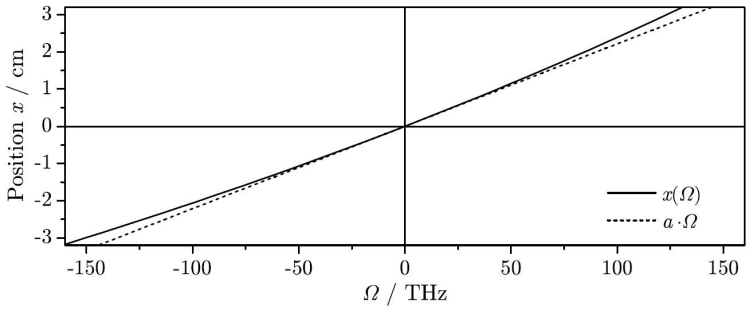

Figure 39: Position as a function of frequency $x(\Omega)$ at the Fourier plane of the experimental setup at a central wavelength of 804 nm. The linear approximation is represented by the gap-line [10].

$$\frac{\partial}{\partial\Omega}\varphi(\Omega) = \tau\frac{1}{a(0)}\frac{\partial}{\partial\Omega}x(\Omega) = \tau\frac{a(\Omega)}{a(0)} \tag{105}$$

$$\frac{\partial^2}{\partial\Omega^2}\varphi(\Omega) = \tau\frac{1}{a(0)}\frac{\partial^2}{\partial\Omega^2}x(\Omega) = \tau\frac{1}{a(0)}\frac{\partial}{\partial\Omega}a(\Omega) \tag{106}$$

These equations shows that only in the case of $\Omega = 0$ the phase rise is τ, but for other frequencies the slope varies. Also a linear chirp is a result of the frequency dependent temporal shift, which follows from the second derivation. This effect is important for the basic tests, which include exact phase modulation, because the exact position of the frequencies at the Fourier plane of the SLM setup has to be considered.

Pixel-Replica

An ideal SLM would have an active LC matrix without any gaps, but this is technically not yet possible. The phase at the gaps is not controllable and influenced by both neighboring pixels. They are responsible for a discrete phase modulation m_{gap}. r is in further calculations the relative width of the gaps in condition to the pixel-distance Δx. A discrete phase modulation excites just a cascaded image [10]

$$\begin{aligned} m_{pix} &= \sum_{l=-N/2}^{N/2} m(l\cdot\Delta x)\cdot rect\left(\tfrac{x-l\cdot\Delta x}{(l-r)\Delta x}\right) \\ &\quad + m_{gap}\cdot rect\left(\tfrac{x-(l+\frac{1}{2})\cdot\Delta x}{r\Delta x}\right) \end{aligned} \tag{107}$$

$$\begin{aligned} &= m(x)\cdot\sum_{l=-N/2}^{N/2}\delta(x-l\cdot\Delta x)\otimes rect\left(\tfrac{x}{(l-r)\Delta x}\right) \\ &\quad + m_{gap}\cdot\sum_{l=-N/2}^{N/2}\delta\left(x-(l+\tfrac{1}{2})\cdot\Delta x\right)\otimes rect\left(\tfrac{x}{r\Delta x}\right) \end{aligned} \tag{108}$$

with

$$rect(x) = \{^{1,|x|\leq 1/2}_{0,else.} \tag{109}$$

It follows for $x(\Omega) = a(0)\Omega$ and an infinite small focal length in the Fourier plane of the $4f$-stretcher [10]:

$$\Xi_{pix}(\Omega) \quad = m_{pix}(a\Omega) = \Xi(\Omega) \cdot \sum_{l=-N/2}^{N/2} \delta(\Omega - l \cdot \Delta x/a) \otimes rect\left(\frac{a\Omega}{(l-r)\Delta x}\right) \tag{110}$$

$$+m_{gap} \cdot \sum_{l=-N/2}^{N/2} \delta(\Omega - (l + \tfrac{1}{2}) \cdot \Delta x/a) \otimes rect\left(\frac{a\Omega}{r\Delta x}\right) \tag{111}$$

This equation includes the fact that the modulator has a discrete filter-function $\Xi(\Omega)$ (640 pixel). The response-function $\xi_{pix}(t)$ of the pulse-shaper can now be calculated by

$$\xi(t) = \frac{1}{2\pi} \int_{-\infty}^{\infty} \Xi(\Omega) e^{i\Omega t} d\Omega, \tag{112}$$

and the approximation that the spectral components are not cut off by the LC matrix, allows one to make the border crossing $N \to \infty$. Thus, the response-function of the SLM is:

$$\xi_{pix}(t) \quad = \sum_{l=-\infty}^{\infty} \xi(t - l \cdot \tfrac{\pi 2a}{\Delta x}) \cdot (1 - r) \cdot sinc\left(\frac{(1-r)\Delta x}{2a} t\right) \tag{113}$$

$$+M_{gap} \sum_{l=-\infty}^{\infty} (-1)^l \delta(t - l \cdot \tfrac{\pi 2a}{\Delta x}) \cdot r \cdot sinc\left(\frac{r\Delta x}{2a} t\right)$$

Figure 40 shows a simulation of a pulse before and behind the pulse shaper. There are three cases illustrated, an ideal filter and discrete filter and a filter with gaps, like the real pulse shaper. Every figure shows the influence of the resulting response-function.
Neglecting the influence by gaps ($r = 0$), the discrete electrode-structure of the LC matrix causes beside the modulated pulse, temporally equidistance replicas. The replicas have a distance of $\pi 2a/\Delta x$ (see figure 40) and they are damped proportionally to a sinc-envelope, with zero-crossings at multiples of $\pi 2a/\Delta x$. The second case (b) in figure 40 shows a constant phase modulation $\xi(t) = e^{i\phi_0}\delta(t)$, there are no pixel-replicas because the initial pulse remains and the zero-crossings collapsed with the sinc-envelop. The third case (figure 40 (c)) includes also the gaps with $r > 0$, which generate a constant modulation. The gaps effect temporally equidistant copies of the unmodulated initial pulse. These are less damped than the pixel-replicas and gaps cause a shift of the sinc-envelope. Thus, they are never at the same position as the pixel-replicas. But there is a case in which the discrete filter-function disappears. It has to be $\xi(t) = \Xi_{gap}\delta(t)$, where $\Xi_{gap}\delta(t)$ is the constant gap modulation. So each pixel has the same modulation as the gaps. The first zero-crossings of the *sinc*- envelope of the modulated

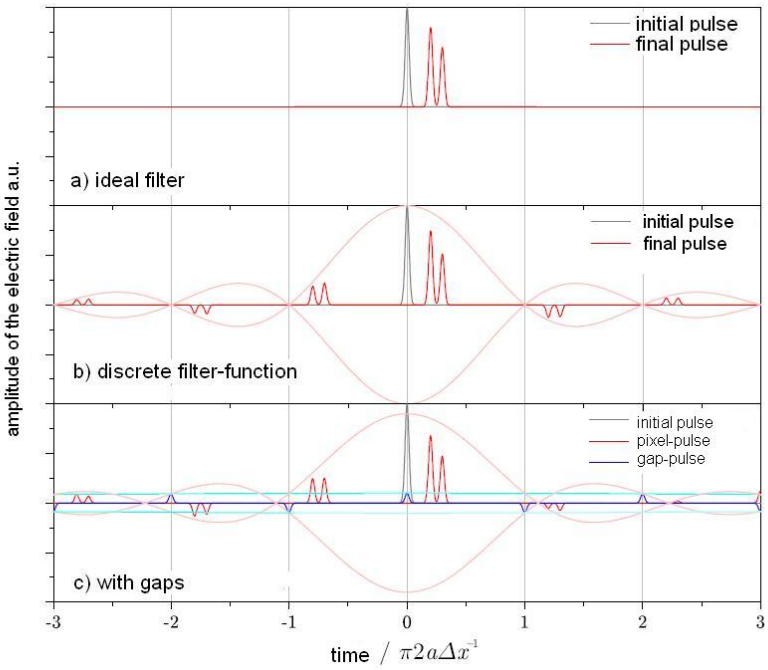

Figure 40: The simulation shows the influence of a discrete filter-function and a discrete filter-function with gaps. The discrete filter-function $\Xi(\Omega)$ generates replicas of the modulated pulse (b). The replicas have a distance of $\pi 2a/\Delta x$. Additional replicas of the initial pulse are caused by the gaps between the pixel (c) [10].

pulse lie at $\approx \pi 2a/\Delta x$. The usable time frame is the half of it, because a time independent modulation is just given for the case of non-overlap of the initial pulse and its copies. The rise of the phase is limited; this is calculated by the Nyquist limit.

Nyquist limit

The pulse modulation is limited by the discrete phase function given by the so called "Nyquist sampling theorem", which is also called aliasing in the theory of discrete Fourier-transformation. Every function of modulation is discretized over the 640 modulator-pixels.
The sampling theorem says that every periodic function has to be displayed at least by two bases per period to realize uniqueness.
The sampling frequency ν_{samp} defines the limit frequency called the Nyquist-frequency ν_{Ny}

$$\nu_{Ny} = \frac{\nu_{Samp}}{2}. \tag{114}$$

Two bases per period means at least two over a period of 2π, because the modulo 2π property of the phase allows differing between rise or fall by π.
Thus, the phase-function of the pulse shaper has to be in such a way that a phase-shift of $\Delta\phi = 2\pi$ extends over two pixel. The phase difference between two neighboring pixels $\delta\phi$ may not exceed π:

$$\delta\varphi = \mid \phi(\Omega + \Delta\Omega) \mid < \pi, \tag{115}$$

where $\Delta\Omega = \Delta x/a$ is the frequency distance between neighboring pixels. Consequently, it is just possible to realize phase-functions with a slope of $\frac{d\varphi}{d\omega} < \pi$.
The maximum values for the available compensation of higher-order dispersion can be calculated with the formula for the Taylor coefficient from equation 27:

$$\begin{array}{rcl} |\phi_1| < \frac{\pi}{\Delta\Omega} & \Rightarrow & |\phi_1|_{max} = 12.5 \cdot 10^3\,\mathrm{fs} \\ |\phi_2| < \frac{2\pi}{N^2\Delta\Omega^2} & \Rightarrow & |\phi_2|_{max} = 1.6 \cdot 10^5\,\mathrm{fs}^2 \\ |\phi_3| < \frac{8\pi}{N^2\Delta\Omega^3} & \Rightarrow & |\phi_3|_{max} = 3.9 \cdot 10^6\,\mathrm{fs}^3 \\ |\phi_4| < \frac{48\pi}{N^3\Delta\Omega^4} & \Rightarrow & |\phi_4|_{max} = 2 \cdot 10^8\,\mathrm{fs}^4 \end{array}$$

$\Delta\Omega$ is calculated by $\Delta\Omega = \Delta x/a(0)$ with $\Delta x = 100\,\mu\mathrm{m}$ and $\alpha - \beta(\omega) = 15°$. N is the number of pixels ($N = 640$). The values are for the case that all coefficient $\varphi_{k\neq l}$ disappear. In the practical case where one uses a combination of Taylor coefficients of different orders, the achievable values are a less than the calculated values above.

Wrap-Replica

Another limitation results by considering the "elbowroom" of the LC molecules. The molecules can not move independently from each other, so that especially the gap-molecules orientation is influenced by the pixel molecules. The result is a continuous crossover of the molecules from one pixel to the following pixel. That means the modulation, caused by the gaps, is not constant, which prevent the gap-replica and the pixel-replica are reduced.

The effect arises, if one wants to realize phase-shift higher than 2π. The SLM-S 640/12 has a maximum phase-shift of about 5π, but the usable range is just 2π. To generate higher modulation the spectral phase has to be wrapped modulo 2π. Wrapping requires an infinite steepness rising at the wrapping position. This means that the molecules orientation has to change without spatial extension and that's not the case.
The interaction of the molecules entails a finite increase of the 2π jump. As an example, a linear phase modulation clarifies this problem. Figure 41 shows such a modulation in the unwrapped and wrapped case. It shows that the periodic phase modulation generates a temporal time shift, but beside this, it also creates replica in the distance of the temporal time shift. These replicas are

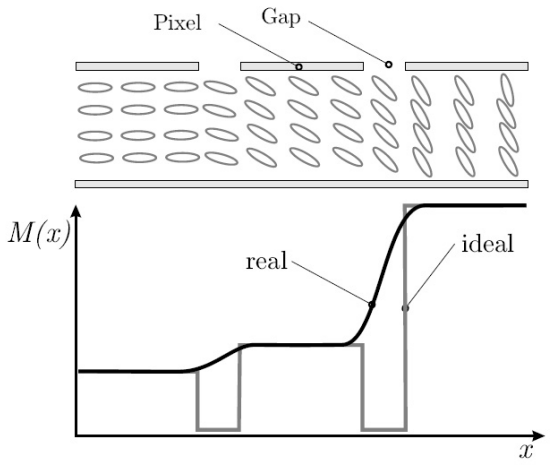

Figure 41: The molecules of the liquid crystal, which are located in the gaps between the pixel-molecules, are influenced by the neighboring molecules. That means that the molecules of the liquid crystal are not orientated discretely. This causes a smoothing of the discrete modulation [10].

called wrap-replicas. There are just a few properties to mention, the first one is that an increasing slope of the 2π jumps causes a decreasing of the intensity of the wrap-replica. Therefore it is advantageous to have a small beam waist at the focus of the cylindrical mirror to not rise the phase smoothing by the molecule coupling. Another property is the temporal wide distribution of the wrap-replica, in case of any phase modulation, where the 2π jumps are spectral unequal. This causes differences in the ideal periodic modulation.

3.10 Adaptive Dispersion Compensation

The main task of the SLM is the compensation of the residual dispersion after the fiber and the grating compressor.
To compensate dispersion, it is necessary to calculate the exact dispersion of the laser pulse, which should be modulated by the SLM to adjust the correct voltage to the pixel of the SLM.
For that, the position of the spectrum on the LC matrix has to be well known. All these circumstances have to be kept in mind, while calculating the necessary phase-shift of each pixel.
One can avoid the calculation by using a non-deterministic algorithm.
The algorithm should be based on a global search-strategy to find a qualitative solution in great search vacate and the algorithm should be able to converge under experimental conditions. One algorithm fulfilling these demands is the

genetic algorithm. The algorithm tries to sample every local minimum, starting from a plurality of start-points.

Genetic Algorithm

The genetic algorithm (GA) is a procedure, which is non-deterministic optimization. The concept of these algorithms is the biological theory of evolution. The main operations are the mutation, cross-over and survival of the fittest.
The genetic algorithm has been developed by John Holland in the USA in the seventies [36].
The biological theory of evolution describes the evolution of life forms. These life forms are optimally adapted to their natural environment. Survival of the fittest means thereby that those individuals of a population survive, which are adapted best to a specific habitat. Its genotype is changed by mutation and cross-over, before the genotype is handed over to the next generation. This process repeats itself again and again. The result is an adaptive system present over many generations, which can also survive small changes of the environment.
The genetic algorithm is based on the following process:
The algorithm starts with an initial population of individuals, whose genotype consists of random numbers. One individual is a set of parameters of optimization.
The initial population is the primary generation. The primary generation provides a creation of descendants. These descendants are created by mutation or by crossing of pairs of individuals. The result of this process is a generation. Now, the new generation has to be evaluated. This is done by taking the parameters (gene) of each individual and insert them into the function, which has to be minimized.
Thus, a fitness value is assigned to each individual. This fitness is an indicator for the evaluation of the certain proposal for the solution. The selection of the best individuals is the next step. The best individuals are filtered to become "parents" for the next generation of "children". In this manner, the descendants are generated iteratively, thus getting better and better. This concept of population uses a high number of proposals for solution and takes them into the next round of the genetic algorithm.
The method allows reacting flexible to slow changes of the desired function, but also sudden short jumps. In the special case of the genetic algorithm, the parameters of optimization are coded binary. The first step of the genetic algorithm is to evaluate the individuals of the initial population. Capable individuals from the first generation are chosen to generate new descendants by a recombination pattern. This marriage pattern can be described as follows:
The first step is to establish a ranking list by evaluating the individuals. Afterwards, two individuals are chosen with a probability, which is proportional to the

evaluation. The search strategy is determined by the cross-over (recombination-pattern). There are several possibilities of cross-over. Descendants are generated by cutting the sequences of the two binary sequences of the parents at different positions. The fractions are then alternately folded. For mutation, the bits of the binary coded genotype of the descendants are folded at random positions. The chance of this bit-inverting depends on the recombination-pattern. Thus, a new genotype is inserted into the population by mutation.
Without the mutation, the population becomes more and more homogeneously, because of the selection. As a consequence there is the possibility to converge in a local minimum and not in a global minimum. In the end the individuals of the old generation are replaced by descendants.
The replacement pattern is very manifold and they have to be adapted to the concrete problem. The replacement pattern can replace the whole generation, or it is elitist. In this case the n best individuals are taken over in mutated form into the next generation.
The GA is used for dispersion compensation, the individuals and population have to be adapted to the concrete problem of this work.

3.11 Experimental method for the self-learning feedback optimization

In this work, the voltage across the pixels is stored individually, so that every individual has 640 elements (gene) one for each pixel. The initial voltages for the pixel, which is up to a phase-shift and the initial population of individuals are generated at random. The number of individuals for a population must be alleged and are responsible for the rate and the efficiency of the genetic algorithm.
Figure 42 shows the GA which is adapted to the TEO experiment: The algorithm starts with a certain number of individuals, in this case there are 25 individuals. Each individual contains 640 variables and each variable presents a pixel. The value of each variable is determined randomly and is up to a phase-shift of 2π. The feedback signal for the assessment is a photomultiplier signal of a frequency doubled laser pulse where the intensity is inversely-proportional to the pulse duration. After the assessment, the variables of the population are selected using the principle of its survival of the fittest. Afterwards, the variables are recombined and completed by random variables to form a new individual. The next population is then established by the elitism-rule and randomly generated individuals. The genetic algorithm has no global maximum, but it converges to saturation.
To evaluate the population, the laser beam is frequency doubled in a BBO crystal, after passing the SLM. Since the energy of the laser pulses is constant the

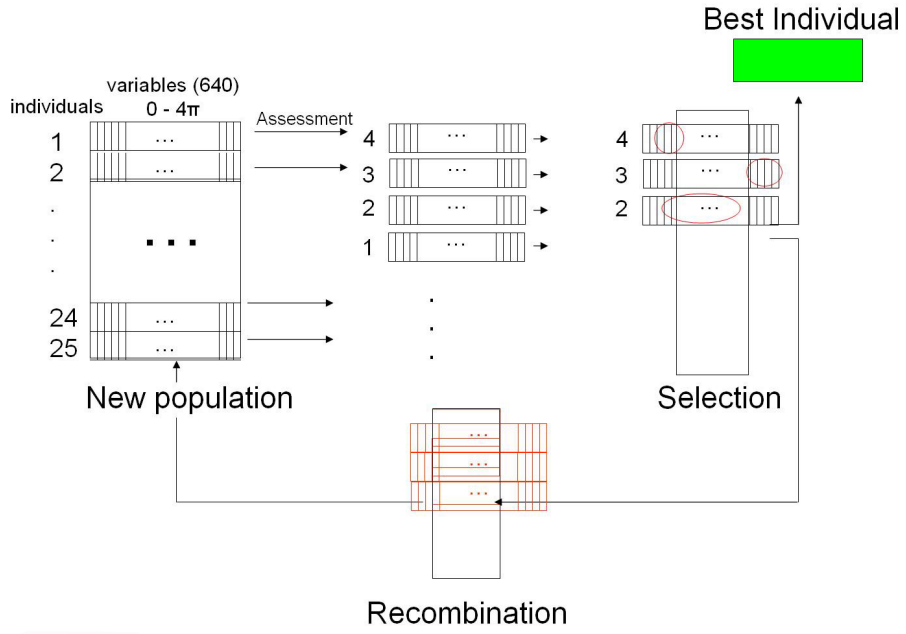

Figure 42: The principle of the genetic algorithm.

BBO signal is increased when the pulse duration is decreased

$$I_{SHG} \propto I_{Laser}^2 \propto \left(\frac{Energy_{Laser}}{pulseduration} \right)^2 \cdot 1/area. \tag{116}$$

So the photon intensity of the second harmonic generations is used as a feedback for the genetic algorithm. The feedback signal is delivered by a photomultiplier behind the BBO. The aim is to minimize the pulse duration by maximizing the SHG signal.
The fitness factor is the SHG signal. Based on this signal, a set of individuals is selected and is used, as described in the section before, for the next generation. This process is repeated until the algorithm runs into saturation. The whole setup for GA algorithm is shown in figure 43. Before the genetic algorithm can be used to compensate dispersion, it is necessary to simulate the algorithm to insure that tit is feasible to compensate the dispersion by controlling the SLM.

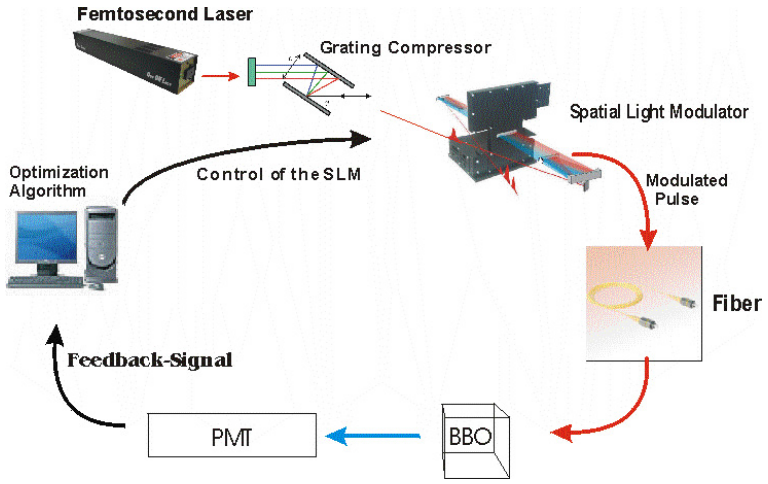

Figure 43: Scheme of an iterative algorithm: The laser pulse propagates through a grating compressor, a SLM and a fiber. The entire system is dispersion free. The feedback signal is generated in a BBO crystal and detected by a photomultiplier (PMT) which is installed behind the BBO crystal. This feedback signal is sent to a genetic algorithm.

4 Simulations, Measurements and Analysis

4.1 Simulation of the Self-Phase Modulation

The self-phase modulation (SPM) introduced in section 3.1 is a nonlinear effect that change the spectrum of the laser pulse. The nonlinear effect can be avoided by using a glass rod with a diameter larger than the fiber behind the fiber. The glass rod provides remaining dispersion for the final compression of the laser pulse (see section 3.1). But, the spatial intensity of the laser is drastically reduced due to the much larger transverse laser diameter compared to the core of the fiber (see equation 116).

Therefore, no SPM accrues even though the laser pulse reaches its shortest pulse duration. Figure 44 and figure 45 show simulation results. Figure 44 shows the simulated spectrum of the laser pulse with high intensity which has propagated through a 170 m long quarz glass fiber. The spectrum is entirely distorted and significantly different from the initial spectrum one (red line in figure 44). The result of a reduction of the intensity in the simulation by a factor of 100 is shown in figure 45. The spectrum has modulation, but it is similar to the initial spectrum.

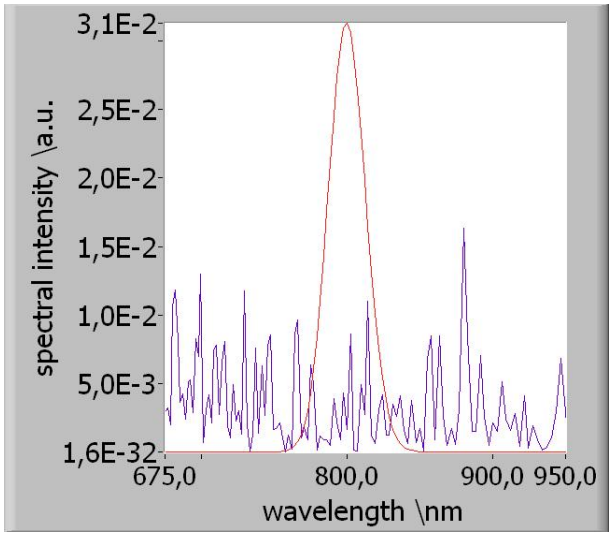

Figure 44: The Lab2 simulation shows the spectrum of self-phase modulated Gaussian for a propagation lengths of 170 m in quarz glass fiber. The blue line is the spectrum behind the dispersive element, the red one shows the initial pulse spectrum.

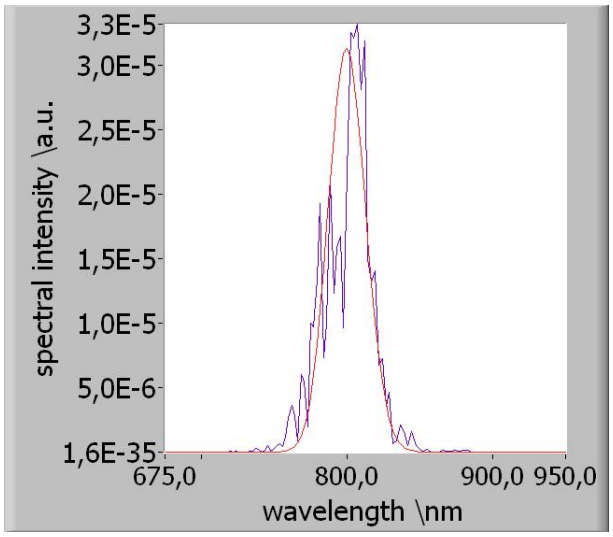

Figure 45: The Lab2 diagram shows the spectrum of a laser pulse which has propagated along a 170 m long quarz glass fiber with 100 times lower intensity than in figure 44. The blue line is the spectrum behind the dispersive element, the red line shows the initial pulse spectrum.

4.2 Calculation of the FWHM after the fiber

The dispersion in an optical fiber can be calculated by equation 53. The factor k'' represents the GVD and is a material constant, which depends as follows on the wavelength:

$$k_l'' = \frac{\lambda_l^3}{2\pi c^2} \frac{d^2 n}{d\lambda_l^2}|_{\lambda_l} \tag{117}$$

The value for $\frac{d^2 n}{d\lambda^2}$ for SQ1 is tabulated in reference [18] with $0.4 \cdot 10^{11} \frac{1}{m^2}$. So, the pulse duration $\Delta\tau$ increases with

$$\Delta\tau = \frac{2\pi c}{\lambda_l^2} \cdot k_l'' \cdot l\Delta\lambda \tag{118}$$

For a fiber length l of 170 m, the resulting pulse duration $\Delta\tau$ is 540 ps, a spectral width of $\Delta\lambda = 30$ nm, at a central wavelength λ_l of 800 nm.

4.3 Analysis of the polarization maintenance of the Thorlabs fiber FS-LS-4616

The fiber which is used in this work is a single-mode polarization maintenance fiber, with a mode field diameter of $(5.3 \pm 0.5)\,\mu m$. The core is surrounded by a $(80 \pm 2)\,\mu m$ diameter cladding. The operation wavelength is 820 nm with a cut-off wavelength of less than 780 nm. The typical attenuation is 3.0 dB/km and the maximum attenuation is 5.0 dB/km (see section 2.6).
The factor to test is the h parameter, which defines how well the polarization is preserved. The h-parameter should be less than $5 \cdot 10^{-4}/m$, measured at the operating wavelength of 820 nm. This value is given by the manufactory and means that the polarization is preserved with a accuracy of $5 \cdot 10^{-4}$ for each meter of the fiber.

Analysis of polarization maintaining of the fiber

To verify the maintenance of polarization in the fiber, two half-wave plates, the fiber, a polarizer and two photodiodes are needed. The setup is shown in figure 46.

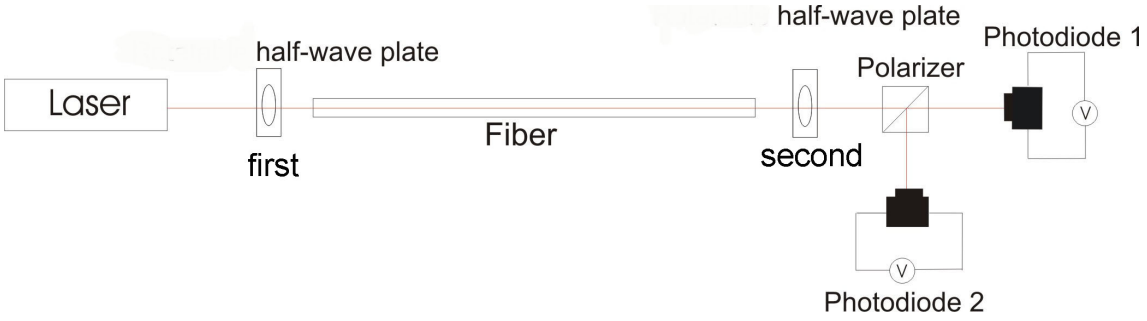

Figure 46: Setup for the polarization maintenance measurement.

The measurement starts with an angle of 0° of the first half-wave plate. The angle of the second half-wave plate is varied between 0° and 90°. The intensity after the polarizer is measured for every angle by the two photodiodes, the first photodiode is used to get the following data set to be analyzed, the second photodiode is used to get information about the noise and the signal of the second photodiode should increase by decreasing signal of the first photodiode. The comparison allows to define the polarization, high differences between the two photodiode signals means a linear polarized laser pulse. This measurement will be repeated for angels from 0° to 45° in steps of 5° of the first half-wave plate. The measured intensities at the photodiodes should follow a $\cos^2(x)$ function in case of polarization maintaining, which follows from the law of Malus [17]. Therefore

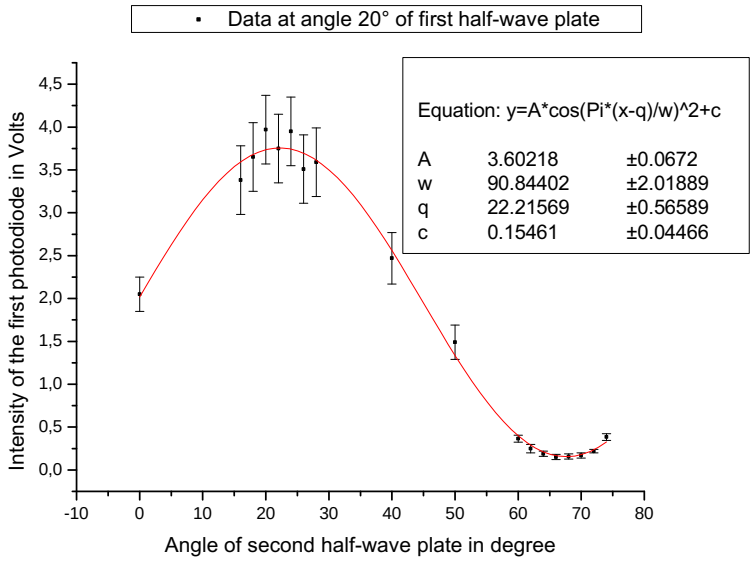

Figure 47: Measured value and fitted curve for analyzing the polarization maintenance

every measurement has been plotted and fitted by

$$Y = A \cdot \cos^2\left(\frac{\pi(x-q)}{\omega}\right) + c \tag{119}$$

c is a constant, q the shift of the $\cos^2(x)$ curve, A is the amplitude and ω the frequency of the $\cos^2(x)$ curve. Several results are plotted in figures 47 and 48. The maximum values and the minimum of every data set are plotted as a function of the angle of the half-wave plate before the fiber (see figure 49). They are also fitted by equation 119, because the maximum values as well as the minimum values follow also the law of Malus.
Figure 49 shows the ratio of the quotient of the maximum and the minimum value. This ratio is the h parameter times the fiber length of l =170 m.

The fiber shows a value of $l \cdot h = 0.020 \pm 0.008$ which means in case of the 170 m long fiber a h parameter of $(1.2 \pm 0.5) \cdot 10^{-4}$/m. Concluding, only 2 % of the initially fully polarized beam have been scattered while propagating in the fiber into the perpendicular polarization. The h parameter which is given by Thorlabs is $5 \cdot 10^{-4}$ /m. Thus, the fiber maintains the polarization even better than it was specified by the manufactory.

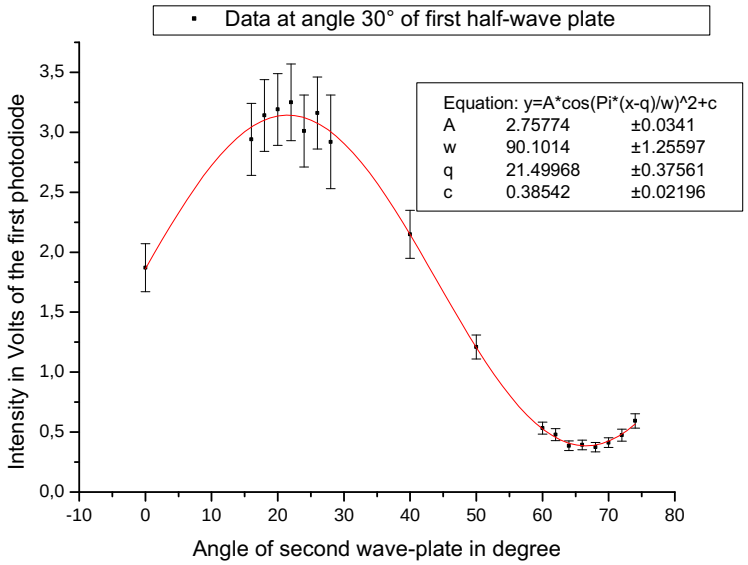

Figure 48: Measured value and fitted curve for analyzing the polarization maintenance

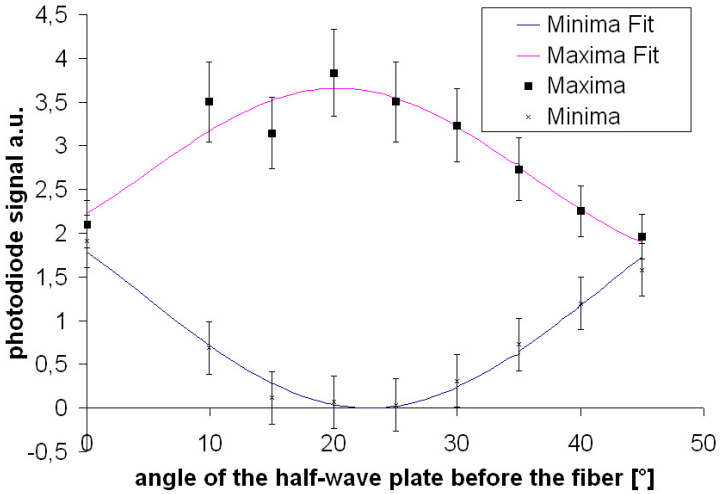

Figure 49: The diagram shows the maxima and minima of the fitted curves. The values for the maxima are fitted with equation 119, the same was done with the minima.

4.4 Calibration of the phase-shift as a function of the applied voltage to the Spatial Light Modulator

To be able to control the SLM, it is necessary to measure the phase-change of the SLM as a function of the voltage, which is impressed to a pixel of the LC matrix. To determine the phase-shift $\phi(U)$ the phase-modulation has to be transformed into an amplitude-modulation, which can be measured by a photodiode or photomultiplier. The transformation can be achieved by a 45° polarizer in front of the LC matrix (see figure 50).
The laser light passing the polarizer is tilted by 45° with respect to the optical axis. This light can be separated into two orthogonal waves, in x and y direction, with equal amplitude. Since the LC matrix is birefringent, difference in the propagation velocity of the two waves, cause a relative phase-shift $\Delta\phi$. After the LC matrix for an arbitrary phase-shift $\Delta\phi$ the laser light is an elliptical polarized wave. The phase-shift or phase-retardation is given by

$$\Delta\phi = \frac{2\pi}{\lambda} d\Delta n. \tag{120}$$

For the SLM, which has a voltage dependent index of refraction and a thickness of z_{LC} follows:

$$\Delta\phi_0 = \frac{2\pi}{\lambda} z_{LC}\Delta n(U). \tag{121}$$

After passing the LC matrix, the beam is reflected and passes the LC matrix a second time. This is considered by a doubling of the LC thickness:

$$\Delta\phi = \frac{2\pi}{\lambda} 2 \cdot z_{LC}\Delta n(U). \tag{122}$$

The last element for the laser beam to pass, is the polarizer again. The whole setup is shown in figure 50.

This setup can be seen as a polarizer-analyzer pair which includes a birefringent medium and where the polarizer and the analyzer are parallel to each other. The transmission can now be calculated by using Jones-matrix [17]. The transmission is then given by:

$$T(U) = \cos^2\left(\frac{\phi}{2}\right). \tag{123}$$

The measurement allows calibrating the phase-shift as a function of the impressed voltage on the pixels of the SLM. The maximum value for the impressed voltage is U_{max} =10 V. The voltage can be controlled with a resolution of 12 bit, or resulting in an increment of 2.44 mV and 4096 control values for the voltage.
For a given wavelength and the thickness of the LC cell, it also possible to calculate the difference of the index of refraction $\Delta n(\omega, U)$.

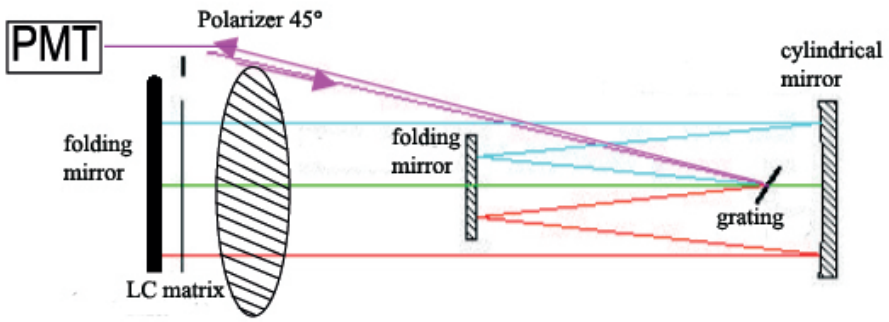

Figure 50: The SLM setup has to be upgraded by a polarizer. This polarizer is placed in front of the SLM to transform the phase-modulation into an amplitude-modulation. The amplitude is detected by a photomultiplier (PMT).

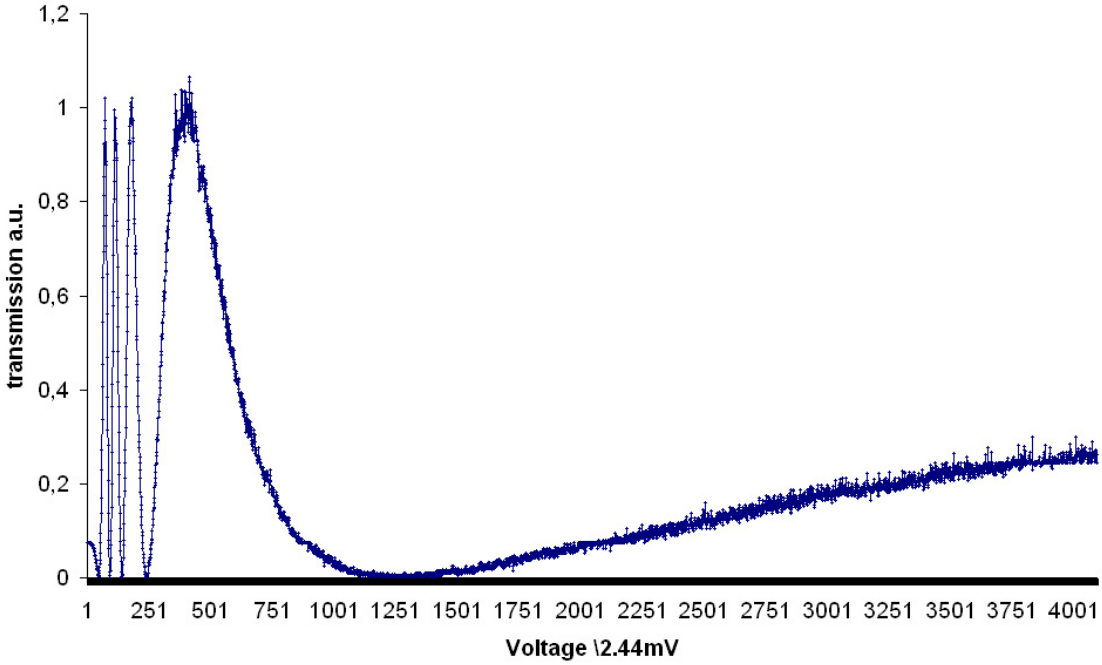

Figure 51: The transmission of the SLM as a function of the voltage is measured to calibrate the SLM.

Figure 51 shows the transmission as a function of the voltage. This curve is

transformed with the equation:

$$\phi = 2 \cdot arccos\left(\sqrt{T(U)}\right) \tag{124}$$

The transformed curve in figure 52 has a folded structure. This is a result of the

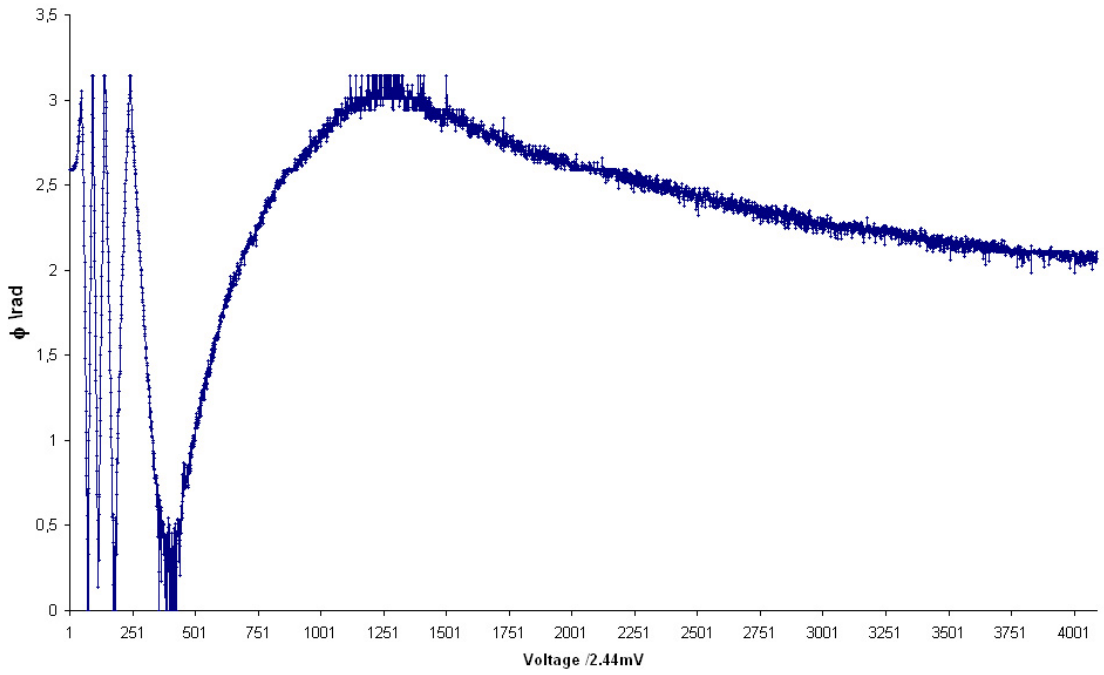

Figure 52: The diagram shows the transformed curve of the transmission curve.

square root and *cos*-function, which are not unique. To understand the oscillating behaviour with an exponentially decreasing frequency one has to take physical arguments into account. These arguments also allows to unfold the curve:
The nematic liquid crystals have the property to be completely birefringent, if the impressed voltage is zero and they become less birefringent by increasing voltage. Therefore, the calibration curve has to decrease with increasing voltage. It is not clear, if the curve is decreasing or not because of $\cos(x) = \cos(-x)$.
The next equivocality is based on the periodic structure of the *cos*-function, because it is $\cos(x) = \cos(x + 2\pi)$. Thus, the calibration curve can be shifted by $n \cdot 2\pi$ up and down. But the phase-retardation decreases monotonously by increasing voltage, so that in the case of maximum voltage the phase-retardation tends to zero. The calibration curve of the phase-retardation could be established by (see figure 53) taking this into account.

The calibration curve (figure 53) shows a maximum phase-retardation of nearly 8π with an offset of π in agreement to the specification of the manufacturer of

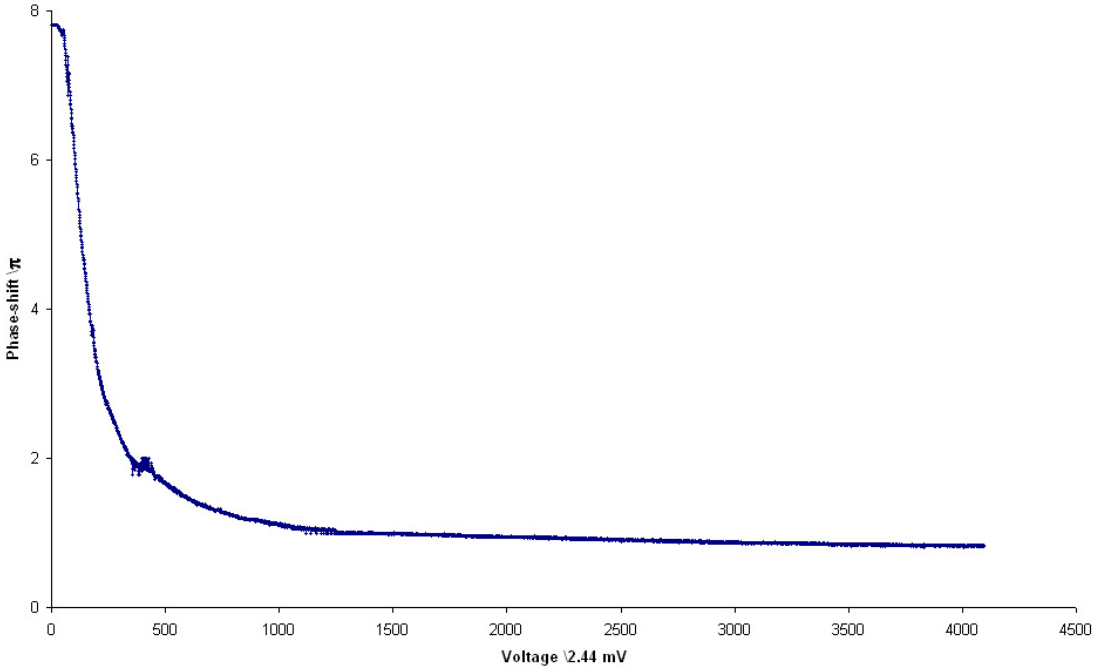

Figure 53: The calibration curve extracted from the measurement in figure 52. The calibration curve allows determining the working area and the maximum phase-shift.

4π for a single passage through the SLM. The calibration curve allows to select the region for the SLM control system. The intermediary range provides high dynamics for the phase-retardation with a sufficient fine control.
If the voltage is too high, the induced electric field will have a noticeable influence on the gaps, which will cause a deviation of the fixed filter-function of the gaps. If the voltage is too low, the time of response of the LC matrix will be too long. Now, it is possible to control the SLM matrix and to induce a certain phase-retardation by a well defined control-voltage. But the SLM works properly in a well calibrated SLM setup. The calibration of the setup is the next step.

4.5 Calibration of the Spatial Light Modulator Setup

For a properly working shaper, the setup should be free of dispersion that means the exiting laser pulse should deliver the same spectra and auto-correlation signal as the initial beam. The parameter of the setup are summarized in table 9.

I have done the first calibration with the auto-correlation method. Therefore the auto-correlation signal of the initial beam is taken, to compare it with the signal, which results after the laser has passed the SLM setup. The two signals

grating	$1800\,\mathrm{mm}^{-1}$
$\alpha - \beta_l$	$15°$
focal length	50 cm
number of pixel	640
pixel distance	100 µm
distance gap/pixel	0.04 µm
thickness of the modulator	3 mm
beam diameter	50 µm
transmission	47% at 800 nm
response time	$\approx 40\,\mathrm{ms}$
bandwidth	60 nm

Table 9: Parameters for the SLM setup at a central wavelength of 800 nm

are represented in figure 54 and 55.

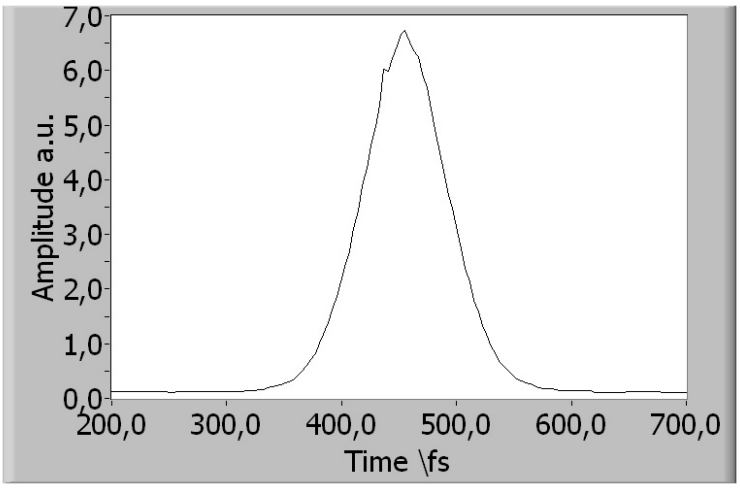

Figure 54: The figure shows the auto-correlation signal of the pure laser without grating compressor and SLM setup. The autocorrelated FWHM is 82fs.

The comparison of two auto-correlation signals shows that the FWHM of the two signals matches very well. The difference of 19 fs between the two signals is caused by a linear chirp. Thus, the SLM setup is not completely dispersion free and the alignment can be optimized. But the exiting signal behind the SLM has a "tail". This "tail" depends partly on the intrinsic phase. The intrinsic phase [10] follows from the image deviation of the real setup. These deviations are normally aberrations of the optical elements used. The aberrations increase with increasing angle of the light with respect to the optical axis and therefore

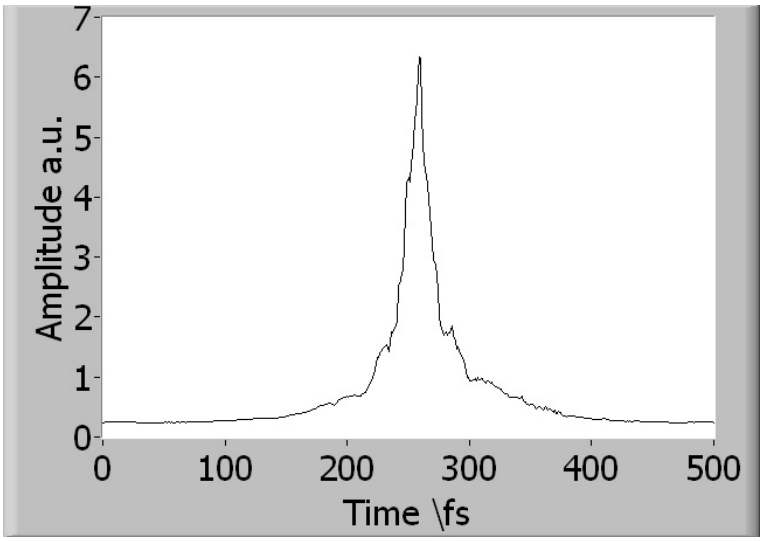

Figure 55: The figure shows the auto-correlation measurement of the laser after passing the SLM setup without any applied pattern. The autocorrelated FWHM is 63 fs.

especially the borders of the spectrum are involved in these deviations. Another reason for the "tail" can be a not optimally adjusted SLM setup and the not perfect optical surfaces of the components of the SLM setup. Regarding the proportions of the tail, the main reason for the tail are misalignments.
The "tail" will be compensated by the optimization algorithm, which will be used to control the SLM (see section 3.11).
Another way to check the setup is to analyse the spectrum of the laser beam before and behind the SLM setup. With the spectrum, one can detect for example a cut-off of the wavelength spectrum or one can detect modulation, which appears in peaks and asymmetrical spectrum. Also spatial chirps can be detected with a spectrometer.
The data, shown in figure 56, present the spectrum of the laser pulse before and behind the SLM setup. The initial spectrum (pink curve) is comparable with the final spectrum (red curve). Only for wavelength above 820 nm a cut by the size of the SLM is generated. The spikes are produced by the fiber-coupling of the spectrometer and do not belong to the laser beam spectrum, because the fiber-coupling consits of a multi-mode fiber and is not optimized for laser with a central wavelength of 800 nm.

To assure the correct functionality of the SLM and its setup, it is necessary to perform basic tests with the SLM. For instance certain pulse forms are generated by writing phase-sift patterns into the SLM. A pattern consists of 640 values. Each value belongs to a certain pixel and contains the control voltage for the pixel to introduce a phase-shift to the laser pulse. This can be done with a

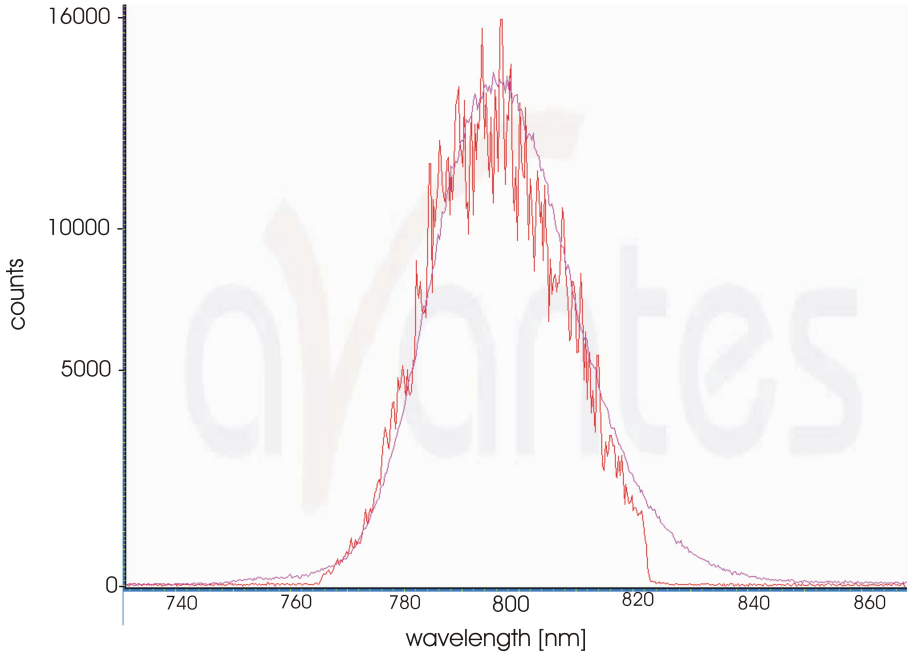

Figure 56: The figure shows two spectra of the laser beam, before (pink line) and after the SLM setup (red line). The cut-off of the red line is a result of the limited modulation window of the SLM. The spikes are produced by the fiber-coupling of the spectrometer and does not belong to the laser beam spectrum.

LabView program controlling the SLM.
The modulated pulse form will be measured by an auto-correlator. The expected results can be simulated by a Lab2 program.

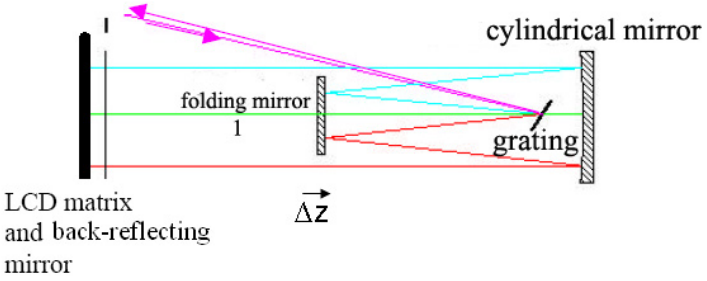

Figure 57: Setup to analyse the dependence of the FWHM on the position of the first folding mirror.

4.6 Alignment of the SLM

Before the SLM can be tested with discrete phase functions the sensibility of the positions of the folding mirror (see figure 57) has to be analysed by a variation the z-position to avoid misalignments. The FWHM of the final laser pulse as function of the z-position is shown in figure 58. This measurement should deliver information about the influence of the adjustment to the pulse form of the exiting pulse.

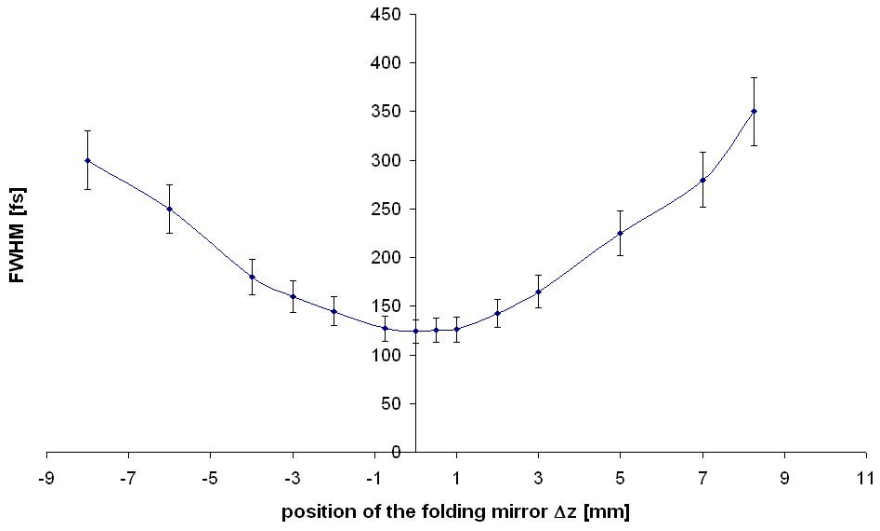

Figure 58: The plot shows that the position of the first folding mirror has a sensible influence on the FWHM of the exiting pulse.

The diagram shows that the position of the folding mirror has a significant influence on the pulse duration of the propagating laser beam. And the position

has to be chosen precisely to the position of the minimum of the pulse duration.

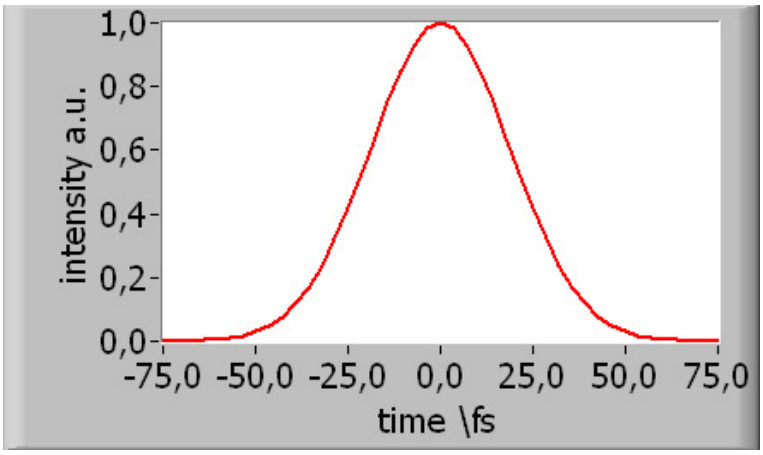

Figure 59: This diagram shows the simulated auto-correlation signal in case of a constant phase-shift pattern. The auto-correlation signal before and after the SLM setup is in the simulation exactly the same. Thus, this diagram represents booth signal, before and after the SLM setup.

4.7 Basic tests with discrete phase-functions

The calibration and the alignment of the SLM setup can be tested by modulating the laser pulse with discrete phase-function. The phase-function assigns to every pixel a certain value. For example a linear phase-function would assign to each pixel a phase-shift which increases linearly from one pixel to the other. This can be done by using the calibration-curve (see section 4.4), which allows generating a certain phase-shift at the pixel by impressing a control voltage on the pixel. The modulation will be analyzed by an auto-correlator. To verify the correct operation of the SLM the system will be compared to an auto-correlation trace, which is simulated with Lab2.
Beyond, the effect of the phase-modulation on the pulse form will be treated analytically.

Linear phase modulation

An auto-correlation signal of the laser beam (Figure 54) has been taken without the SLM setup to compare it with modulated laser pulses.
The simplest phase-shift pattern is a constant or zero pattern. The phase-shift, which follows from the impressed voltage, has to be calculated by using the calibration curve.
The auto-correlation signal behind the SLM setup should be the same as the signal of the initial laser (see section 2.2), because the SLM introduces over the whole bandwidth of the pulse the same phase-retardation.

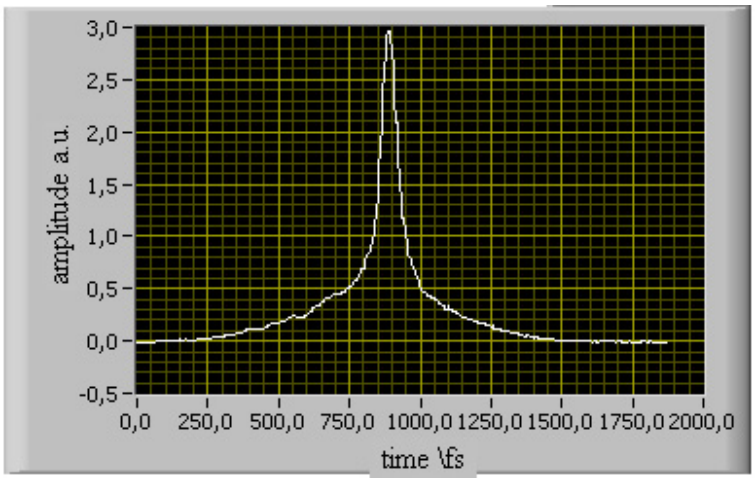

Figure 60: This diagram shows the measured auto-correlation curve in the case of a constant pattern for the SLM control.

The next step is the simulation of a constant pattern. The simulation includes a Gaussian laser pulse which passes the SLM, which phase-shift of each pixel can be controlled separately, and intensity detectors. The result of the simulation is presented in figure 59. The figure shows the auto-correlation signal. The pattern which is impressed upon the SLM is constant, with a constant value between 0π and 2π. The result is that a constant pattern has just slight influence on the pulse profile and the FWHM is the same within errorbors.

The measurement shows that the pulse profile after the SLM has just one main peak, but the auto-correlation signal shows a large tail. This "tail" has already been discussed in section 4.5.

Another linear phase modulation can be realized by a saw tooth pattern (see figure 62). A saw tooth pattern is a linear pattern, which has modulo breaks at the maximal applicable phase-shift value.

A linear phase-shift means that the modulated pulse is shifted in time. This behaviour can not be measured by an auto-correlation, because the auto-correlation has to be the same with and without a sawtooth pattern. This is proved by figure 61 which is similar to figure 55. But the time-shift can be simulated, which is shown in figure 63. The simulation also shows that if the modulo break of the pattern proceeds at even multiples of π, the modulated pulse is just shifted in time. But if the modulo break of the pattern proceeds at odd multiple of π, the modulated pulse is shifted in time and there are several small pulses beside the main pulse (see figure 64). The small pulses are replica pulses (see

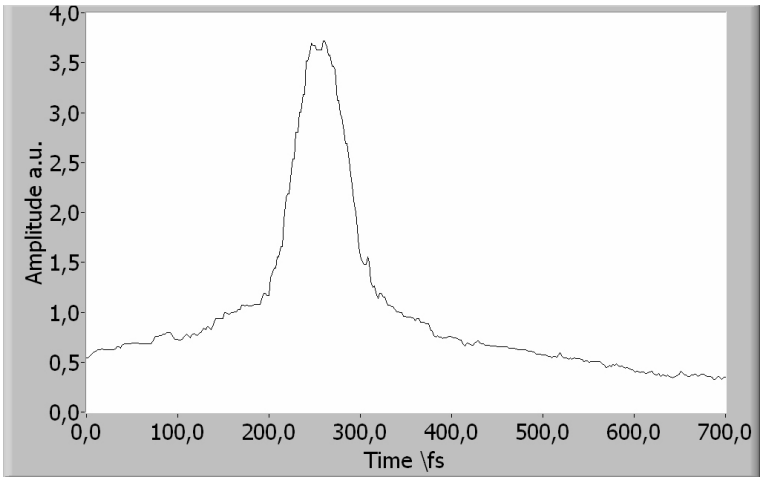

Figure 61: This measurement shows the auto-correlation diagram with a linear pattern applied to the SLM.

sections 3.9).

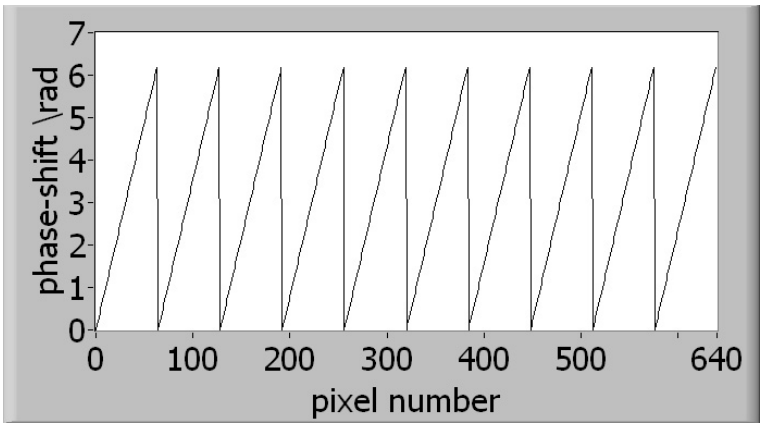

Figure 62: The figure shows a sawtooth pattern, which is impressed to the SLM. The maximum amplitude is 2π and the period of the sawtooth pattern is 10.

The comparison of the simulation of the auto-correlation signal in figure 65 and the measured auto-correlation signal in figure 66 shows a good agreement. That means that the calibration curve in section 4.4 and the SLM setup deliver a controllable laser pulse modulation.

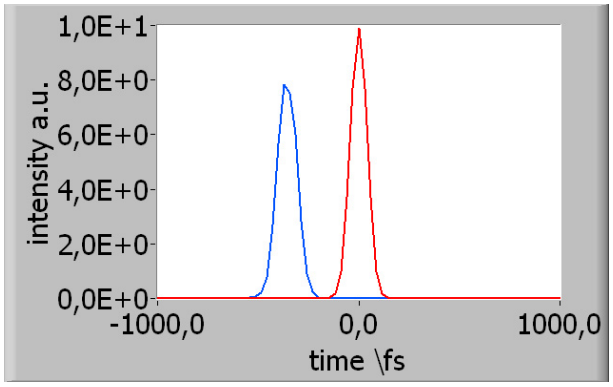

Figure 63: The simulation of the intensity against time shows in case of an even-modulo-break sawtooth pattern a time-shift of the final pulse (blue line) respective to the initial pulse(red)

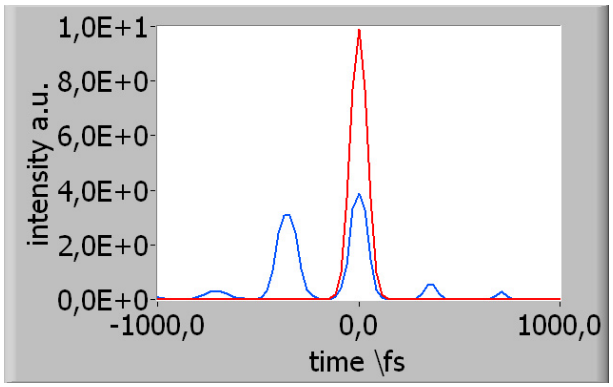

Figure 64: This simulation of an intensity signal has been plotted in case of a sawtooth pattern with modulo break at π comparing to the initial laser pulse intensity signal (red line). The diagram shows several peaks beside the main peak (blue line), these peaks are replicas. The sawtooth pattern includes 10 periods.

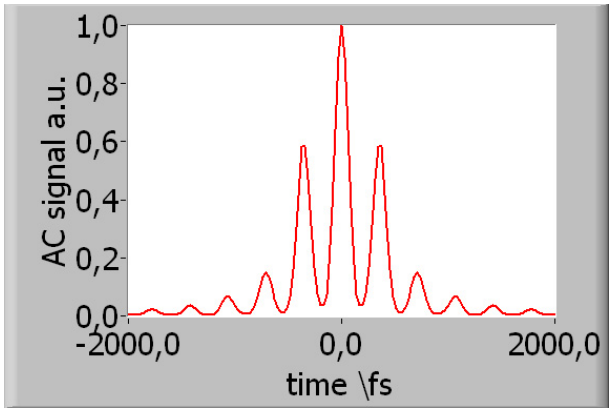

Figure 65: This simulation of an auto-correlation signal has been plotted to a sawtooth pattern with modulo break at π. The diagram shows several peaks beside the main peak, these peaks are replicas of simulation result in figure 63. The sawtooth pattern includes 10 periods.

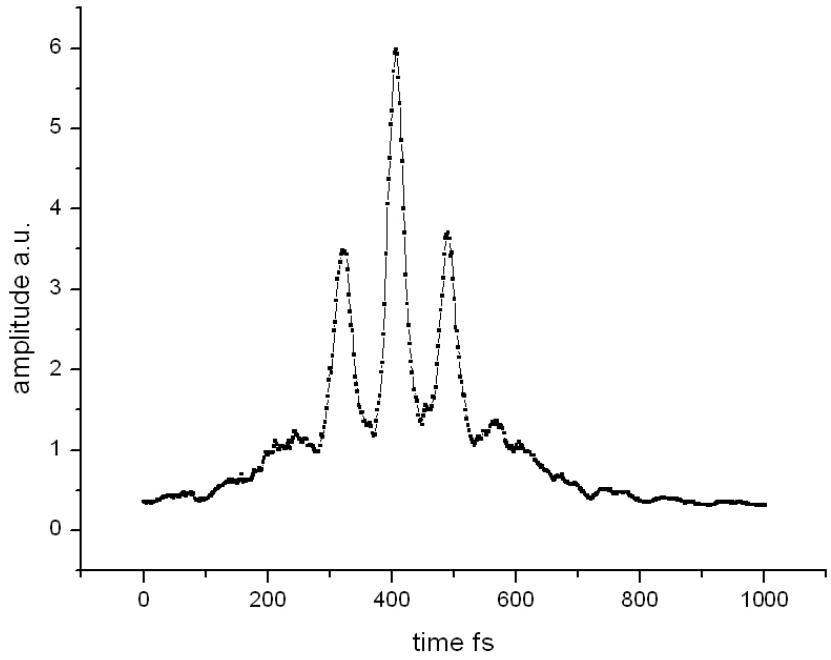

Figure 66: This measured diagram of an auto-correlation signal has been plotted for a sawtooth pattern with modulo-break at π. The diagram shows several peaks beside the main peak. These peaks are replicas. The sawtooth pattern includes 10 periods.

Sin pattern

The next test pattern is a *sin*-pattern, this pattern is more complicated as a linear pattern and it can clarify, if the SLM is able to shape the laser beam also in a periodic way, which is only possible with a valid calibration curve and a good adjustment of the SLM setup.
Also in this case, the modulated pulse will be detected by an auto-correlator; this auto-correlator uses SHG, so to understand the measured auto-correlation signal it is necessary to understand the influence of sinusoidal phase-modulations on a SHG which is described in section 2.8.
To simplify the expression for the complex spectral envelope of the modulated electric field in case of second harmonic (see equation 71), one can comprise the specification of the initial laser pulse. The ideal initial laser pulse has a central wavelength of $\lambda = 800\,\text{nm}$ and a bandwidth of $\Delta\lambda = 30\,\text{nm}$. For $\Delta\Omega_1$ follows from [8]:

$$\Delta\Omega_1 \approx \frac{2\pi c}{\lambda^2}\frac{\Delta\lambda}{\sqrt{2ln2}} \tag{125}$$

Thus, $\Delta\Omega_1$ is about 75 THz. Hence, the modulation frequency is in the range of $\Delta t \approx 0,1ps$. The term of the first order of the Bessel function arises with the last two values to $exp\left(-\frac{1}{8}(75THz \cdot 0,1ps)^2\right) \approx 0,1\%$ (see section 2.8). This value is negligibly small. This allows an approximation of the final field envelope $\tilde{\mathfrak{e}}_2(\Omega_2)$ by the $zero^{th}$ order of the summand, which includes the Bessel-function. It is:

$$\tilde{\mathfrak{e}}_2(\Omega_2) \propto e^{-\frac{1}{2}\left(\frac{\Omega_2}{\Delta\Omega_1}\right)^2} J_0\left(2\phi cos\left(\frac{\Delta t\Omega_2}{2} + \psi\right)\right) \tag{126}$$

A criteria for the approximation is

$$\Delta\Omega_1\Delta t > \sqrt{-8ln\left(\frac{|\alpha_1|}{|\alpha_0|}\right)}. \tag{127}$$

The result of the last calculation is that a sinusoidal phase modulation ends in the case of second harmonic generation in an amplitude modulation. In this case the auto-correlation signal has to be periodic.
To simulate this discussed modulation, a sinusoidal pattern (see figure 67) with a maximal amplitude of 8π and with 10 periods is generated. The result is indeed a periodic second order background free intensity correlation (see figure 68).

The spectral modulation frequency was 0.35 ps, which allows the approximation (equation 126). The same pattern is used in the measurement, always regarding the calibration curve and the fact that the laser passes the SLM twice. The results of the measurement is shown in figure 69. It shows the same periodical developing as seen before in the simulation (figure 68). Beyond, the small

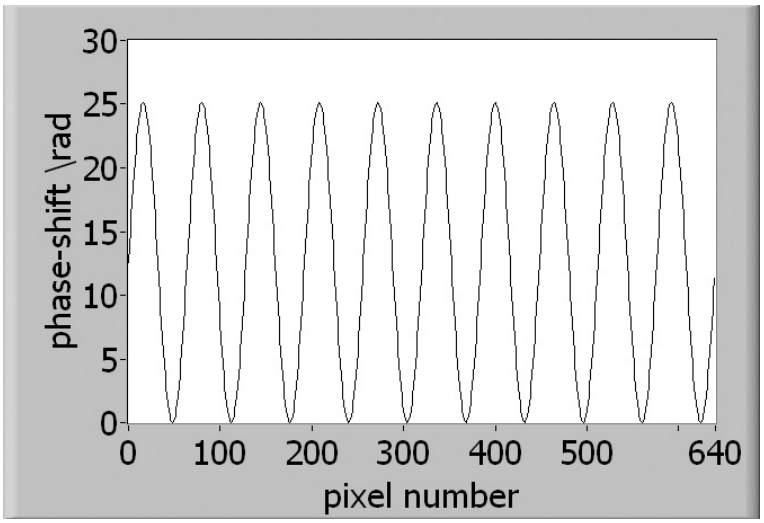

Figure 67: The impressed sinusoidal pattern with an amplitude of 8π and 10 periods.

maxima between the main maxima are shown in the simulation and are also delivered by the measurement. Just the temporal distance between the peaks are not the same. In the temporal distance in the simulation is twice as large as in the measurement. This is a result of the fact that the beam propagates twice through the SLM. In conclusion, the SLM works well and is able to modulate the laser beam with periodic pattern, too. The last steps before building up the whole setup, the laser, the fiber, the grating compressor and the SLM, is to simulate the TEO laser transport.

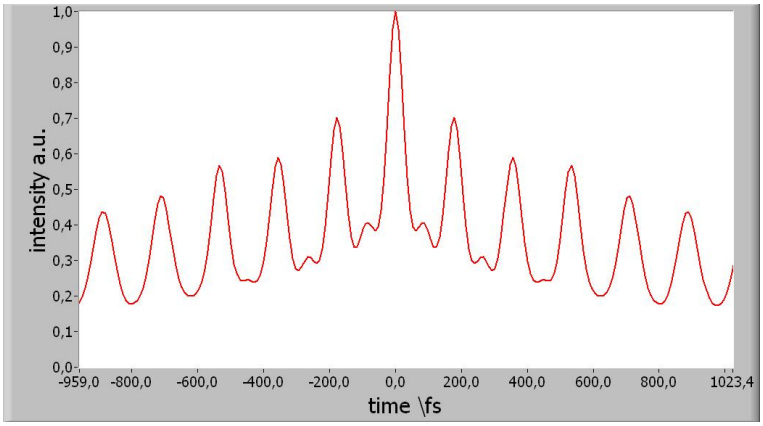

Figure 68: The simulated auto-correlation signal of the sinusoidal modulated laser beam. The modulation function has an amplitude of 8π and 10 periods

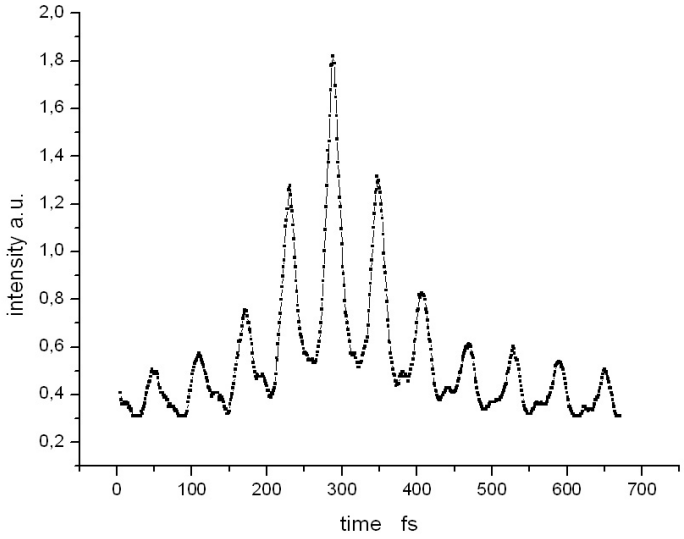

Figure 69: The measured auto-correlation signal of the sinusoidal modulated laser beam. The modulation function has an amplitude of 8π and 10 periods.

4.8 Simulation of the laser transport

The entire laser transport setup can now be simulated with a Lab2 [16] program. The simulation of the TEO laser transport starts with a Gaussian laser light source with a central wavelength of 800 nm and a bandwidth of 30 nm. The laser pulse is detected by an intensity detector and a spectrometer. The simulation includes all dispersive elements (lenses, ...) where the 170 m long fiber is approximated by SQ1 material, the grating compressor and the spatial light modulator. The two last elements compress the pulse back to its initial pulse duration.
The simulation is used to predict the expected FWHM after the dispersion compensating elements and the exiting pulse structure. The simulation also allows optimizing the setup regarding the settings of grating compressor and SLM. The pulse shaper is simulated by a LCD array with 640 pixels including gaps. The LCD is embedded between two gratings and two focussing optical elements in a 4-f arrangement. The grating equation is used to calculate the wavelength at each pixel which in turn means that the nonlinear character of the grating diffraction is implemented.
The result of the simulation with optimized parameters is shown in figure 70. The initial pulse duration of 32.5 fs could be recompressed using the grating compressor to 77 fs FWHM. The increase of the pulse duration by a factor of two is caused by dispersion produced by the grating compressor and the SLM.

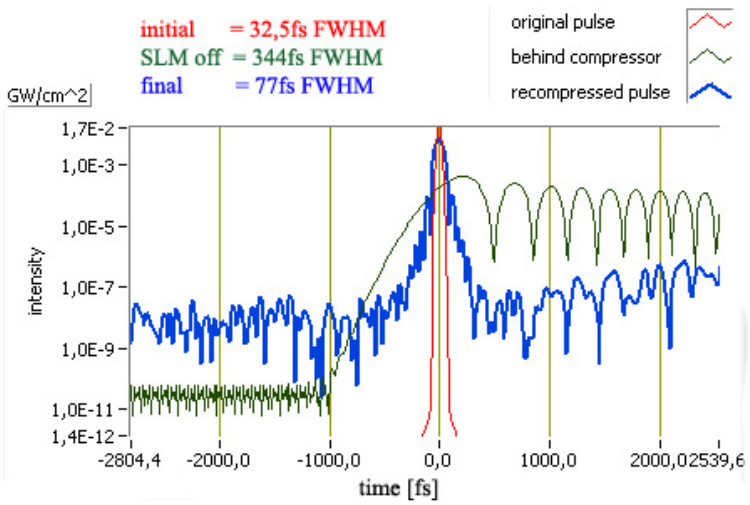

Figure 70: The Lab2 simulation shows that the grating compressor compresses the bunch down to 344fs, but it produces higher orders of dispersion. The SLM compensates for the higher orders of dispersion and compresses the pulse down to 77 fs FWHM.

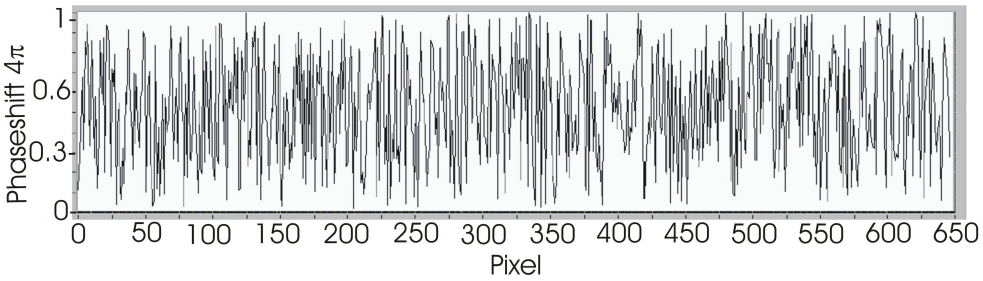

Figure 71: The last pattern generated by the genetic algorithm. The diagram was generated by 1000 cycles of the genetic process. The initial population had 100 individuals and 30 individuals have been chosen to pass the next step of the genetic algorithm. With this pattern the FWHM of the laser pulse could be recompressed to 73.4 fs.

Simulation of Adaptive Dispersion Compensation with Lab2

To insure that a genetic algorithm will be able to compensate dispersion, especially higher orders of dispersion, the algorithm will be integrated in a simulation, which includes a Gaussian laser, the fiber, the grating compressor and the SLM. As already seen in the basic tests, the SLM will be controlled by a LabView program. A Lab2 program allows combining the genetic algorithm with the virtual femtosecond laboratory. The SLM, which will be used in this simulation, makes possible giving each pixel a certain phase-shift, this phase-shift will then be defined by the genetic algorithm. A two photon conduction diode (TPC) delivers the needed feedback signal. The simulation will be stopped, when the signal reaches the expected value which belongs to a laser pulse duration less than 100 fs and does not change more than 1%.

The simulation shows that the genetic algorithm works as expected (see figure 72) and the FWHM could be reduced to $\approx 73fs$. The run of the curve of the SHG signal starts with a slow increase before the signal increases exponentially up to a slowly increasing plateau. The generated pattern seems to permit no conclusion about the modulated pulse. The pattern has a random character. The reason is the modulo break at certain pixel. A similar problem was given in section 11.4; in that case, there was also a diagram, which had modulo breaks. But there is enough information about the physics to unfold the calibration curve with modulo breaks. For example, the fact that the calibration curve is a decreasing function, and that the curve has no leaps, because the molecules of the LC matrix orientate continuously. But in the case of the pattern, which was generated by the genetic algorithm, there is not enough information. It would be necessary to know more about the phase of the laser pulse, which has to be shaped. The pattern in figure 71 allows one to appreciate the rise of the modulation-function and the number of modulo breaks. But the definite modulo

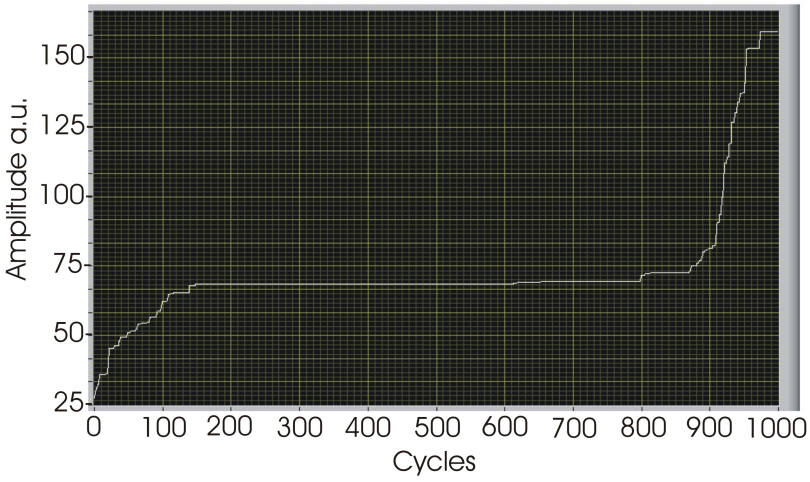

Figure 72: This diagram shows the run of the TPC signal-curve of each generation. It shows the expected run, with an exponential increase in the middle and a plateau at the end of the 1000 cycles. The settings for this diagram are the same as in curve 71.

break can not be determined. The breaks can be modulo π or modulo 2π. The pattern in figure 71 also shows that the SLM works at the threshold, which is determined by the Nyquist limit.
Accurate information about the phase of the laser pulse can be achieved by diagnostic tools such as Frequency Resolved Optical Gating (FROG).

The next step is to recompress a laser pulse, which has passed some dispersive elements. In this case, the SLM should not operate at its limit. Thus, the generated pattern should have a clear structure.

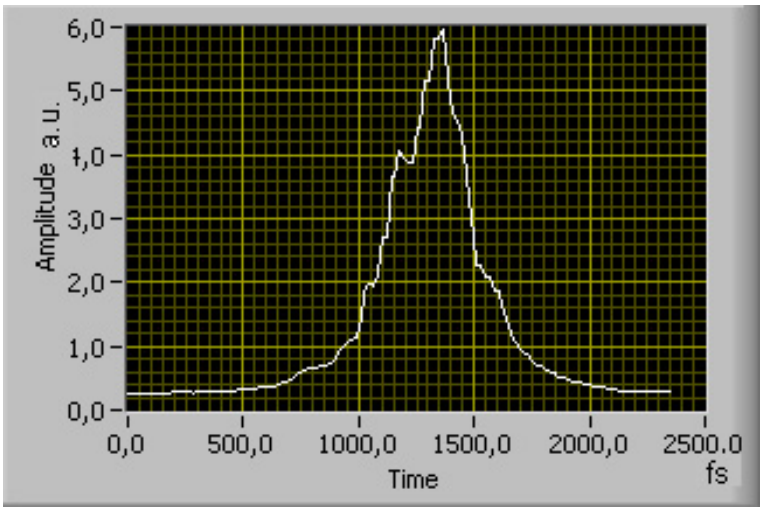

Figure 73: This diagram shows the auto-correlation signal of the laser behind the dispersive elements and the SLM, which is switched-off. The FWHM in this case is autocorrelated about (356 ± 10) fs.

Recompression of chirp induced by a glass rode using the Genetic Algorithm

To test the SLM as a stand-alone system for compensation of dispersion, a setup is created which includes the initial Ti:Sa laser pulse, dispersive elements and the SLM including the GA.
The dispersive elements are two polarizers, two lenses, a rotator and two wave-plates. The genetic algorithm should also compensate the "tail" (figure 60). Therefore, the algorithm runs over 12 h. Always regarding the calibration curve and taking the BBO signal as feedback for the algorithm. The results of this run are shown in figure 74 and figure 75.

The figures 73,74 and 75 show that the SLM is able to recompresses the chirp induced by some glasses by using the genetic algorithm. One can see that the pulse is compressed from a FWHM of (356 ± 10) fs with glass rod and without SLM (see figure 73) to a FWHM of (100 ± 10) fs and the tail, seen in figure 60, is also compensated and this auto-correlation signal shows a Gaussian profile. Thus, the genetic algorithm also works in the real. The generated pattern, which includes the necessary phase-shift to recompress the pulse, has, compared to the simulated pattern in figure 71, a conspicuous structure (see figure 74).
The pattern is parabolic with modulo breaks. This means that the glasses produce basically a linear chirp. Another conspicuity is that the generated pattern is not symmetric to the center. The center is shifted by 20 pixels, which means a shifting of wavelength by 2 nm. The central wavelength is therefore 798 nm instead of 800 nm. The next step is to recompress the pulse, which has passed the fiber, by

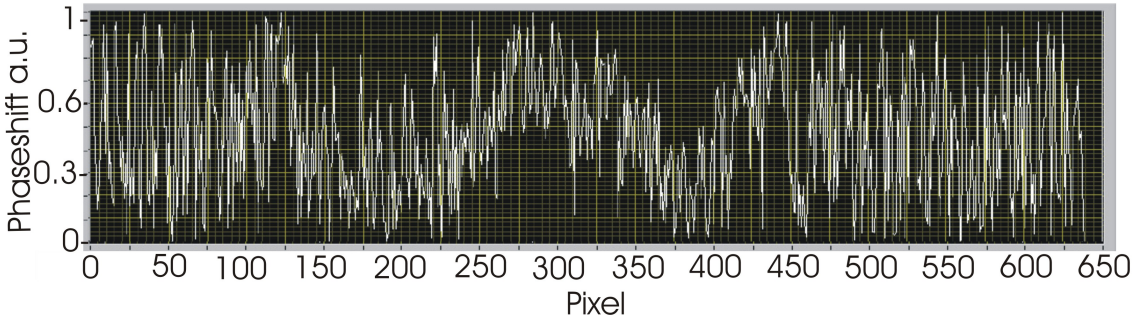

Figure 74: This is the final pattern that recompressed the laser pulse down to (100 ± 10) fs. The pattern has been a specific parabolic structure.

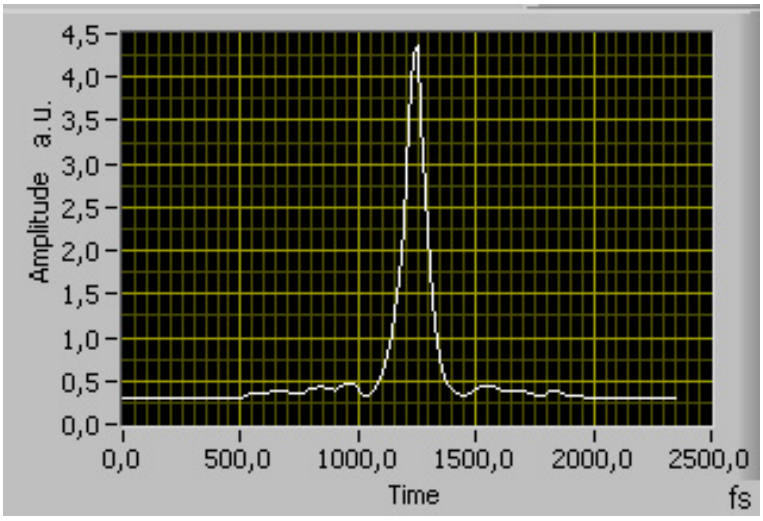

Figure 75: This diagram shows the auto-correlation signal of the laser after 1000 cycles of the genetic algorithm.

using the grating compressor and the SLM together with the genetic algorithm. Now every important element for dispersion free fiber delivery of the Ti:Sa laser pulses have been chosen, described and tested. The whole setup can now be put into operation.

Adaptive dispersion compensation for fiber delivery of femtosecond pulses for the TEO experiment

The simulations and the tests have shown that it is possible to transport laser pulses in a fiber over a distance of 170 m with nearly no loss on pulse structure and pulse duration, the simulation of the whole setup has shown that it possible to compress the pulse after the fiber back down to ≈ 74 fs. An auto-correlation behind the grating compressor, the SLM and the fiber should deliver a FWHM of (80 ± 20) fs. Therefore the setup has been set up like it is shown in figure 17. To achieve a SLM pattern which compresses the pulse back down to the expected FWHM of (80 ± 20) fs, the genetic algorithm was run over two days.
The results are shown in figure 76, figure 77 and figure 78.

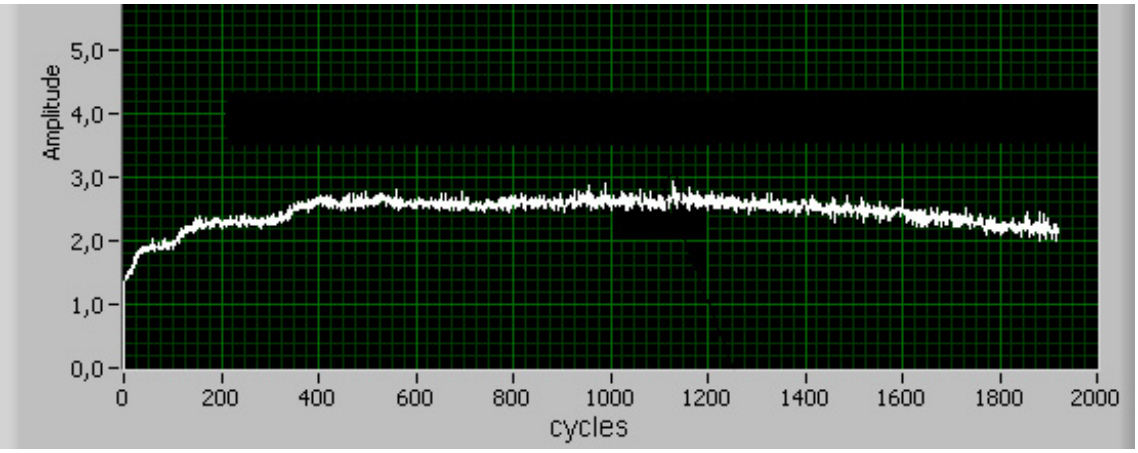

Figure 76: This diagram shows the run of the feedback-signal curve.

Figure 76 shows that the increase at the beginning of the curve is transferred into a plateau, which starts to decrease after 1100 cycles. Therefore, the pattern belonging to the maximum feedback signal at cycle number 1012 has been taken to compress the laser pulse (see figure 77).

The SLM was able to compress the pulse from (1.6 ± 0.2) ps to (92 ± 20) fs. The SLM pattern was acquired by analyzing the feedback development (figure 76), because a certain SLM pattern belongs to each value of the feedback signal. The pattern which belongs to the maximum value of the feedback signal is shown in figure 77. This pattern was used to achieve the final compression back to (92 ± 20) fs. The pattern is quite unstructured, but this has already be seen and discussed in the simulation of the genetic algorithm (section 4.8). Another conclusion from this pattern is that the laser is well aligned because there is a local minimum at pixel 340 with small rises to the left and to the right of the center. This local minimum is based on the fact that the phase-shift has to increase at the border of the SLM LC matrix (see section 3.9) The decrease of the feedback-

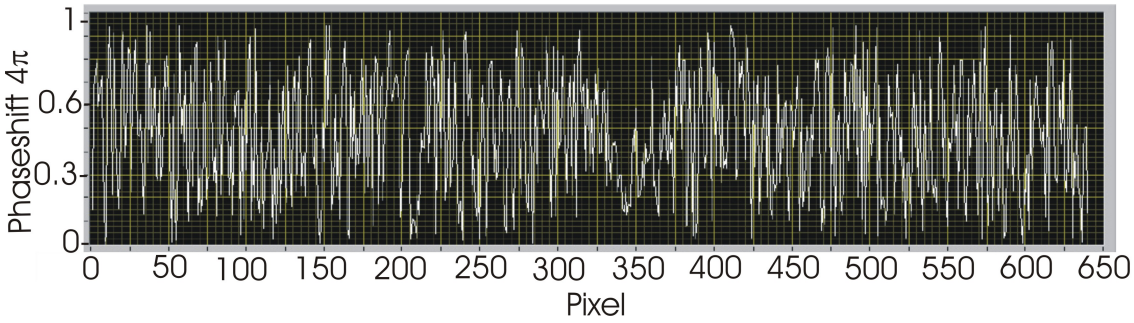

Figure 77: This diagram shows the final pattern, which has been used to compress the pulse. This pattern was determined by the feedback-signal curve.

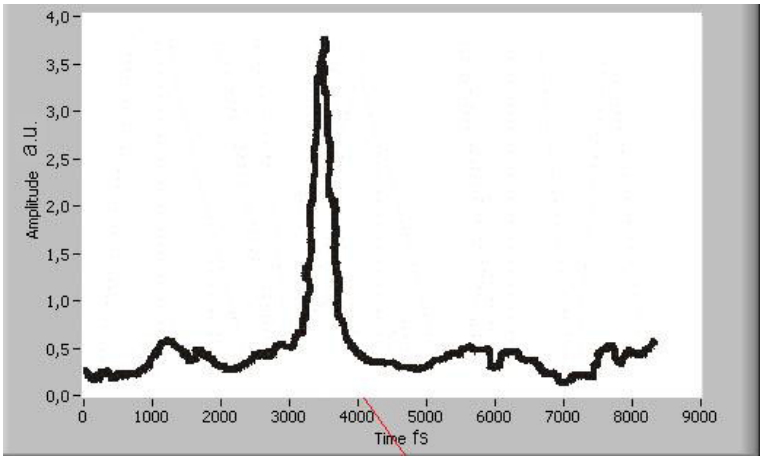

Figure 78: This auto-correlation signal presents the final signal behind the fiber, the SLM and the grating compressor.

signal after 1100 cycles does not agree with the simulation. A possible reason for this run of the feedback signal might be the noise of the feedback signal, this has to be analyzed more precisely.
The outcome of this are two problems, the first is the "big tail" of the auto-correlation signal in figure 78, which contains nearly 90% of the signal. The remaining 10% of pulse, which has the correct compressed profile, is not enough for the electro-optic sampling, because the EO signal would be smeared over the whole "tail". The other problem is the seemingly unstructured final pattern (see figure 77). Just the center of the pattern has an obvious structure. This enables us to check if the SLM setup is aligned correctly. Therefore the pattern has to have a local minimum and an obvious structure, because the phase-shift which is impressed on the center of the pulse in the Fourier plane has to increase slowly out of the local minimum. The reason therefore is, that the dispersion increases

out of the local minimum (see simulation in section 4.8). As already seen in section 4.8, it is not possible to conclude from the final pattern to the impressed phase-shift, which modulates the pulse to a compressed pulse. Just the fact that there are many modulo breaks in the pattern, which means that the impressed modulation-function is steep and the SLM works at its limit (see Nyquist-limits in section 3.9).
It is necessary to use other diagnostic tools, which are able to deliver more information about the phase of the laser pulse, which has to be compressed. A Frequency Resolved Optical Gating (FROG) is able to deliver such information, which will allow understanding of the final pattern more precisely and will also allow unfolding the final pattern to get information about the impressed modulation-function.

4.9 Laue Diagram of the ZnTe Crystal

Laue-Method

Before the ZnTe crystal can be installed in the vacuum chamber of the VUV-FEL beamline, its orientation and symmetry has to be verified. This is done by the Laue Method. This method uses a X-ray beam with a continuous wavelength distribution. The X-ray beam is collimated and aligned on the surface of a crystal.

The Laue-diffraction is detected by an X-ray sensitive film placed either in the transmitted or back-reflected setup. The transmission method a very thin crystal, otherwise the absorption of X-rays in the crystal is too high. The intensity of diffracted beam is proportional to the volume of the crystal.

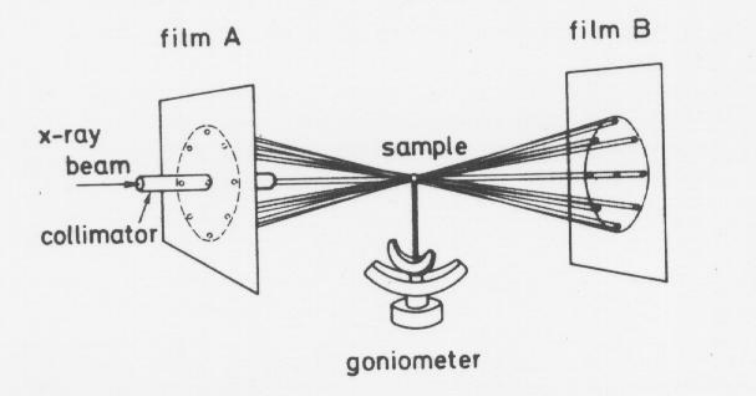

Figure 79: The figure shows the two possible Laue setups, with A the back-reflection film and B the transmission film [22].

Figure 79 shows the two possible setups of detection, the transmission and the back-reflection one.

Because of the rather thick crystal of 250 µm, the back-reflection is used.

Laue Diagram Analysis of the ZnTe Crystal

Three ZnTe crystals with the same dimensions and orientation have been delivered glued onto a solid block (see figure 80). [h] The Laue diagram taken in back-reflection of the first ZnTe is shown in figures 81.

The distance between the sample and the collimator is 10 cm. The cathode voltage of the X-ray source is 60 kV with a current of 30 mA. The sample was exposured for 4 min. The ZnTe crystal was ordered such that it has a surface plane of $< 110 >$ and a vertical side plane of $< 001 >$ [14].

To analyse the data quantitatively, it is necessary to know more about the crystal structure of ZnTe. ZnTe is a member of the zincblende crystal group illustrated

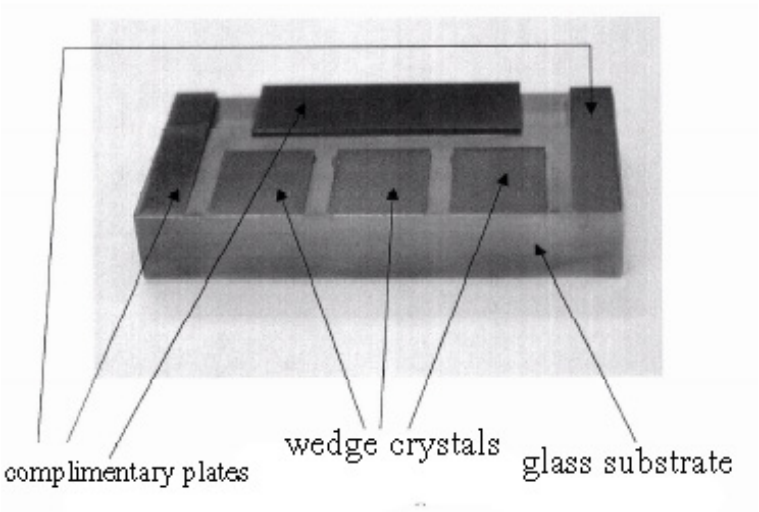

Figure 80: Photography of the delivered crystals and their mount

in figure 82. The Tellorid ions form a face-centered cubic array and the Zinc ions fill one-half of the tetrahedral holes. The Laue diagrams are analyzed by comparing them with diagrams taken for a well known crystal structure, which are illustrated in the "Laue Atlas" [6].

The analysis shows a good agreement between the illustrated diagram 83 and the measured diagram 81. Only a mismatching in the position of the spots, which are shifted out of the middle along the short edge of the crystal is observed. A possible reason for this is a tilt in the plane of the crystal with respect to its surface.
The simulation program "Lauept" [5] allows the calculation of Laue-diagrams in back-reflection of the lattice with a tilt-angle with respect to the incoming X-ray beam. The best match is been reached with an angle of 1° (see figure 84). The angle is acceptable for the TEO experiment and only a small reduction of the birefringence effect is expected [38]. In conclusion, the crystals each have the right orientation and can be used in the TEO experiment.
To exclude physical damage from the transport, the crystal has been analyzed with a microscope. The pictures are shown below in figure 85 and figure 86. The groves are caused by the polishing of the crystal.

An influence of the timing resolution, caused by the variation of the crystal thickness due to the groves can be neglected.

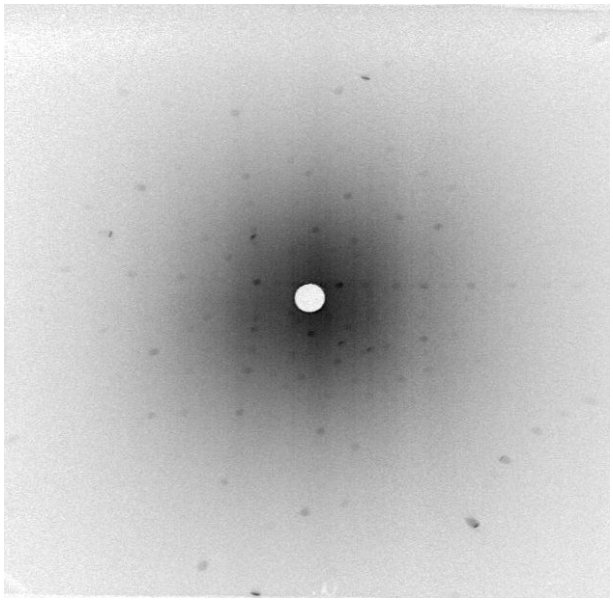

Figure 81: Laue diagram of the first ZnTe crystal taken by the back-reflection method

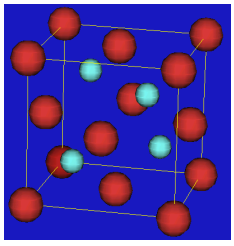

Figure 82: Structure of a Zinc Tellorid crystal [20]

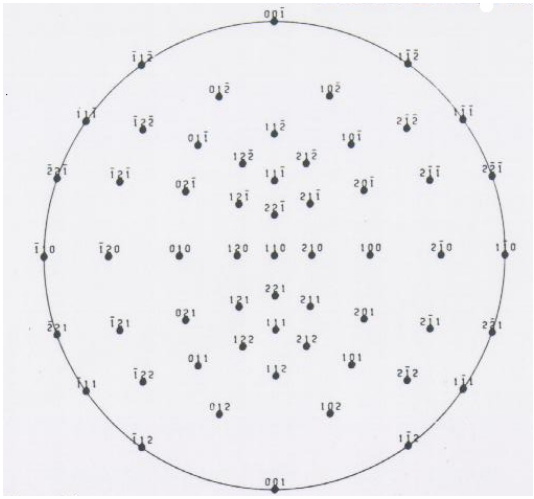

Figure 83: Calculated Laue diagram of a < 110 > ZnTe crystal in back-reflection method [6]

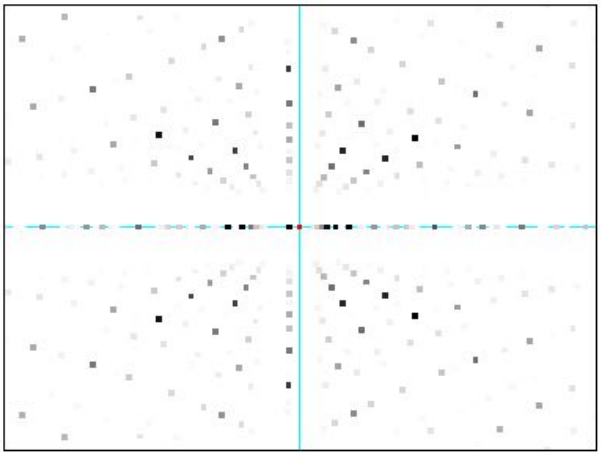

Figure 84: Simulated Laue diagram of a ZnTe crystal which is tilted by 1° in vertical-direction

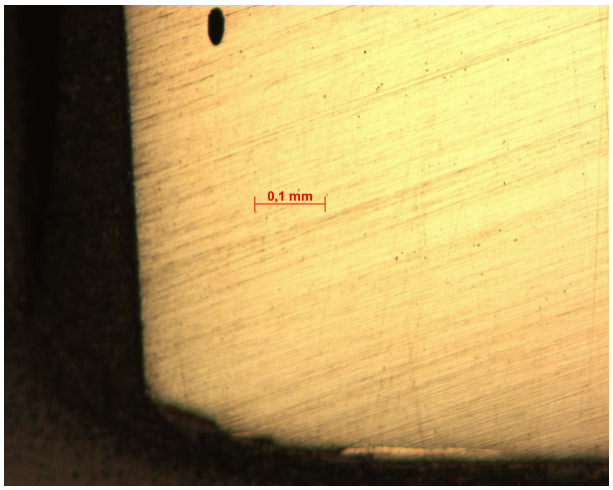

Figure 85: Photography of the left plane corner of the left crystal

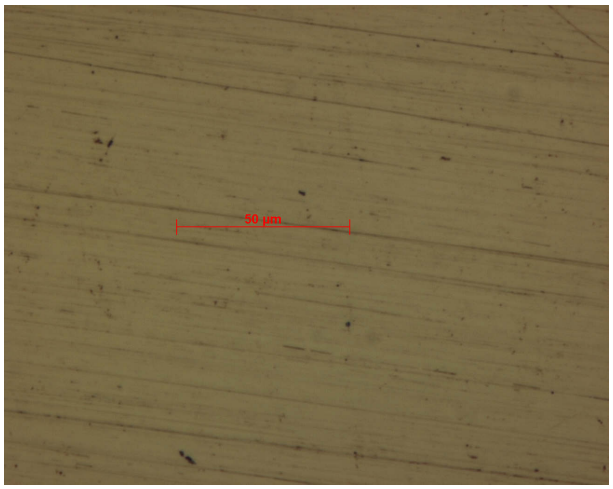

Figure 86: Photography of the right crystal with 500 times magnified, the cracks are caused by polishing and they have no influence on the sampling.

5 Conclusion and Outlook

A setup for electro-optic sampling was built up in the course of this diploma thesis. The decisive elements, the ZnTe, the SLM, the grating compressor and the fiber were simulated and tested.
The analyzes of the ZnTe crystal shows that the crystal has the correct symmetry, orientation and dimensions. Also, the imaging system in the tunnel setup was tested and is ready for timing measurements. So in regard to the ZnTe crystal and its imaging system, the electro-optic sampling can be carried out.
The ZnTe crystal is the heart of the TEO experiment, but the main part is the laser transport.
This laser transport has to get over a distance of 170 m, the laser pulses have to have a pulse duration in the sub-100 fs regime and the polarization must be maintained over the whole distance. It was shown that it is possible to achieve these requests. Regarding the polarization, the critical element is the fiber-optic, its polarization maintaining is determined to 0.020 ± 0.008 which means a h parameter of $(1.2 \pm 0.5) \cdot 10^{-4} 1/m$ and that only 2% of the initially fully polarized beam have been scattered while propagating in the fiber into the perpendicular polarization. .
To achieve femtosecond pulses at the crystal surface, it is necessary to transport the Ti:Sa laser pulses without dispersion, which would cause pulse broadening.
It was shown that a combination of a grating compressor and a SLM is able to compensate the dispersion. In this manner, it was possible to achieve a FWHM behind the fiber of 90 fs, but the "tail" of the pulse contains to much intensity. The "tail" should contain at most 30% instead of 90%. The simulation of the whole laser transport system delivers a minimum FWHM of 73 fs, so that the transport system still can be optimized.
The critical points of the laser transport system are the adjustment of the grating compressor and the SLM as well as the genetic algorithm. The genetic algorithm has to be run at least over 1000 cycles, which takes about 12 h. An advantage of this algorithm is the marginal demand on information about the pulse form and about the locations of the laser pulse spectrum at the LC matrix, this allows the starting of the algorithm also with slight deviations of alignment of the SLM and grating compressor setup.
But the adaptive dispersion compensation can be optimized by using Taylor coefficients, which will reduce the number of elements (640) substantially. This will also reduce the run-time of the algorithm. Therefore, it is necessary to know more about the phase of the dispersive laser pulse. This information will be delivered by a Frequency Resolved Optical Gating (FROG), this detector will be installed in the near future.
Finally, the problems, which are discussed during this work are not unsolvable and the principle of the TEO experiment are simulated and tested. But the last point which has to be established is the synchronization of the laser with the FEL.

So, if the synchronization, which was not part of this thesis, works very well, the first measurements with this kind of sub-100 fs bunch arrival-time monitor can be put into practice.

Bibliography

[1] John. M. J. Madey, *Free Electron Laser* **J. Appl. Phys 42, 1906** (1971)

[2] A. H. Zewail, *Femtochemistry: Ultrafast Dynamics of the Chemical Bond* World Scientific, Singapur, (1994)

[3] Bernd Steffen et all *Bunch length measurements at the SLS limac using electro optical sampling* Proceedings of the 2004 FEL Conference, **392-394** (1994)

[4] Wolfgang Demtröder: *Atome, Moleküle und Festkörper* , Springer Verlag Berlin (2000)**Band 3**

[5] Huang, Xion Rong *White -Beam X-ray diffraction pattering* (1998-2003)

[6] Preuss, Eduard; Krohl Urbean, Bernhard; Butz, Rainer *Laue Atlas* Bertelsmann (1973)

[7] N.A. Papadogiannis, et. all *On the feasibility of performing nonlinear autocorrelation with attosecond pulse trains* Applied Physics B: Lasers and Optics (2003) **Pages: 721 - 727**

[8] Hacker, Martin *Neue Möglichkeiten und Anwendungen der Phasenmodulation ultrakurzer Laserimpulse* Dissertation Physikalisch- Astronomische Fakultät der Friedrich-Schiller-Universität Jena (2003)

[9] Lupulescu, Cosmin *Femtosekunden-Analyse und Rückkoppelungskontrolle von molekularen Prozessen in organometallischen und alkalischen Systemen* (2004)

[10] Gregor Stobrawa: *Aufbau und Anwendung eines hochauflösenden Impulsformers zur Kontrolle ultrakurzer Laserimpulse* Dissertation, Physikalisch-Astronomische Fakultät der Friedrich-Schiller-Universität Jena (2003)

[11] Kasper, Axel *Erzeugung und Charakterisierung ultrakurzer Lichtpulse aus Titan:Saphir Laser Oszillation* Dissertation (2002)

[12] Jonas Burghoff: *Formung eines Multi-Terawett-Laserimpulses* Diplomarbeit, Physikalisch- Astronomische Fakultät der Friedrich-Schiller-Universität Jena (2002)

[13] Bartelt, Andreas *Steuerung der Wellenpaketdynamik in kleinen Alkaliclustern mit optimierten Femtosekundenpulsen* Dissertation (2002)

[14] Holger Schlarb, Stefan Düsterer, et. all: *Proposal for a Sub-100 fs Electron Bunch Arrival-Time Monitor for the VUV-FEL at DESY* Paper, Proceedings of EPAC 2004, Lucerne, Switzerland (2004)

[15] S.-H. Lee et. al.: *Adaptive dispersion compensation for remote fiber delivery of NIR femtosecond pulses* Opt. Lett. (2004) **vol 29 P2602**

[16] B. Schmidt et. al.: *Lab2 - A virtual femtosecond laser lab* http://www.lab2.de

[17] Eugene Hecht: *Optik* Oldenbourg (1998) **Bd. 2**

[18] Jean-Claude Diels and Wolfgang Rudolph: *Ultrashort Laser Pulse Phenomena* Optic and Photonics, Academic Press California (1995) **Bd. 1**

[19] A.M. Weiner: *High-resolution femtosecond pulse shaping* Paper, Optical Society of America (1998)

[20] ZnTe structure http://physics1.byu.edu/ stokesh/zns.htm

[21] Agrawal, G.P. *Nonlinear Fiber Optics* Harcourt Publisher Ltd., ISBN 0120451433 (2001)**3. Auflage.**

[22] Cullity, B.D. *Elements of X-ray diffraction* Upper Saddle River Pearson Education,(2001) **third edition**

[23] Spence, D.E.; Kean, P.N.; Sibbett, W. *69-fsec pulse generation from a self-mode-locked Ti:sapphire* In: Optics Letters 16 (1991) **S.42-44**

[24] Moulton, P.E. *Spectroscopic and laser characteristics of* $Ti : Al_2O_3$ Journal of the Optical Society of America B 3, Nr. 1, (1986) **S. 125-133**

[25] Moulton, P.E. *Tunable solid-state lasers* In: Proceedings of the IEEE 80, Nr. 3, (1992) **S. 348-364**

[26] Morgner, U.; Kärtner, F.X.; et. all *Sub-two-cycle pulses from Kerr-lens mode-locked Ti:sapphire laser* In: Optics Letters 24; (1999) **S. 411-413**

[27] Comly, J. and Garmire, E. *Second harmonic generation from short light pulses* Appl. Phys. Lett., (1968) **Vol 12 Page 7-9,**

[28] Martinez, O.E. *Grating and Prism compressor in case of finite beam size* Journal of Optical Society America B **1986**

[29] Martinez, O.E. *3000 times grating compressor with positive group velocity dispersion - apllication to fiber compensation in 1.3 -1.6 μm region* IEEE Journal of Quantum electronics (1987)

[30] ZEMAX Development Corporation *ZEMAX* Optics Simulation Software (2005)

[31] *Anleitung des SLM-S 640/12*

[32] Rullire, C. *Femtosecond Laser Pulses, Principles and Experiments* Springer, Berlin Heidelberg New York (1998)

[33] Kneubühl, Fritz K.; Sigrist, Markus W.; *Laser* Teubner Verlag

[34] Yariv, Amnon *Quantum Electronics* John Wiley and Sons (1989) **third edition**

[35] Bronstein, Semendjajew, et. all. *Taschenbuch der Mathematik* Verlag Harri Deutsch (1993) **4. edition**

[36] Holland, J. *Artifical Genetic Adaption in Computer Control Systems* Dissertation, University of Michigan (1971)

[37] http://www.hpk.co.jp/Eng/products/SYSE/streakE.htm *Hamamatsu Streak Camera Specification*

[38] Schmüser, P. et. all. *Numerical Studies on the Electro-Optic Sampling of Relativistic Electron Bunches* TESLA Report (2005)

[39] http:
www.fiber-optics.info *Different Types of fiber*

[40] http://sales.hamamatsu.com/index.php?id=13195780 *Hamamatsu H6780-20 Photosensor Module*

[41] Agrawal, Govind P. *Nonlinear fiber optics* University of New York, Rochester (2000) **Third Edition**

[42] Apolonski, A. ; Poppe, A. ; Tempea, G. ; Spielmann, C. ; Udem, T. ; Holzwarth, R. ; Haensch, T. W. ; Krausz, F.: *Controlling the Phase Evolution of Few-Cycle Light Pulses.* In: Physical Review Letters 85 (2000), **S. 740-743**

[43] Gaeta, A. L.: *Nonlinear propagation and continuum generation in microstructured optical Fibers.* In: Optics Letters 27 (2002), **S. 924-926**

[44] Genty, G. ; Lehtonen, M. ; Ludvigsen, H. ; Broeng, J. ; Kaivola, M.: *Spectral broadening of femtosecond pulses into continuum radiation in microstructured Fibers.* In: Optics Express 10 (2002), **S. 1083-1098**

[45] Dudley, J. M. ; Provino, L. ; Grossard, N. ; Maillotte, H. ; Windeler, R. S. ; Eggleton, B. J. ; Coen, S.: *Supercontinuum generation in air-silica microstructured Fibers with nanosecond and femtosecond pulse pumping.* In: Journal of the Optical Society of America B 19 (2002), **S. 765-771**

Chapter 1

Appendix

0.1 Lab2 Simulation environment

Lab2 is based on the theory of ultrashort laser pulses which is described in section 2.1. Figure 1.1 shows a typical "frontpanel" of a Lab2 simulation program. The program includes a Gaussian laser pulse source a linear dispersive element and an intensity detector as well as a spectrometer. The frontpanel shows the control panel for the laser source and the dispersive element, Lab2 includes the most common types of glass, for example SQ1 and the frontpanel shows the diagrams of the intensity and the spectrum. Figure 1.2 shows the "blockdiagram" of the

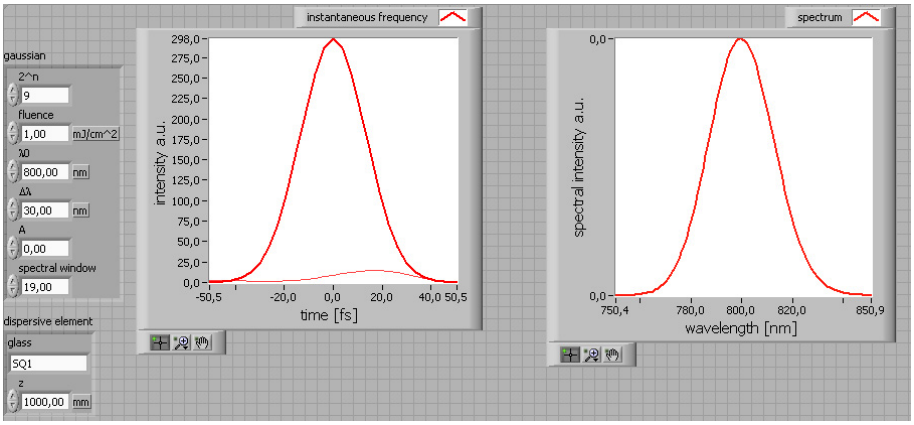

Figure 1.1: This figure shows a LabView Frontpanel of a Lab2 simulation program.

Lab2 simulation program. The blockdiagram is the programming environment. The connections of the certain Lab2 virtual instruments (vi) are established at the blockdiagram environment. The red lines between the elements includes every necessary information about the laser, it can be seen as a laser beam. It is possible to connect several elements at the same red line.

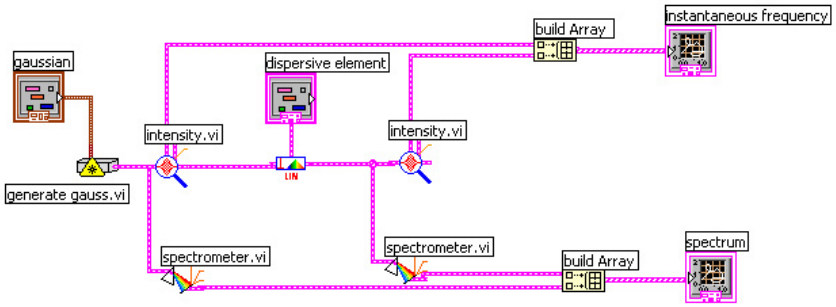

Figure 1.2: This figure shows the blockdiagram of the Lab2 simulation program.

0.2 Determination of the focal length of the focusing elements in the 4-f stretcher

The 4-f stretcher has three degrees of freedom:
The focal length f, the grating constant d and the angle of incidence α. These parameters have to be combined in such a way that the width of the laser spectrum in the Fourier plane is adapted optimally to the width of the modulator, which means that the frequency interval on the modulator should be three times the FWHM ($\Delta\omega$) of the laser spectrum. This is a compromise between resolution and cut-off of the laser spectrum by the modulator window. Figure 1.3 shows the correlation between the focal length and the grating parameters. One has to pay attention that the incident laser beam with the central wavelength ω may not be cut off by the lens, this confinement limits the difference between the angle of incident α and the diffraction angle $\beta(\omega_l)$. Another condition is that the diameter of the lens has to be at least as large as the width M of the modulator. These condition allow the calculation of the focal length by a given grating constant and a given width of the modulator M.
It is:

$$arctan\left(\frac{M}{f}\right) = |\alpha - \beta(\omega_l)| \tag{1.1}$$

$$arctan\left(\frac{M}{2f}\right) = \left|\frac{\beta\left(\omega_l + \frac{3}{2}\Delta\omega\right) - \beta\left(\omega_l - \frac{3}{2}\Delta\omega\right)}{2}\right| \tag{1.2}$$

With these equation and the grating-equation:

$$sin(\alpha) + sin(\beta) = m \cdot \frac{2\pi c}{g \cdot \omega}, \tag{1.3}$$

where m is the order of diffraction, one can calculate an ideal combination of grating and focal length.

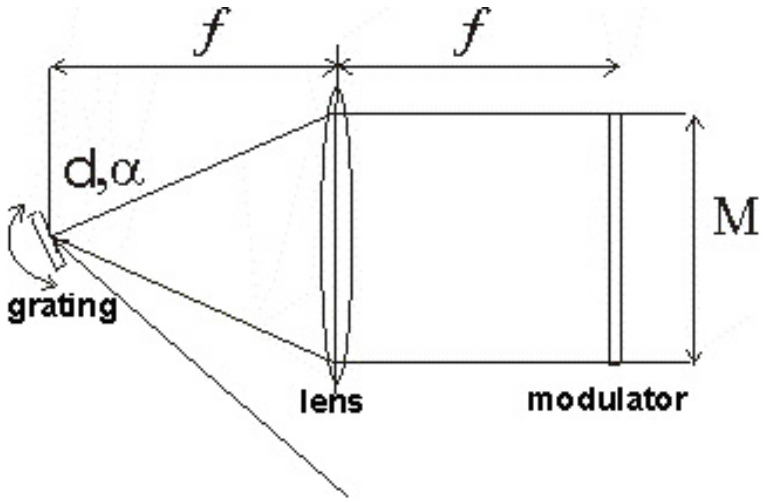

Figure 1.3: The focal length of the lens with given grating parameters should be chosen in such a way that the laser spectrum at the Fourier plane is optimally adapted to the width of the modulator window. Also, the incident angle on the grating α has to be chosen such that the focusing optic does not cut off the laser beam.

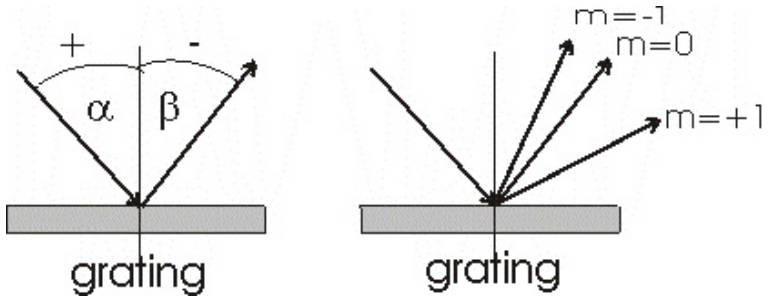

Figure 1.4: Definition of the angles and the order of the grating equation

0.3 Laue diagrams of the remaining two crystals

0.4 Photography of the ZnTe crystals

0.5 Power Balance

Obviously, every optical element produces losses of laser beam power. For the electro-optic sampling it is necessary to have enough power to get a good feedback and EO signal. From experience to realize a good feedback signal, it is necessary to have a beam power with more than 12 mW. Therefore, the power before the ZnTe crystal has to be calculated starting with the initial power of 330 mW. The main energy losses are produced by the fiber coupling. The fiber together with

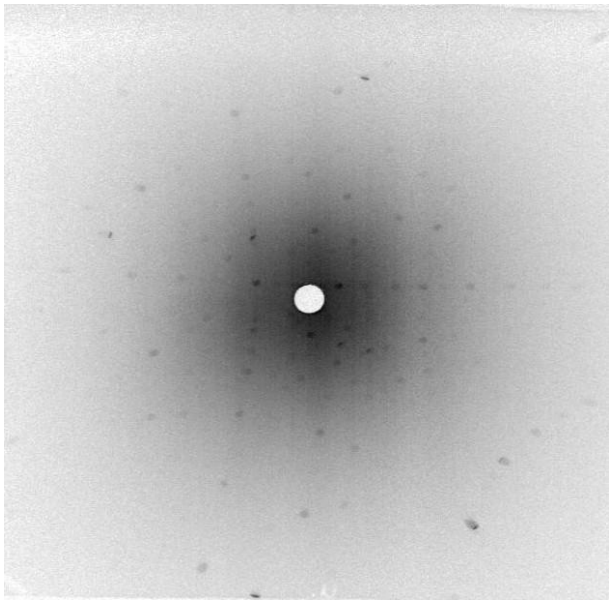

Figure 1.5: Laue diagram of the center ZnTe crystal

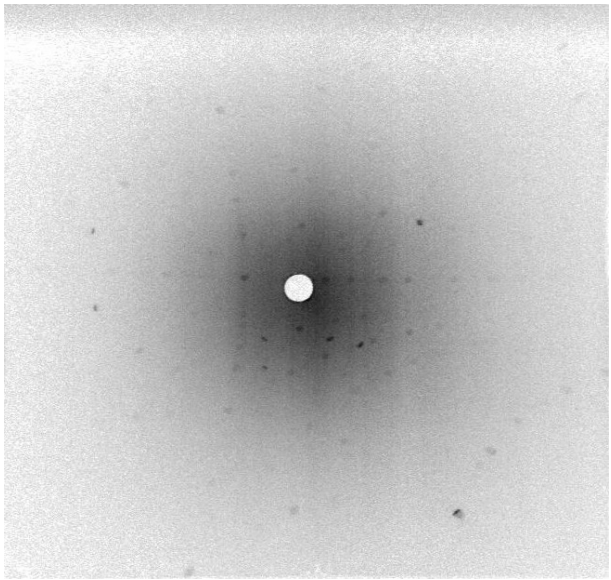

Figure 1.6: Laue diagram of the right ZnTe crystal

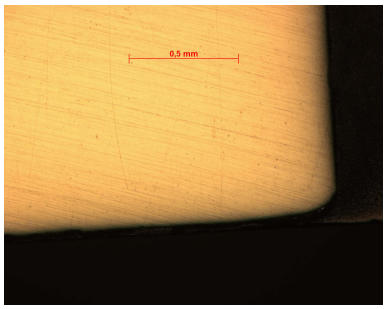

Figure 1.7: Photography of the right plane corner of the center crystal

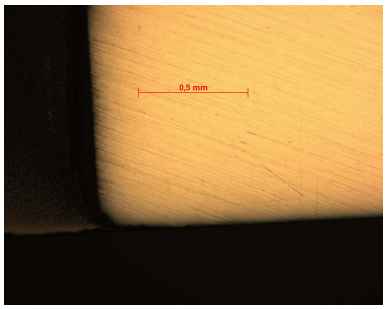

Figure 1.8: Photography of the left plane corner of the right crystal

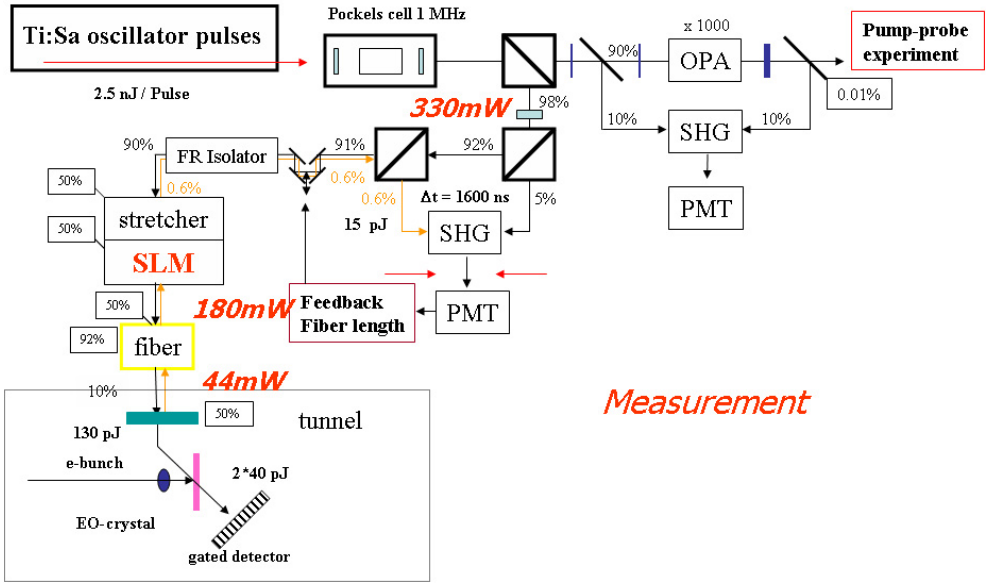

Figure 1.9: This diagram shows the energy balance for the whole setup. The percent values present the energy transmission for the certain elements. The red values are measured values. They show that the fiber produces an energy loss of 75%, comparing with the given attenuation of 0.5 db in the case of a 170 m long fiber which means a transmission of 90%, the main power loss is caused by the coupling of the laser into the fiber and out of the fiber. But the power at the ZnTe crystal is enough for the electro-optic sampling.

the coupling causes a power loss of 75%. The power behind the fiber out-coupling is 44 mW, this power will then be reduced by a beam splitter down to 22 mW. But this power will be enough for the electro-optic sampling.

0.6 Auto-correlator Setup

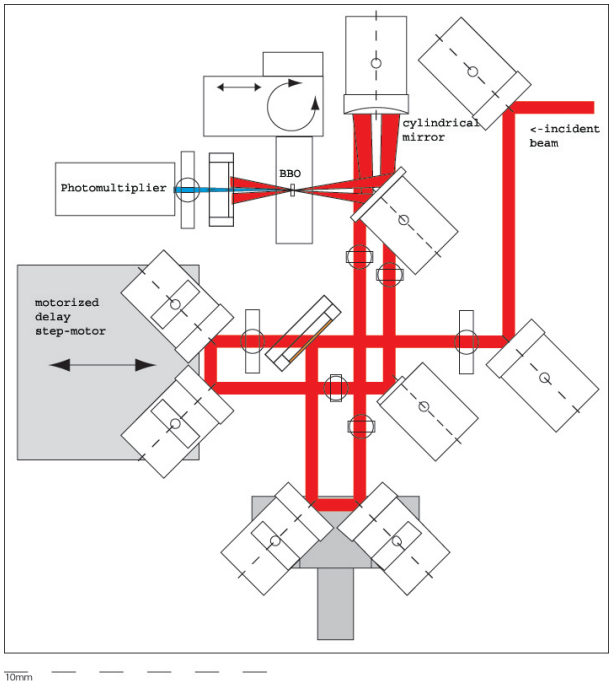

Figure 1.10: Setup of the auto-correlator used in the TEO experiment

List of Figures

List of Tables

Acknowledgements

Without the great support I was given during the course of this thesis, its completion would not have been possible.

Firstly I would like to thank Prof. Dr. Jörg Roßbach for the conceptual formulation and the support of this thesis.

Secondly my thanks go to Dr. Bernhard Schmidt for his constructive questions, for the correction of this work and for his support by building and providing the TEO experiment.

My sincere thanks go to Dr. Stefan Düsterer. With his formidable knowledge in laser physics and in every question concerning the TEO experiment my diploma thesis would not have been possible. I am also thankful for his assistance with the writing and with the arrange of this thesis.
The help and support for the measurement and the setup of the TEO experiment by Armin Azima was exceptional. Without his efforts and his knowledge the measurements and setups for this thesis would be much harder. Working closely together for almost a half year would not have been as easy as it was without his continuing support and the continuous motivation resulting from it.

Many special thanks go to Dr. Holger Schlarb for many helpful discussions and supports. He let me know the principles of the TEO experiment and guided me through the tasks, problems of my thesis and the the writing of my diploma thesis.
Important measurements are created by an auto-correlator which was designed and built up by Bernd Steffen. He also was an initiator for helpful discussions and supported me with the providing of important elements for the TEO experiment.
My thanks go also to Dr. Rasmus Ischebeck for guiding me through the first days at the DESY and for explaining me many problems concerning the setup and control of the experiment.
My work would have been much harder, if I had not been so well supported by the FLA team, especially Prof. Dr. Peter Schmüser, Jan Menzel, Axel Winter, Dr. Axel Knabbe and Dr. Sara Casalbuoni have always helped me to solve my

problems and they give me a good feeling being in the FEL group.
The experiment also needed many mounts and other infrastructural mechanisms which were realized by stuff of engineers and technicians, so I also thank Kai Ludwig, Jan Hauschildt, Otto Peters, Matthias Hoffmann, Matthias Böttcher and Dieter Habercorn for their support and their fast realization of the constructions for the experiment.
I am greatful for the help of Mrs. Ingrid Nikodem in coping with the DESY administration.
A special thank goes to Florian Löhl and Lars Fröhlich who brought me to my diploma thesis and who accompany me through my whole studies inclusive through this thesis.
Last but not least I would like to thank my family, colleagues and friends for their support and tolerance of my lack of communication during the last months.

Erklärung

Hiermit erkläre ich, diese Arbeit selbständig verfasst zu haben. Andere als die angegebenen Quellen und Hilfsmittel habe ich nicht benutzt und ich bin mit einer Veröffentlichung einverstanden.

Hamburg, im Juni 2005

(Franciskus Van den Berghe)